Fraunhofer
IKTS

Fraunhofer Institute for Ceramic Technologies and Systems IKTS

Kompetenzen in Keramik und Materialdiagnostik
Competencies in ceramics and materials diagnostics

On the determination of nonlinear elastic constants for residual stress measurements using Rayleigh waves

Sergey Gartsev

Fraunhofer Verlag

Fraunhofer Institute for
Ceramic Technologies and Systems IKTS

Schriftenreihe
Kompetenzen in Keramik und Materialdiagnostik

Publication Series
Competencies in ceramics and materials diagnostics

Editor
Prof. Dr. rer. nat. habil. Alexander Michaelis

Vol. 3

Sergey Gartsev

On the determination of nonlinear elastic constants for residual stress measurements using Rayleigh waves

Fraunhofer Verlag

Contact:
Fraunhofer Institute for
Ceramic Technologies and Systems IKTS
Winterbergstraße 28
01277 Dresden
Phone +49 351 2553-7700
info@ikts.fraunhofer.de
www.ikts.fraunhofer.de

Bibliographic information of the German National Library:
The German National Library has listed this publication in its Deutsche Nationalbibliografie; detailed bibliographic data is available on the internet at www.dnb.de.

ISSN: 2750-7246
ISBN (print edition): 978-3-8396-1881-3
DOI (free PDF version): https://doi.org/10.24406/publica-479

D 14

Zugl.: Dresden, TU, Diss., 2022

Print and finishing:
Fraunhofer Verlag, Mediendienstleistungen

The book was printed with chlorine- and acid-free paper.

© Fraunhofer Verlag, 2023
Nobelstraße 12
70569 Stuttgart
verlag@fraunhofer.de
www.verlag.fraunhofer.de

is a constituent entity of the Fraunhofer-Gesellschaft, and as such has no separate legal status.

Fraunhofer-Gesellschaft zur Förderung
der angewandten Forschung e.V.
Hansastraße 27 c
80686 München
www.fraunhofer.de

All rights reserved; no part of this publication may be translated, reproduced, stored in a retrieval system, or transmitted in any form or by any means, electronic, mechanical, photocopying, recording or otherwise, without the written permission of the publisher.

Many of the designations used by manufacturers and sellers to distinguish their products are claimed as trademarks. The quotation of those designations in whatever way does not imply the conclusion that the use of those designations is legal without the consent of the owner of the trademark.

Technische Universität Dresden

On the determination of nonlinear elastic constants for residual stress measurements using Rayleigh waves

M. Sc.

Sergey Gartsev

der Fakultät Elektrotechnik und Informationstechnik
der Technischen Universität Dresden

zur Erlangung des akademischen Grades

Doktoringenieur

(Dr.-Ing.)

genehmigte Dissertation

Vorsitzender:	Prof. Dr.-Ing. habil. Gerald Gerlach	Tag der Einreichung: 11.04.2022
Gutachter:	Hon.-Prof. Dr.-Ing Henning Heuer	Tag der Verteidigung: 30.09.2022
Gutachter:	Prof. Dr. rer. nat. habil. Andreas Mayer	
Gutachter:	Prof. Marco Ricci	

Abstract

In-field surface treatment intensity monitoring is still an open and challenging nondestructive testing problem. The main issue for the determination of residual stress levels by electromagnetic or ultrasonic measurements is the change in the microstructure of the treated material during processing and operation, which makes it impossible to uniquely relate the measured quantities (changes in conductivity, Barkhausen noise or elastic wave velocity) to variations in the stress-strain state.

This work is focused on the evaluation of acoustoelastic constants (AEC) by means of surface acoustic waves (Rayleigh waves, RW). These constants represent the state of the material's microstructure, and are thus very sensitive to variations in it. Moreover, these parameters are needed for the determination of the residual stress level with acoustoelastic measurements. Comparison of different testing strategies (direct measurement of RW AEC on the surface and mapping from the bulk wave AEC values), as well as investigation of the possibility of creating an in-situ method for measuring AEC near the surface using the nonlinear interaction of two Rayleigh waves are the main contributions of this work.

In order to assess the current level of measurement precision and to analyse the improvement possibilities, a series of experiments were carried out to measure bulk wave and surface wave acoustoelastic constants for untreated and treated materials. Several automated procedures and algorithms have been developed and applied to increase the robustness of the extraction of the measured parameters, also allowing the collection of the necessary data.

The indirect (mapping of bulk wave AEC to the surface wave AEC through the Grüneisen constants) and the direct method are compared for the different states of material (annealed, plastically deformed, surface treated) for the In718 and Ti6246 alloys. It is shown that mapping between bulk and surface wave acoustoelastic constants is not matching up, therefore the direct AEC measurements should be used for the stress-strain state evaluation in the vicinity of the surface. In addition, it is shown that surface AEC are very sensitive to any changes in material structure up to change in the sign of the effect, and for the practical application a direct in-situ Rayleigh wave AEC measurement should be performed.

Nonlinear elastic-wave interactions (also called wave mixing or scattering) — namely, the generation of secondary ultrasonic waves in a nonlinear medium — are considered as a prospective mean for near-surface nonlinear elastic parameter evaluation. The allowed interactions between bulk and surface waves, as well as the dependence of the scattering efficiency on the frequency and angle between source waves, were investigated through an analytical model, then compared with the experimental results and available FEM simulations. Finally, possible future steps for the development of the applied methods for the determination of near-surface higher-order elastic constants are discussed. In addition, a number of problem-specific numerical routines and algorithms have been developed and successfully applied. In conclusion, several proposals for the future experiments are given and briefly discussed.

Acronyms

ADC Analog-Digital Converter

AEC AcoustoElastic Constant

ANP Acoustic Nonlinear Parameter

BW Bulk Wave

DSP Digital Signal Processing

FEM Finite Element Modelling

FFT Fast Fourier Transform

HPF High-Pass Filter

HUGO High precision Ultrasonic GOniometer

In718 Ni-Cr19-Fe19-Nb5-Mo alloy

LDV Laser Doppler Vibrometry

LUT Laser Ultrasonic Testing

OLS Ordinary Least Squares fit

RANSAC RANdom SAmple Consensus

RW Rayleigh Wave

SAW Surface Acoustic Wave

SNR Signal-to-Noise Ratio

SOEC Second-Order Elastic Constant

STFT Short-Time Fourier Transform

Ti6246 Ti-6Al-2Sn-4Zr-6Mo alloy

TOEC Third-Order Elastic Constant

TOF Time Of Flight

Contents

Abstract . . . 3

Acronyms . . . 5

1 Introduction . . . 9
- 1.1 Short overview of available methods for surface treatment evaluation . . . 10
  - 1.1.1 Existing procedures: production, destructive and laboratory methods 11
  - 1.1.2 Development of the in-situ NDT methods . . . 11
  - 1.1.3 Comparison of the methods and objectives of current work . . . 14
- 1.2 Ultrasonic testing: an overview . . . 16
  - 1.2.1 Conventional ultrasonic testing . . . 16
  - 1.2.2 Nonlinear UT measurements . . . 18
  - 1.2.3 Existing limitations and challenges . . . 21

2 Theoretical Framework: elements of the theory of elasticity . . . 23
- 2.1 Linear model (Elastic moduli, infinitesimal displacements, plastic deformation region) . . . 23
- 2.2 Elastic waves in isotropic solids . . . 25
  - 2.2.1 Bulk waves . . . 25
  - 2.2.2 Surface acoustic waves (Rayleigh waves) . . . 25
- 2.3 Reflection and refraction of elastic waves . . . 26
- 2.4 Nonlinear theory of elasticity: account of third-order terms . . . 29
- 2.5 Acoustoelastic effect . . . 30
  - 2.5.1 BW AEC . . . 30
  - 2.5.2 RW AEC definitions and calculation from TOEC . . . 31
- 2.6 Rayleigh wave velocity dispersion inversion for stress measurement . . . 31
- 2.7 Nonlinear interaction of elastic waves in solids . . . 32

3 Methodology . . . 39
- 3.1 AEC measurements . . . 39
  - 3.1.1 TOEC/BW AEC measurements using contact ultrasonic measurements 40
  - 3.1.2 RW AEC measurements using laser interferometry . . . 41
- 3.2 Immersed measurements of RW dispersion using the ultrasonic goniometer HUGO . . . 42
- 3.3 Design of in-situ method of nonlinear elastic parameters estimation . . . 43
- 3.4 Algorithms . . . 49
  - 3.4.1 Automated strain extraction from raw extension data . . . 49
  - 3.4.2 Comparison of the group velocity evaluation methods for the BW AEC measurements . . . 50
  - 3.4.3 Group velocity evaluation using the iterative algorithm for the low SNR data . . . 54
  - 3.4.4 Phase velocity extraction . . . 55

3.4.5 Multidimensional phase unwrapping and wave vectors/phase velocity extraction . . . 59
3.4.6 Extraction of the radiation direction of elastic wave and its polarisation for sparse multidimensional data . . . 66
3.4.7 Local scattering efficiency by perturbation theory for wide-band primary pulses . . . 68
3.5 Supplementary study of applicability of contactless laser ultrasonics . . . 69

4 Results . . . 71
4.1 Third-Order Elastic Constant (TOEC) values for relevant superalloys . . . 71
4.2 RW AEC values for relevant superalloys . . . 72
4.3 Rayleigh wave dispersion measurements . . . 74
4.4 Nonlinear interaction of elastic waves and its potential for AEC estimation . . . 75
4.4.1 Perturbation model . . . 75
4.4.2 Experimental results . . . 77
4.4.3 Extraction of propagation direction and dominant polarization from multidimensional data . . . 79
4.4.4 Sensitivity of local scattering efficiency to TOEC variation . . . 79

5 Discussion . . . 81
5.1 Key parameters for the accuracy of the BW AEC and RW AEC measurements 81
5.2 Nonlinear interaction of Rayleigh waves as a prospective in-situ method for evaluation of surface layer nonlinear elastic constants . . . 82
5.3 Design of future setups for AEC determination . . . 83

6 Conclusion . . . 87

7 References . . . 89

8 Appendix . . . 99
8.1 Calculation of bulk waves acoustoelastic constants . . . 99
8.2 Algebraic expressions for RW AEC mapping from BW measurements . . . 100
8.3 Parameters of Rayleigh wave dispersion inversion . . . 100
8.4 Polarization restrictions for nonlinear bulk wave interactions . . . 101
8.5 Ordinary least squares fit . . . 102
8.6 Supplementary graphics of perturbation model simulation results . . . 103

List of publications . . . 112

1 Introduction

Since the begin of the era of aeronautics, the aerial vehicles and parts of its structures have always been among the most outstanding examples of the application of latest advances of the structural design, novel engineering approaches, advanced materials and production technologies and methods. Limiting to aviation, the design of the propulsion system was always at the frontiers of the theoretical and applied mechanics and materials science, demanding for the state-of-the-art manufacturing precision and outstanding fatigue life.

In particular, more than seventy years of development of gas turbine engines combined all of the available innovations all of aforementioned research fields. This could be explained by the harshest conditions under which the gas turbine elements are built to last: loads, temperature, pressure, vibrations and centrifugal forces. According to [Mee81; Kof04], the evolution of the jet engine structural design went into three main sections: application of new materials and material processing methods, active cooling and heat isolation.

Among the material processing methods applied for the enhancement of the efficiency and reliability of gas turbine engine structural elements, such as compressor and turbine discs and blades, one can highlight the surface treatment operations, namely the shot peening, laser shock peening and deep rolling. Those techniques are applied in many industries in order to improve the structural elements operational lifetime. The core of all those methods is the modification of the outer layer of metal, in order to induce the compressive residual stresses, which significantly improves the high-cycle fatigue properties [Sch14]. This effect is directly dependent on the intensity and the state of the treatment [Wag99].

The goal of the surface treatment operations, considered in this work (namely the shot peening, laser shock peening, low plasticity burnishing) is the introduction of compressive residual stress in a thin (0.1 – 0.5 *mm*) surface layer. These methods are used for enhancement of the expected fatigue life of critical structural components: an induced compressive stress layer suppresses the initiation and growth of a crack under (cyclic) tensile load, therefore improving the overall fatigue performance [Sch06]. As an example, such a treatment is used in the production chain of blade discs for gas turbines, which are exposed to high temperatures and to high centrifugal tensile stresses. Components in the hot part of the gas turbine engine (turbine discs and blades) are operating under the temperatures up to 600°C [Pre06], which creates the potential for the thermal annealing or release of the induced compressive stresses.

Ultrasonics is one of the standard methods for non-destructive testing (NDT) and material studies [Bra96]. However, despite several decades of intensive research, a robust method for in-situ residual stress evaluation using the UT measurements is yet to be de-

rived. In this contribution the current state-of-the-art research in this topic have been assembled, and the existing limitations for the commercial application of ultrasonic measurements for the evaluation of surface treatment intensity have been outlined. Moreover, a prospective supplementary experimental design, based on the properties of nonlinear interaction of ultrasonic waves in a solid, is presented and its applicability is evaluated using the commercially available equipment. Such measurements are one step further towards the in-situ evaluation of nonlinear elastic parameters in a thin surface layer, which are crucial for the residual stress evaluation. In addition, a comprehensive set of processing tools, such as Digital Signal Processing (DSP) algorithms for the robust extraction of relevant parameters is presented. Last but not least, an extensive series of analytical simulations was performed to optimize the layout of experiments, and to interpret the outcomes.

1.1 Short overview of available methods for surface treatment evaluation

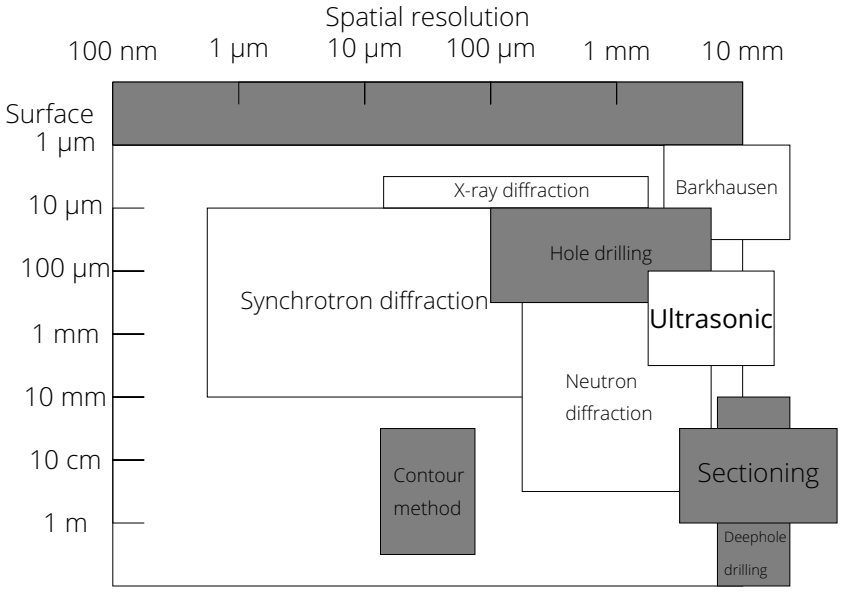


Figure 1.1: Typical penetration depth and the spatial resolution of the various residual stress measurement techniques (from [Ros12; Sch14]). The destructive methods are colored.

The estimation of residual stresses is a subclass of the general stress-strain state evaluation problem. Surface treatment, i.e. shot peening, is a mature industrial procedure (first reports on the beneficial effect of the shot peening on fatigue life date back to at least 1938 [Pla83]). Since then a large number of laboratory and destructive methods for measuring residual stresses have been developed to assess the stress-strain state during and/or after operations. According to [Ros12; Sch14], residual stress measurement methods could be depicted according to their spatial resolution and penetration (Figure 1.1). Below is a brief description and basic principle of the most common ones.

1.1.1 Existing procedures: production, destructive and laboratory methods

Almen stripes

The first prototype for the procedure to evaluate the intensity of the treatment was introduced in 1942 by J.O. Almen (U.S. Patent 2350440A), and based on measurements on standardized metal stripes, treated with the same process (i.e. beads size, energy, intensity), as the structural element under test. Under the action of compressive stresses, the strip deforms into an arc, the bending profile of which can be measured with an Almen gauge. This method also gave its name to the technical unit of treatment intensity.

Destructive methods

The principle underlying the destructive methods of residual stress assessment (slitting, layer removal, hole drilling and contouring) is relaxation measurements. By observing the redistribution of the field of deformations (change in shape of the specimen) induced by controlled removal of material portions or drilling, and comparing it with an analytical/numerical solution, the stress-strain state of the original specimen can be restored.

Diffraction methods

The other branch of methods, namely diffraction methods, are mainly used as reference laboratory methods. The principle may be described as follows: electromagnetic radiation (typically, X-rays) or neutrons penetrates the surface layer of a material with a regular lattice (penetration depth in the range of 0.05-100 mm, depending on photon/particle energy and material) and then re-radiate according to Bragg's law:

$$n\lambda = 2d\sin(\theta) \tag{1.1}$$

By extraction of the lattice parameter d, one can estimate the absolute residual or applied strain. Though some portable X-ray solutions are available on the market, their applicability is restricted with the limited output beam energy, and therefore the maximum penetration depth.

It should be mentioned, that both measurement methods are linked directly with the measurements of the strain. The mapping from the strain levels to the stress evaluation is done usually either with using of the literature values of linear elastic properties of the material, or through an additional calibration procedure [Ast].

It is also worth mentioning other state-of-the-art laboratory approaches, namely the use of indentation measurements [Car01] and electron backscatter diffraction [Chi11] to characterise the residual stress caused by the surface treatment.

1.1.2 Development of the in-situ NDT methods

In comparison with the laboratory methods, conventional quantitative nondestructive evaluation (NDE) methods, in particular electromagnetic and ultrasonic testing, are either applicable for ferromagnetic metals only, or still found themselves at the development stage.

Electromagnetic methods: overview

The characteristics of electromagnetic (EM) field propagation in various materials (conductive and non-conductive, ferromagnetic and non-ferromagnetic) are widely used in nondestructive testing [Bra96]. The basic principle behind magnetic and eddy current methods is

as follows: a sample is placed in an EM field generated by a permanent magnet/electromagnet or eddy current coil and a response is measured using another coil circuit with a specific shape and frequency close to the specimen surface which is sensitive to changes in the magnetic and electrical properties.
Magnetic flux leakage measurements for ferromagnetic materials, for example, consist of a permanent magnet or electromagnet, and magnetic flux detector (e.g. a Hall element or an induction coil), and typically suitable for detecting changes in the magnetic field associated with cracks or flaws in a specimen. Later a similar setup was used to measure residual stresses using Magnetic Barkhausen noise.

Magnetic Barkhausen Noise

Magnetic Barkhausen Noise (MBN) measurements use the sensitivity of the "macroscopic" magnetic hysteresis loop and related time-averaged parameters associated with the movement of multigrain domain walls under an external magnetic field in the presence of material degradation and/or internal stresses. This effect has been known for almost a century [Tyn27]. These parameters can be detected either by using a non-contact sensor coil (magnetic Barkhausen emission) or by using a contact piezoelectric sensor (acoustic Barkhausen emission) by placing the sample in an external alternating magnetic field. Naturally this method is only applicable for ferromagnetic metals (i.e. non-austenitic steels). The maximum penetration depth is usually limited to a few millimetres and the maximum measurable stress levels are limited to 300-400 MPa [Gau98; Sch14].

Eddy Current

In general, eddy current testing methods measure the local variations of conductivity/resistance and magnetic permeability properties in the vicinity of the specimen surface and can be applied to any electrically conductive material.
Over the last 20 years significant research efforts have been devoted to the development of surface treatment monitoring methods using eddy current [Zil01; Blo04; AN10b; AN10a; Mad10; Hil10; Bot18]. The dependence of the conductivity tensor [σ] on the elastic stress [τ] can be described as follows [Blo04]:

$$\begin{bmatrix}\sigma_1\\ \sigma_2\\ \sigma_3\end{bmatrix} = \begin{bmatrix}\sigma_0 & 0 & 0\\ 0 & \sigma_0 & 0\\ 0 & 0 & \sigma_0\end{bmatrix} + \begin{bmatrix}K_{\shortparallel} & K_{\perp} & K_{\perp}\\ K_{\perp} & K_{\shortparallel} & K_{\perp}\\ K_{\perp} & K_{\perp} & K_{\shortparallel}\end{bmatrix}\begin{bmatrix}\tau_1\\ \tau_2\\ \tau_3\end{bmatrix} \tag{1.2}$$

where σ_0 denotes the electrical conductivity of an isotropic body in the absence of stress and $K_{\shortparallel}$ and $K_{\perp}$ are electroelastic coefficients, parallel and normal to the stress direction, respectively. Through the calibration measurements of the Apparent Eddy Current Conductivity (AECC) variation under the uniaxial stress, the effective electroelastic coefficient, or

$$\frac{\delta\sigma_0}{\tau_1} = K_0 = \frac{1}{2}(K_{\shortparallel} + K_{\perp}) \tag{1.3}$$

can be estimated. As these coefficients are material-specific and are not widely available in the literature, they usually have to be measured before a test. This fact, as well as the sensitivity of the coefficients to processing intensities, considerably limit the application of EC-measurements for superalloys.

Eddy Current Induced Thermography

Over the last 20 years, advances in infrared (IR) camera development and the resources available for thermographic image processing have opened up a wide range of applications for infrared non-destructive testing stimulated by various heat sources (i.e. flash [Wan18], resonant vibration excitation [Sol15] or eddy currents [Tia16]). Along with enhanced data processing capabilities (resulting in increased lateral/depth resolution) due to full-matrix recording of thermal field evolution, a particular advantage of eddy-current pulse thermography (ECPT) is the possibility to quantify both the electrical and thermal properties of the material under study, through its ability to decompose the Joule heating (or resistance/conductivity) and heat diffusion, according to Fourier's law [Yin13]. The dependence of the thermal properties of a material on its stress-strain state has not found wide application in NDE. However, there are several theoretical and experimental works providing the relation between mechanical and thermal properties of the medium [Ros84; Tri04; Bai]. Here a brief idea from [Ros84] is given.

The thermal conductivity λ in metal can be represented as the sum of two components:

$$\lambda = \lambda_e + \lambda_f \tag{1.4}$$

where λ_e is the electronic thermal conductivity and λ_f is the phonon (lattice) thermal conductivity. The first term is prevailing in pure metals at room temperature. The heat carriers (electrons and phonons) can be scattered by impurities, phonons or electrons. Therefore, the thermal resistivity $W_e = \frac{1}{\lambda_e}$ can be written as

$$W_e = W_{e0} + W_{ef} + W_{ee}, \tag{1.5}$$

where the terms on the right refer to impurities, phonons and electrons, respectively. At relative high temperatures (T $\sim$ 300K), W_e is dominated by electron-phonon scattering, which could be approximated according to the Wiedemann-Franz law:

$$W_{ef} = \frac{\rho_e}{L_0 T} \tag{1.6}$$

where ρ_e is the electrical resistivity, which depends on the elastic stress through the piezoresistive (or electroelastic) effect [Ros84; Mor10].

Up to now, currently available infrared cameras do not yet meet the accuracy and sensitivity requirements for detection of small (less than 1%) variations in thermal/electrical properties in thin layers. However, with the further proliferation of infrared cameras, this challenge may become solvable. The required sensitivity and frame rate should be at least in the range $\sim$ 5-15 mK at 100 Hz respectively, which until now is achievable for high-end IR cameras with a cooled photon detector.

Ultrasonic Testing

The acoustoelastic effect, or the dependence of the velocity of propagation of the ultrasonic wave on the level of stress (strain) of the medium, makes it possible to characterize stress by means of ultrasonic testing.

Practical applications of the acoustoelastic effect may consist of either extended characterization of materials by measuring higher order elastic constants at known stress levels, or by evaluating the strain and stress levels (applied or residual), having the necessary information about the nonlinear material properties (Fig. 1.2).

The limited number of available experimental values for nonlinear elastic constants depending on a large number of parameters (e.g. plastic deformation, surface layer erosion

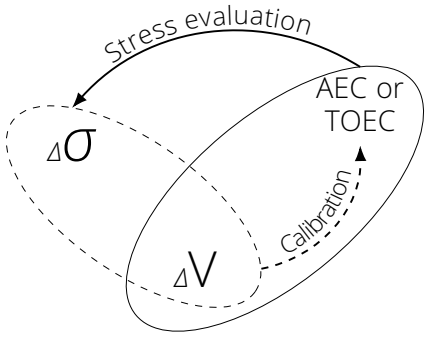


Figure 1.2: Acoustoelastic effect connects the variation in stress level with the variation in ultrasonic wave propagation velocity through the nonlinear properties of material (AECs or TOECs).

and annealing) seriously limit the potential practical application of the acoustoelastic effect. Also an important limitation is the lack of an engineering model describing the dependence of nonlinear elastic constants, on microstructure changes also associated with surface treatment and harsh operating conditions.

1.1.3 Comparison of the methods and objectives of current work

Considering the different approaches available for measuring residual stresses and their limitations (Table 1.1), ultrasonic inspection is one of the most promising tools for the development of in situ industrial residual stress control method, due to its relatively low equipment cost, advanced theoretical basis, non-contact measurement capability with Laser Ultrasonic Testing (LUT), and high signal-to-noise ratio for immersion testing.

Since the determination of nonlinear elastic parameters (Rayleigh Wave (RW) AcoustoElastic Constant (AEC)) at the material surface is the main difficulty for the practical application of the acoustoelastic effect to assess residual stresses, the main objective of this work is to compare available methods for its assessment, their accuracy and applicability, and to develop a new in-situ method using the nonlinear elastic wave interaction effect.

In this work the accuracy of AEC determination by means of direct and indirect measurements for relevant materials is evaluated using the large amount of gathered experimental data. An important part of the work is the analytical and experimental analysis of the application of non-linear surface elastic wave interaction to determine RW AEC, performed for the first time. To improve the accuracy and reliability of the extraction of measured quantities, a number of problem-specific automatic and semi-automatic procedures and algorithms have been developed, tested and successfully applied to the experimental and available FEM data.

Method	Precision (~% of yield stress)	Penetration depth	Works best for	Has limitations with
Splitting	10-25%	Specimen thickness	Routine comparative quality control	Nonuniform and untypical stresses
Sectioning	5-15%	Specimen thickness	Specimens with regular-shaped geometry	Challenging calculations for multiple sectioning
Stoney Equation	3-10%	Layer thickness	Thin layers on flexible beams	Determining layer thickness accurately
Layer Removal	5-15%	Specimen thickness	Flat plates and cylinders of uniform thickness	Subject to measurement drift
Hole Drilling	5-15%	Up to 2 mm	Near-surface measurements of in-plane stress	Max. stress=70% yield
Deep Hole Drilling	3-10%	Specimen thickness	Large components	Compromised by plasticity
Slitting	3-10%	Specimen thickness	1D perpendicular stress in prismatic shaped specimens	Non-uniform across width stresses
Contouring	3-10%	Specimen X-section	2D perpendicular stress in prismatic shaped specimens	Cutting accuracy, problems for near-surface
X-ray Diffration	~20MPa	<0.03 mm	Near surface measurements on crystalline materials	Variations in grain structure and surface texture
Synchrotron Diffraction	~50MPa	>5 mm	Deeper non-destructive measurements than X-ray	Requires synchrotron and zero-stress refreference
Neutron Diffraction	~50MPa	25 mm (Steel)/100 mm (Al)	Deeper non-destructive measurements than Synchrotron	Requires neutron radiation source and zero-stress reference
Magnetic BNA	>25MPa	1 mm	Ferromagnetic materials only	Material-specific calibration
Ultrasonic	>25MPa	1-20 mm	Low-cost comparative measurements	Material-specific calibration
Thermoelastic	Qual.	var.	Low-cost comparative measurements	Not quantitative
Photoelastic	5-15%	Specimen thickness	Full-field measurements in transparent materials	Transparent materials, not quantitative
Indentation	Qual.	<1 mm	Comparative measurements	Not quantitative

Table 1.1: From [Sch14]: Comparison of practical residual stress measurement methods and their limitations.

1.2 Ultrasonic testing: an overview

Ultrasonic testing is generally defined as the use of elastic waves with a frequency of 20 kHz or higher for non-destructive testing, in particular for detection of defects, for measurement of element thicknesses and for determination of physical properties [Kra90]. The following chapter presents a brief review of the development stages, current applications and existing limitations of ultrasonic testing and evaluation methods.

The idea of ultrasonic testing of materials was first introduced by S. Sokolov in 1929, who suggested using the characteristics of a continuous elastic waves to detect defects in solid materials [Sok29]. However, it is believed that the first commercial pulse-echo measurement systems were developed not earlier than 1943 simultaneously in the USA (based on the work of F. Firestone) and in UK (D. Sproule) [Gra81].

Although the basic concept (pulse-echo or through-transmission test) for most applications remains the same to this day, advances in electronics and digital data processing change the industry standards almost every decade. In 1952, for example, D.C. Erdman patented an ultrasonic flaw detector that displayed an echo signal from a sample submerged in water along the scanning axis on a cathode ray tube along the axes (space, time) (patent US2593865A). With the further development of analog and digital experimental equipment, the use of synthetic aperture radar and sonar imaging techniques, new types of inspections became available. For example, the concepts of beam shaping, angular control and focusing, well known from radar theory, have been applied for the first time in the form of a predecessor of the phased array ultrasonic transducer (PAUT) in 1954 [Bra54]. It took over fifteen years to reach the field of medical diagnosis and another fifteen years to bring PAUT to industrial applications. Only in the last 25 years, linear and matrix phased array ultrasonic transducers of various shapes have entered the broad non-destructive testing market [Bra96].

The RCA Laboratories group seems to have been the first to demonstrate the applicability of laser interferometry for detection and visualisation of ultrasonic waves [Mez74]. Later, with the development of compact commercial Laser Doppler Vibrometry (LDV) (such as Polytec, optomec and others), absolute displacement (or velocity or acceleration) measurements became the de facto standard for remote non-contact ultrasonic measurements.

Not only the properties of bulk wave propagation have been utilized for NDT: the special solution of the boundary value problem on the surface of an elastic solid body was theoretically predicted by Lord Rayleigh in 1885 [Ray85]. The first applications of RW, or Surface Acoustic Wave (SAW), in the field of non-destructive testing date no later than 1954 [Coo54; Min54]. Although they have been widely used in microelectronics in interdigital devices and SAW filters since the 1970s, RW are still a niche solution for industrial non-destructive testing.

Another family of elastic waves, namely guided waves (Lamb waves or plate waves) propagating in thin plates and shells are also applied in the context of non-destructive testing problems [Gri61; Bra96]. The commercial application of test systems based on guided wave propagation characteristics began in the last decade of the XX century [Ros10].

1.2.1 Conventional ultrasonic testing

The most common industrial application of ultrasonic testing is non-destructive assessment of the structural integrity of samples, structural elements and structures of metal alloys, modern carbon and glass fibre reinforced composites, concrete, wood and many other materials as well as evaluation of their mechanical properties. The main fields of application and the corresponding methods can be categorised by the typical operating frequency. Approximate frequency range of conventional ultrasonic testing methods is

represented graphically in Figure 1.3.

In the "low frequency ultrasonic range" or around 15(20)-300 kHz, guided wave and air-coupled UT testing methods are dominant. The propagation properties of guided waves (Lamb waves or plate waves) depend on both elastic and geometric properties of the structure under test. Up to now the main (and still mostly promising) applications are the inspection of pipelines, rails and plates [Pap08; Oli21]. Although guided waves have the unique feature of propagating tens of metres along a structure, many practical issues such as reliable excitation and problems of interpreting the real signal still remain open [Ros10].

Air-coupled ultrasonic methods have an immediate and obvious advantage over other methods. The use of air as a couplant closes all the problems associated with the transmission of the elastic pulse. However, the main limitation of air-coupled UT methods is the significant mismatch of acoustic impedances of air and most of the materials, as well as the strong attenuation of ultrasound in the air. This limits the use of ACUT mainly to materials with low acoustic impedance (polymers reinforced with glass and carbon fibres, wood, textiles and others) and to the frequency range 100-2000 kHz.

The most versatile and widespread area of ultrasonic inspection is contact and immersion methods. Here the problem of transmitting an elastic wave to the structure under test is solved by using special gels or oils, or by direct immersion into a liquid (usually water). When using a normal incident single element (pulse-echo), PAUT, or a pair of transducers (through-transmission or pitch-catch) with normal incident or inclined transducers, the vast variety of structural defects can be detected. This family of techniques is used to detect fatigue cracks, inclusions or porosity, grain structure and weld defects, as well as for material investigation and thickness measurements [Bra96]. Most of these applications are performed in the frequency range 0.5-20 MHz.

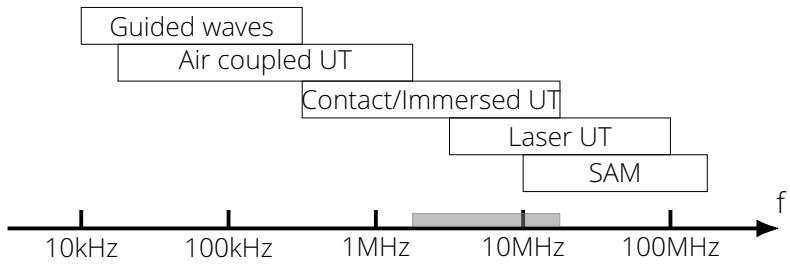


Figure 1.3: Approximate operating frequency range of the conventional ultrasonic methods for industrial NDT. The frequency range of interest (Rayleigh wave penetration depth of order of surface treatment depth) is indicated by grey.

Contactless high-frequency ultrasonic inspection is also possible using laser excitation and detection. A high-power laser pulse (i.e. Ng:YaG) locally heats the sample surface, creating thermoelastic deformation and/or ablation or evaporation of a thin surface layer of material. These factors generate an elastic pulse, which can be detected by a laser interferometer. The method has found application in testing composite and metal structures and for in-line inspection of welding and metal rolling quality [Mon04] [1].

At higher frequencies (around 20-200 MHz, with existing extensions up to the GHz range) scanning acoustic microscopy is widely used for various biological applications, quality

[1] Another special case is the use of electromagnetic forces, namely magnetostrictive, Lorentz or Coulomb forces, to generate elastic waves, is beyond the scope of this brief review.

monitoring of integrated circuits and testing of composite materials with lateral resolution down to fractions of *μm* [KY93; Ary18]. Obviously, operating at high frequency has the disadvantage of limiting the penetration depth (range *μm* to *mm*).

Most of these approaches are prone to similar drawbacks:

1. Fundamental physical constraints impose severe limitations on ultrasonic inspection: trade-off between minimal resolution and penetration depth always arise due to the properties of elastic wave propagation in all media.
2. Ultrasonic transducers only provide relative measures of pressure of elastic wave: record-ed amplitude in relative units and the time delay limits the potential application (does not apply for the laser interferometry).
3. Most ultrasonic methods require coupling between transducer (transmitter and receiver) and the specimen surface, by introducing layer of couplant of an unknown thickness that varies from point to point. This introduces an additional source of uncertainty. Furthermore, the gel and oil can evaporate over time, which alters the bonding conditions. Finally, dissolved gases, air bubbles and other inclusions can affect the quality of immersion tests [Kra90].
4. A reliable interpretation of UT signals requires a higher average level of system operator [Dgz]: standard UT training requires more time investment in comparison to the other in-situ methods.

Despite all these limitations, ultrasonic nondestructive testing methods hold the largest part on NDT market [Ndt], offering high accuracy, a wide range of problem-specific tailoring and competitive overall cost.

1.2.2 Nonlinear UT measurements

Most of the methods mentioned above are described using theoretical models based on linear elasticity theory, valid for infinitesimal deformations [Aul73; Lan86]. However, for a certain class of problems, it is necessary to extend the linear model to adequately describe the observed phenomena. One of such problems is the estimation of mechanical stresses using the acoustoelastic effect - dependence of the ultrasonic wave propagation velocity on the stress (strain). This section presents a brief review of existing works in the field of nonlinear ultrasound related to the problem of qualification and quantification of applied and residual stresses in metals.

The first studies on nonlinear deformation of elastic bodies were carried out by D. Bernoulli and L. Euler. Later A. Cauchy, G. Green and V. Saint-Venant laid the foundations of nonlinear strain theory, which developed into general elasticity theory in the second half of the XIX century [Sav70]. It is believed that Brillouin in 1925 [Bri25] was the first to explicitly relate the stress tensor and the velocity of elastic wave propagation in an elastic medium. However, only after a series of publications by F.D. Murnaghan, which culminated in a comprehensive monograph in 1951 [Mur51], where the author presented an elegant theoretical model of finite strains of elastic isotropic and anisotropic solids, the practical application of the acoustoelastic effect began.

Using Murnaghan's formalism, Hughes and Kelly [Hug53] derived an explicit relation between the velocity of bulk elastic waves of different polarization and the internal stresses. They were also apparently the first to publish the results of applying the acoustoelastic effect to the characterisation of materials by measuring specific non-linear parameters - Third-Order Elastic Constant (TOEC) for polystyrene, iron and glass in different material states.

RW acoustoelastic effect for the surface treatment intensity evaluation

In 1960 Frederick [Fre60] presented experimental results on the dependence of Rayleigh wave velocity on residual stress for various aluminium and steel alloys. The following year, Hayes and Rivlin [Hay61] published an explicit theoretical description of the acoustoelastic Rayleigh wave effect. T.L.Szabo [Sza75] investigated the problem of inversion of SAW velocity dispersion for hardened steel. The analytical model was later extended and experimentally verified for the case of non-uniform loading [Hir81]; in this work, the Rayleigh wave velocity dispersion associated with a depth-varying stress was measured with an applied load on a mild steel sample. A. Zeiger et al. [Zei82] showed the temperature dependence of the measured RW AEC for several steel alloys. Later D. Husson and G. S. Kino [Hus82; Hus85] published a comprehensive perturbation theory for the acoustoelastic effect in case of inhomogeneous stresses on inhomogeneous elastic bodies for bulk and surface (Rayleigh and Lamb type) waves. In recent years, P. Mora and M. Spies [Mor19a; Mor19b] revised this contribution and proposed a new formulation.

In a detailed theoretical review [Man87] on the applicability of stress quantification using ultrasonic methods, the authors pointed out several main limitations.

- First, since the residual stresses in bodies are usually caused by inelastic processes (thermo-mechanical surface treatments such as welding, drilling and others), the existing theory of elastic-plastic deformation, which cannot adequately describe these phenomena, needs further development. This statement is based on the work of G.C. Johnson [Joh81], where several samples of aluminium alloys (6061-T651, 2024-T351 and 7075-T651) were investigated and showed the alloy-specific dependence of variation of AEC with plastic deformation.

- Another problem is the distinction between stress induced rate changes and metal texture changes. Although this has already been mentioned in [Cre67], a robust industrial approach to accounting for grain alignment has not yet been implemented. However, there are some methods using birefringent shear waves or critically refracted longitudinal waves which have limited application [Sch14] for stress estimation using ultrasound.

This thesis focuses on the development of an NDE method for monitoring residual stresses for one particular family of mechanical treatment, namely surface treatment, which includes the shot peening, laser shock processing and deep rolling. All of these techniques aim to create a surface layer of compressive residual stresses balanced by tensile stresses deep within the machined part (shown schematically in Figure 1.4). This type of treatment significantly slows down the surface fatigue crack growth [Wag99] and resistance to foreign object damage [Pre04], both in the fabrication and repair phase [Liu01]. P. Nagy et al. [Car02] were among the first researchers to investigate the applicability of UT to assess residual stresses induced by surface treatment for aluminium alloy. His group also reported on the dependence of nonlinear elastic parameters on microstructural changes induced by plastic deformation (cold work), also induced by surface treatment [Nag06].

The demand for surface treatment intensity control tools comes strong from jet engine manufacturers: critical jet engine components are exposed to high-temperature stresses (e.g. discs and blades of high-pressure turbines) and the possibility of annealing during operation is present [Sch06]. These components are made from high-strength, high-temperature superalloys such as Inconel (trade name for a nickel-chromium-based alloy) and titanium alloys. Lack of a certified tool for monitoring residual stresses (and hence remaining life prediction), required by the [EAS03; FAA09] certification requirements, limits the potential for weight optimisation by maximising the positive effects of surface treatment. For the relevant superalloys, only a few experimentally measured non-linear elastic

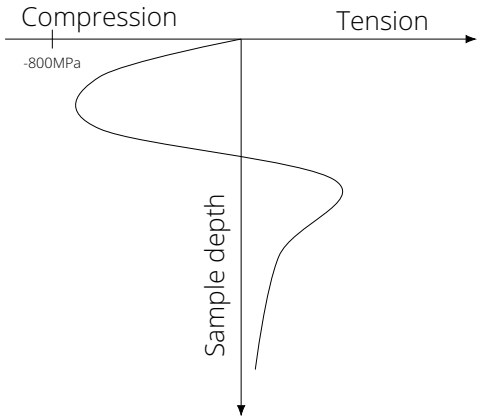


Figure 1.4: Schematically shown residual stress depth profile for surface treated components.

parameters - acoustoelastic constants or third order elastic constants have been published [Hub12; Rje13]. Since the surface treatment intensity is depth dependent, Rayleigh wave dispersion measurement seems to be the most convenient method of ultrasonic inspection. Following the first publications on the determination of the residual strength of shot-peened aluminum alloys [M.02; Rui04], several groups have published RW velocity dispersion measurements for high-temperature superalloys [Köh10b; Bar12; Hub14]. However, the problem of relating the measured RW velocity dispersion to a specific residual stress depth profile has not yet been solved.

Thus, improving the methodology for measurement of the nonlinear elastic characteristics of high-temperature superalloys in different processing states, as well as searching for an independent way to in-situ evaluation of nonlinear material properties are the two main challenges of this contribution.

Nonlinear interaction of elastic waves

Another physical effect which gives an insight into the nonlinear elastic properties of solids is the nonlinear elastic wave interaction (or wave scattering or wave mixing): a non-linear solid generates secondary elastic waves in the presence of two primary elastic waves.

This effect and a brief analysis of the possible types of interacting waves was described no later than 1944 by L.D. Landau [L.D44]. Later, Goldberg [Gol60] derived an explicit equation of motion for a nonlinear medium. The possible types of initial and scattered waves, as well as the interaction criterion were discussed by G. Jones and D. Cobett [Jon63], they have also presented the first numerical results for wave scattering in polystyrene. Taylor and Rollins [Tay64; Rol64] extended the theoretical description and also presented the first experimental results for fused silicon, polycrystalline aluminium and polycrystalline magnesium.

Korneev et al. [Kor98] extended the polarisation constraints on the interaction of different types of bulk waves (pressure waves and shear waves with vertical and horizontal polarisation) and presented experimental results for sandstone. Regarding practical NDE applications, bulk wave scattering has been presented to monitor ageing in thermoplastics [Dem12; Dem14] and adhesive joints [Ju19a], the occurrence of fatigue cracks in steel samples [Hil06], quality control of titanium diffusion joints [ER13] and detection of plastic deformation in aluminium [Sun18].

Meanwhile, the bulk wave and Rayleigh wave interaction has been used to the greatest extent for piezoelectric materials and thin films (for interdigital devices) [F. 84]. The first experimental results of surface acoustic wave mixing experiments for pure crystals were presented not later than 1970 [Lea70] for $LiNbO_3$ substrate in GHz range. Further experimental, analytical and numerical studies related [Vel74; Zab92; Shu93] mainly on piezoelectrics. The generation of second harmonics in a nonlinear medium along the SAW propagation path can be interpreted as a special case of interaction of two identical collinear waves [Pad76; Nor79; Kal82; Kal83; Ben13; Ju19b]. Measurements of second harmonic generation (or Acoustic Nonlinear Parameter (ANP) β measurements , which can be derived from TOECs and SOECs), can also be used for NDE surface treatment [Jha09; Liu11; Mat14], or fatigue damage accumulation [Bar03; Her06], as ANP is directly related to the nonlinear material properties depending on the microstructure.

Up to now the collinear and non-collinear Rayleigh wave scattering has mainly been used for piezoelectric thin films for interdigital devices and SAW filters [F. 84; Cam89; Mor07]. Recently published work related to the practical applications of nonlinear wave interactions in NDE are focused on the interaction of bulk waves [Kor98; Kor14; Dem14; Dem15] and Lamb waves [Jin17; Ish18a; Ish18b; Has18; Mor22].

1.2.3 Existing limitations and challenges

Nonlinear ultrasonic measurements in metals, and measurements of TOEC/AEC in particular, are challenging for a several reasons [Zar66]:

- Murnaghan elasticity theory describes the finite-amplitude displacements in isotropic bodies at the macro level, and excludes the influence of defects associated with grains, texture, dislocations and vacancies at the micro level. These defects may significantly affect the values of higher order elastic constants, if their size and periodicity are comparable to the wave length [Rje18].
- Since Murnaghan's theory for isotropic bodies involves three TOEC, at least three independent experiments must be performed to determine the TOEC.
- Since measurable quantities (e.g. AEC or scattering efficiency) consist of a combinations of TOEC (which are often not completely independent either), it is virtually impossible to determine experimentally the sign of TOEC without additional hypotheses for some materials.
- Static or dynamic strain (for acoustoelastic or wave mixing measurements) must be large enough for reliable measurements. In practice: the strain level should be greater than 1e-4, which is the limit of commercial ultrasonic transducers and amplifiers.

Furthermore, the scale of the effects puts serious demands on the experimental design and processing algorithms, as both the change in wave velocity and the amplitude of the scattered wave compared to the fundamental components are in the range of fractions of a percent.

Thus, the main practical objectives of this work are to investigate the current accuracy of TOEC/AEC measurements for existing laboratory equipment, the possibility of improving these parameters using digital signal processing techniques, and to develop the basis of a new measurement principle based on the effect of nonlinear interaction of surface acoustic waves in metal.

2 Theoretical Framework: elements of the theory of elasticity

All real bodies are deformed by physical forces, changing their shape and/or volume. These changes are called *strains*. The theory of elasticity deals with elastic solids: if the applied forces are released quasi-statically, the strains are vanishing. The following assumptions will then be made: the deformations in elastic solids will be isothermal (or adiabatic), and heat transfer from one part of the body to another in dynamic processes (such as wave motion) will be excluded. In addition, typical dimensions are assumed to be much larger than intermolecular distances, so the internal forces, or *internal stresses*, acting on a small volume of the body are only transferred through its surface. The following subsection briefly summarizes the theory from [Bre85; Lan86; Lur05].

2.1 Linear model (Elastic moduli, infinitesimal displacements, plastic deformation region)

When elastic body is deformed by the action of external forces, internal stresses occur. One can represent the force acting on the arbitrary small volume dV as $\int \boldsymbol{F} dV$, where $\boldsymbol{F}$ is the force per unit volume. As the total force acting on the small volume is equal in magnitude and opposite in direction to resultant of all the other forces, and accounting the divergence theorem, we could write for each of three components F_i:

$$F_i = \frac{\partial \sigma_{ik}}{\partial X_k}, and \int F_i dV = \int \frac{\partial \sigma_{ik}}{\partial X_k} dV = \oint_S \sigma_{ik} n_k dS, \tag{2.1}$$

where $\boldsymbol{n} = \{n_k\}$ is an unit normal to the surface S, bounding the volume, and tensor σ_{ik} is the symmetric *stress tensor*. In Equation (2.1) the Einstein summation convention is used (summation over repeated Cartesian indices is implied). This notation also holds in all the following equations, unless explicitly stated otherwise.

The position of each point of the body prior to the deformation could be defined by a vector $\boldsymbol{r} = \{X_1, X_2, X_3\}$ and after deformation by a $\boldsymbol{r'} = \{X'_1, X'_2, X'_3\}$ in Cartesian coordinate system. The quantity $\boldsymbol{u} = \boldsymbol{r'} - \boldsymbol{r}; u_i = X'_i - X_i$ for $i = 1, 2, 3$, is called the displacement vector. If $\boldsymbol{u}(\boldsymbol{r})$ is known, we can introduce the symmetrical *Cauchy strain tensor*:

$$u_{ik} = u_{ki} = \frac{1}{2} \left(\frac{\partial u_i}{\partial X_k} + \frac{\partial u_k}{\partial X_i} \right) \tag{2.2}$$

Strain tensor could be transformed to diagonal form by coordinate change; therefore any deformation could be represented as tension and compression along three pairwise perpendicular axes, called the *principal strain axes*. Three strain invariants can be derived:

$$\begin{aligned} I_1 &= u_{ii}, \\ I_2 &= \frac{1}{2}(u_{ii}u_{kk} - u_{ik}u_{ik}), \\ I_3 &= det(u_{ik}). \end{aligned}$$

Assuming the absence of dissipative losses (or independency of internal energy on deformation velocity), the internal energy per unit volume Φ could be expressed as expansion of strain invariants $\Phi(I_1, I_2, I_3)$:

$$\Phi = \Phi(0,0,0) + \left.\frac{\partial\Phi}{\partial I_1}\right|_0 I_1 + \left(\left.\frac{\partial\Phi}{\partial I_2}\right|_0 I_2 + \frac{1}{2}\left.\frac{\partial^2\Phi}{\partial I_1^2}\right|_0 I_1^2 \right) + \left[\left.\frac{\partial\Phi}{\partial I_3}\right|_0 I_3 + \frac{1}{2}\left.\frac{\partial^2\Phi}{\partial I_1 \partial I_2}\right|_0 I_1 I_2 + \frac{1}{6}\left.\frac{\partial^3\Phi}{\partial I_1^3}\right|_0 I_1^3 \right], \quad (2.4)$$

up to the third order of displacement gradients. In (2.4) the second-order terms are kept in parenthesis, and third-order terms are enclosed in square brackets. We can assume the $\Phi(0,0,0) = 0$ and $\partial\Phi/\partial I_1|_0 I_1 = 0$ — undeformed elastic body in equilibrium condition. For infinitesimal displacements of an isotropic body, introducing the Lamé constants λ and μ, the expression for Φ will take the form:

$$\Phi = \frac{\lambda}{2}u_{ii}^2 + \mu u_{ik}^2 \quad (2.5)$$

Finally, we could introduce the *generalized Hooke's law*:

$$\sigma_{ik} = \frac{\partial\Phi}{\partial\left(\frac{\partial u_i}{\partial x_k}\right)} = C_{ikjl}u_{jl} \quad (2.6)$$

where the fourth-order *elasticity tensor* C_{ikjl} is combined of Lamé constants.

Writing down the Newton's second law and substituting the (2.6) into the (2.1), one may finally obtain the linear equation of motion. This equation for elastic isotropic body with presence of *body forces* $\boldsymbol{f_b}$ could be written in a vector form:

$$\rho\ddot{\boldsymbol{u}} = \mu\Delta\boldsymbol{u} + (\lambda + \mu)\nabla(\nabla \cdot \boldsymbol{u}) + \boldsymbol{f_b}, \quad (2.7)$$

where ∇ is symbolic nabla operator. Being correct only for infinitesimal displacements, linearised model is used for most of the applications. Approximate ranges of applicability of linear theory of elasticity is given at Figure 2.1.

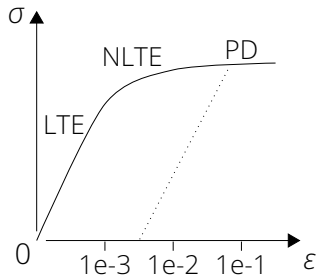


Figure 2.1: Schematic applicability ranges of linear and nonlinear elastic theory for metals. Here LTE stands for linear theory of elasticity, NLTE stands for nonlinear theory of elasticity, PD stands for permanent (irreversible) plastic deformations

2.2 Elastic waves in isotropic solids

2.2.1 Bulk waves

In absence of body forces ($f_b = 0$), the solution of the equation of motion (2.7) for linear isotropic media could be written in terms of two potentials:

$$u = u_L + u_T,\ u_L = \nabla\varphi,\ u_T = \nabla \times \Psi, \tag{2.8}$$

where φ and Ψ are scalar and vector potentials, correspondingly. Those potentials are functions of time and space variables. For a homogeneous medium after substitution of (2.8) into (2.7), the equation of motion could be splitted in two wave equations:

$$\frac{\partial^2\varphi}{\partial t^2} - c_L^2\Delta\varphi = 0;\ c_L^2 = \frac{\lambda + 2\mu}{\rho} \tag{2.9a}$$

$$\frac{\partial^2\Psi}{\partial t^2} - c_T^2\Delta\Psi = 0;\ c_T^2 = \frac{\mu}{\rho} \tag{2.9b}$$

Solutions of Equations 2.9 have a similar form:

$$\varphi = f(\boldsymbol{n}\cdot\boldsymbol{r} - c_L t);\ \Psi = F(\boldsymbol{n}\cdot\boldsymbol{r} - c_T t) \tag{2.10}$$

where $\boldsymbol{n}$ is a vector, perpendicular to the wave front. The simplest and most important solution — harmonic plane wave— has the form:

$$\varphi = A exp[i(\boldsymbol{k}\cdot\boldsymbol{r} - \omega t)];,\ \boldsymbol{k} = \omega\boldsymbol{n}/c_L; \tag{2.11a}$$

$$\Psi = \boldsymbol{B} exp[i(\boldsymbol{k}\cdot\boldsymbol{r} - \omega t)];,\ \boldsymbol{k} = \omega\boldsymbol{n}/c_T \tag{2.11b}$$

The plane wave 2.11a is called a *longitudinal* or *pressure* wave, whereas 2.11b is refereed to as *transversal* or *shear* wave. The vector $\boldsymbol{k}$ is a wave vector, c_L and c_T are the propagation velocities.

2.2.2 Surface acoustic waves (Rayleigh waves)

Special solution of the elastic wave, propagating along the boundary of solid and penetrating about one wavelength in depth of the medium, is named after J. W. Strutt, Lord Rayleigh, who was the first to theoretically describe it in 1887. We can consider a displacement field,

in a isotropic homogenous medium, filling the half-space X_3<0, associated with a linear SAW in a form:

$$\vec{u}(\vec{X},t)=\sum_{\vec{k}} e^{j(\vec{k}\cdot\vec{X}-\omega(\vec{k})t)}\vec{w}(X_3\,|\,\vec{k})A(\vec{k}). \tag{2.12}$$

where the vectors with tilde (i. e. $\vec{k}$) are 2D projections on OX_1X_2 plane. Functions $\vec{w}(X_3\,|\,\vec{k})$ are displacement depth profiles, which could be written in the following form:

$$\vec{w}(X_3\,|\,\vec{k})=\sum_{r=L,T} N_r \begin{pmatrix} \cos\alpha \\ \sin\alpha \\ j\frac{\rho\omega^2(\vec{k})-(\lambda+2\mu)\tilde{k}^2+\mu(\tilde{k}^2-(\omega/c_r)^2)}{\tilde{k}\sqrt{\tilde{k}^2-(\omega/c_r)^2}(\lambda+\mu)} \end{pmatrix} e^{\sqrt{\tilde{k}^2-(\omega/c_r)^2}X_3},$$

$$\text{where } N_L=1; N_T=\frac{\sqrt[4]{(\tilde{k}^2-(\omega/c_L)^2)(\tilde{k}^2-(\omega/c_T)^2)}}{\tilde{k}} \tag{2.13}$$

The coefficients in Equation (2.13) could be derived with substituting of (2.12) into the (2.9) and accounting the boundary conditions:

$$\sigma_{i3}\,|_{X_3=0}=0, i=1,2,3 \tag{2.14}$$

Finally the characteristic equation (or Rayleigh equation) for determination of Rayleigh wave velocity c_R could be given as:

$$\left(2-\frac{c_R^2}{c_T^2}\right)^2-4\sqrt{1-\frac{c_R^2}{c_T^2}}\sqrt{1-\frac{c_R^2}{c_L^2}}=0 \tag{2.15}$$

Therefore, Rayleigh waves are non-dispersive and their velocity is dependent only on *Poisson ratio* ν. For most of the real isotropic materials the solution of (2.15) could be approximated as followed:

$$\frac{c_R}{c_T}\sim\frac{0.87+1.12\nu}{1+\nu},\ \text{where } \nu=\frac{\lambda}{2(\lambda+\mu)}. \tag{2.16}$$

2.3 Reflection and refraction of elastic waves

One important particular case is the elastic wave propagation through a plane boundary between two media with different acoustic properties. Incident, reflected and refracted waves must satisfy four conditions of continuity on the stresses and the displacements. The unit propagation direction vectors of the system of incident, reflected and refracted waves are shown in Figure 2.2. Assuming the medium carrying the incident wave has Lamé constants λ, μ and density ρ, and the joined isotropic half-space could be characterized with λ', μ' and ρ', correspondingly. In the limiting case, the solution also describes the reflection at the medium-vacuum boundary and the related mode conversion.

Incident, reflected and refracted waves could be represented as:

$$\boldsymbol{u^{(n)}}=A_n\boldsymbol{d^{(n)}}exp(ik_n(x_1p_1^{(n)}+x_2p_2^{(n)}-c_nt)), \tag{2.17}$$

where n is an index, characterizing the wave (Figure (2.2)).

The expressions for directions of reflected and refracted waves could be derived from the Snell's law (Table 2.1).

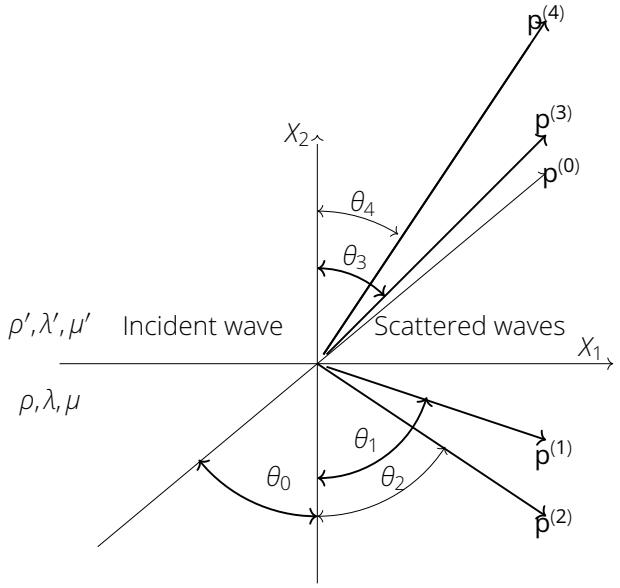


Figure 2.2: Plane elastic wave $\boldsymbol{p}^{(0)}$ refraction and reflection at boundary of two media. Angles and polarizations are given at Table 2.1.

Incident wave type $\boldsymbol{p}^{(0)}$ / Reflected& refracted waves	P $c_0 = c_L = \sqrt{\frac{\lambda+2\mu}{\rho}}$ $\boldsymbol{d}^{(0)} = \boldsymbol{p}^{(0)}$	SV $c_0 = c_T = \sqrt{\mu/\rho}$ $\boldsymbol{d}^{(0)} = \boldsymbol{i}_3 \wedge \mathrm{p}^{(0)}$	SH $c_0 = c_T = \sqrt{\mu/\rho}$ $\boldsymbol{d}^{(0)} = \boldsymbol{i}_3$
Reflected P-wave, $c_1 = c_L$ $\boldsymbol{p}^{(1)} = \boldsymbol{i}_1 \sin\theta_1 - \boldsymbol{i}_2 \cos\theta_1$	$\theta_1 = \theta_0$	$\sin\theta_1 = \frac{c_L}{c_T}\sin\theta_0$	-
Reflected S-wave, $c_2 = c_T$ $\boldsymbol{p}^{(2)} = \boldsymbol{i}_1 \sin\theta_2 - \boldsymbol{i}_2 \cos\theta_2$	SV, $\sin\theta_2 = \frac{c_T}{c_L}\sin\theta_0$	SV, $\theta_2 = \theta_0$	SH, $\theta_2 = \theta_0$
Refracted P-wave, $c_3 = c'_L$ $\boldsymbol{p}^{(3)} = \boldsymbol{i}_1 \sin\theta_3 + \boldsymbol{i}_2 \cos\theta_3$	$\sin\theta_3 = \frac{c'_L}{c_L}\sin\theta_0$	$\sin\theta_3 = \frac{c'_L}{c_T}\sin\theta_0$	-
Refracted S-wave, $c_4 = c'_T$ $\boldsymbol{p}^{(4)} = \boldsymbol{i}_1 \sin\theta_4 + \boldsymbol{i}_2 \cos\theta_4$	SV $\sin\theta_4 = \frac{c'_T}{c_L}\sin\theta_0$	SV $\sin\theta_4 = \frac{c'_T}{c_T}\sin\theta_0$	SH $\sin\theta_4 = \frac{c'_T}{c_T}\sin\theta_0$

Table 2.1: Polarization and direction of the reflected and refracted waves (Figure 2.2). P stands for pressure (longitudinal) wave, SV and SH stands for shear (transversal) wave with vertical and horizontal polarization, correspondingly. Here i_1, i_2 and i_3 are unit vectors.

For the case of $\theta_0 = 0$, it is convenient to introduce the *reflection* and *transmission* coefficients R and T, correspondingly:

$$R = \frac{Z' - Z}{Z' + Z} \text{ and} \tag{2.18a}$$

$$T = \frac{2Z'Z}{Z' + Z} \tag{2.18b}$$

where $Z = \rho C_L$ (or $Z = \rho C_T$, depending on wavetype) is the *acoustic impedance* of medium.

Calculation of amplitudes A_i for the general case is described below.

Amplitudes of reflected and refracted waves

Boundary conditions for two perfectly matched surfaces (as shown at Figure 2.2) could be written as follows:

$$\begin{aligned} u_1|_{x_2=0} &= u_1'|_{x_2=0}, \\ u_2|_{x_2=0} &= u_2'|_{x_2=0}, \\ \sigma_{12}|_{x_2=0} &= \sigma_{12}'|_{x_2=0}, \\ \sigma_{22}|_{x_2=0} &= \sigma_{22}'|_{x_2=0}, \end{aligned} \tag{2.19}$$

for displacements and stresses respectively. Following the Snell's law, the wave vector projection on axis X_1 should be equal for all wave components:

$$k^{(0)} \sin\theta_0 = k^{(1)} \sin\theta_1 = k^{(2)} \sin\theta_2 = k^{(3)} \sin\theta_3 = k^{(4)} \sin\theta_4 \tag{2.20}$$

Considering various types of incident waves, one may obtain the amplitude ratios with the *acoustic Fresnel equations*.

Incident P-wave

In case of the incident P-wave, using the relation

$$k^{(0)} c_L = k^{(1)} c_L = k^{(2)} c_T = k^{(3)} c_L' = k^{(4)} c_T' \tag{2.21}$$

one can rewrite Equations 2.19 for determination of reflected and refracted waves' amplitudes in the matrix form:

$$\begin{bmatrix} -\sin\theta_1 & -\cos\theta_2 & \sin\theta_3 & -\cos\theta_4 \\ \cos\theta_1 & -\sin\theta_2 & \cos\theta_3 & \sin\theta_4 \\ \sin 2\theta_1 & \frac{c_L}{c_T}\cos 2\theta_2 & \frac{\mu'}{\mu}\frac{c_L}{c_L'}\sin 2\theta_3 & -\frac{\mu'}{\mu}\frac{c_L}{c_T'}\cos 2\theta_4 \\ -\left(\frac{c_L}{c_T}\right)^2\cos 2\theta_2 & \frac{c_L}{c_T}\sin 2\theta_2 & \frac{\mu'}{\mu}\frac{c_L}{c_L'}\left(\frac{c_L'}{c_T'}\right)^2\cos 2\theta_4 & \frac{\mu'}{\mu}\frac{c_L}{c_T'}\sin 2\theta_4 \end{bmatrix} \begin{bmatrix} A_1 \\ A_2 \\ A_3 \\ A_4 \end{bmatrix} = A_0 \begin{bmatrix} \sin\theta_0 \\ \cos\theta_0 \\ \sin 2\theta_0 \\ \left(\frac{c_L}{c_T}\right)^2\cos 2\theta_2 \end{bmatrix} \tag{2.22}$$

Incident SV-wave

Since the indices and polarizations of reflected and refracted waves keep the same, only the RHS terms in Equation 2.22 have to be changed to:

$$A_0 \begin{bmatrix} -\cos\theta_0 \\ \sin\theta_0 \\ -\cos 2\theta_0 \\ \sin 2\theta_0 \end{bmatrix} \tag{2.23}$$

Incident SH-wave

If $p^{(0)}$ is the shear wave with horizontal polarization, only the u_3 components and σ_{23} stresses are present. In this case both reflected and refracted waves are also SH waves. The amplitude ratios could be computed as:

$$\begin{aligned} \frac{A_2}{A_0} &= \frac{\mu\cos\theta_0 - \mu'(c_T/c_T')\cos\theta_4}{\mu\cos\theta_0 + \mu'(c_T/c_T')\cos\theta_4}, \\ \frac{A_4}{A_0} &= \frac{2\mu\cos\theta_0}{\mu\cos\theta_0 + \mu'(c_T/c_T')\cos\theta_4}, \end{aligned} \tag{2.24}$$

If θ_1, θ_3 or θ_4 is equal to $\pi/2$, the *grazing* waves, travelling along the X_1 direction are generated. In this case the angle θ_0 is called the *critical* angle. If the angle of incidence of the initial wave exceeds the *critical angle*, inhomogeneous decaying plane wave components (head waves) would also appear.

2.4 Nonlinear theory of elasticity: account of third-order terms

The equations of elasticity theory are generally nonlinear [Zar66], therefore the propagation of elastic waves is accompanied by a nonlinear distortion of the wave profile as well as the interaction of elastic waves in solids. The interaction forces between atoms, molecules and ions in solids nonlinearly depend on the displacement of the particle from its equilibrium position. Hence thermal vibrations of atoms or ions in a crystal lattice are anharmonic, and this anharmonicity leads to the interaction of thermal phonons of the lattice. The possibility of phonon-phonon interaction also gives a description of the thermal conductivity of solids and the absorption of sound. This nonlinearity at the molecular level also reveals itself in nonlinear elasticity for macroscopic processes.

At certain level of mechanical stresses, deviations from the proportionality between strain and stress (the violation of linear elasticity theory - Hooke's law) begin (Figure 2.1). These characteristics of solids depend on several factors: first, the intermolecular forces that depend on the displacement of the molecules are nonlinear. Second, crystals and polycrystals contain various types of defects and dislocations, microcracks and vacancies, which also contribute to the deviation from the linear Hooke's law.

The *strain matrix* η could be defined with Jacobian matrix $J = \frac{(x_1', x_2', x_3')}{(x_1, x_2, x_3)}$ [Mur51]:

$$\eta = \frac{1}{2}(J^* J - E_3), \tag{2.25}$$

where E_3 is a 3x3 identity matrix and asterisk denotes the conjugate transpose (Hermitian transpose). The invariants of η could be written as followed:

$$\begin{aligned} \widehat{I_1} &= \mathrm{Tr}(\eta) = \eta_{11} + \eta_{22} + \eta_{33}, \\ \widehat{I_2} &= \frac{1}{2}(\eta_{ii}\eta_{jj} - \eta_{ij}\eta_{ji}), \\ \widehat{I_3} &= \det(\eta). \end{aligned} \tag{2.26}$$

Therefore, if the strain matrix is infinitesimal, the subindex of invariant displays the order of smallness of each parameter. The energy of deformation per unit volume could be expanded as:

$$\begin{aligned} \varphi &= \varphi_0 + \varphi_1 + \varphi_2 + \varphi_3 + \ldots, \text{ where} \\ \varphi_1 &= const * \widehat{I_1}; \\ \varphi_2 &= \frac{\lambda + 2\mu}{2}\widehat{I_1}^2 - 2\mu\widehat{I_2}; \\ \varphi_3 &= \frac{l + 2m}{3}\widehat{I_1}^3 - 2m\widehat{I_1}\widehat{I_2} + n\widehat{I_3}, \end{aligned} \tag{2.27}$$

where l, m, n are third-order elastic constants in Murnaghan notation. Another notations, such as A, B, C – Landau notation [L.D44], and ν_1, ν_2, ν_3 – Lamé notation are also used. All TOEC triplets are linearly related with each other:

$$\begin{bmatrix} l \\ m \\ n \end{bmatrix} = \begin{bmatrix} 0.5 & 1 & 0 \\ 0 & 1 & 2 \\ 0 & 0 & 4 \end{bmatrix} \begin{bmatrix} \nu_1 \\ \nu_2 \\ \nu_3 \end{bmatrix} = \begin{bmatrix} 0 & 1 & 1 \\ 0.5 & 1 & 0 \\ 1 & 0 & 0 \end{bmatrix} \begin{bmatrix} A \\ B \\ C \end{bmatrix} \tag{2.28}$$

The nonlinear equation of motion could be written as followed:

$$\rho\frac{\partial^2 u_i}{\partial t^2} = \frac{\partial \sigma_{ik}}{\partial x_k} = \frac{\partial}{\partial x_k}\left(\frac{\partial \varphi}{\partial\left(\frac{\partial u_i}{\partial x_k}\right)}\right), \tag{2.29}$$

where σ_{ik} is the first Piola-Kirchhoff stress tensor.

By substituting the Equation (2.27) in (2.29), one may obtain this equation in explicit form:

$$\rho_0\frac{\partial^2 u_i}{\partial t^2} - \mu\frac{\partial^2 u_i}{\partial x_k^2} - (\lambda+\mu)\frac{\partial^2 u_l}{\partial x_l \partial x_i} = F_i, \tag{2.30}$$

where F_i is the i-th component of the nonlinear force per unit volume of the undeformed medium:

$$\begin{aligned} F_i = (\mu + n/4)&\left(\frac{\partial^2 u_l}{\partial x_k^2}\frac{\partial u_l}{\partial x_i} + \frac{\partial^2 u_l}{\partial x_k^2}\frac{\partial u_i}{\partial x_l} + 2\frac{\partial^2 u_i}{\partial x_l \partial x_k}\frac{\partial u_l}{\partial x_k}\right) \\ &+ (\lambda+\mu+m-n/4)\left(\frac{\partial^2 u_l}{\partial x_i \partial x_k}\frac{\partial u_l}{\partial x_k} + \frac{\partial^2 u_k}{\partial x_i \partial x_k}\frac{\partial u_i}{\partial x_l}\right) + (\lambda+m-n/2)\frac{\partial^2 u_l}{\partial x_k^2}\frac{\partial u_l}{\partial x_l} \\ &+ (m-n/4)\left(\frac{\partial^2 u_k}{\partial x_l \partial x_k}\frac{\partial u_l}{\partial x_i} + \frac{\partial^2 u_l}{\partial x_i \partial x_k}\frac{\partial u_k}{\partial x_l}\right) + (2l-m-n/2)\frac{\partial^2 u_k}{\partial x_l \partial x_k}\frac{\partial u_l}{\partial x_l} \end{aligned} \tag{2.31}$$

2.5 Acoustoelastic effect

2.5.1 BW AEC

In the general case of elastic wave propagation in an isotropic body, strained with uniaxial load (the load direction is defined as '1' for convention), dimensionless acoustoelastic constants can be defined as follows:

$$L_{ij} = \frac{\delta V_{ij}/V^0}{\delta\varepsilon} \tag{2.32}$$

where the first subindex shows the wave propagation direction in a Cartesian coordinate system, and the second subindex shows the particle displacement direction for a given wave. ε is a strain level in direction '1', and V^0 stands for the velocity of the same wave at zero axial strain.

The analytical expressions for the variation of velocity of the bulk wave in a pre-stressed isotropic solid were published by Hughes and Kelly [Hug53], based on Murnaghan's theory of finite deformations of solids [Mur51]:

$$\begin{aligned} L_{11} &= 2 + \frac{\mu + 2m + \nu\mu(1+2l/\lambda)}{\lambda+2\mu}, \\ L_{12} &= 2 + \frac{\nu n}{4\mu} + \frac{m}{2(\lambda+\mu)}, \\ L_{21} &= \frac{\lambda+2\mu+m}{2(\lambda+\mu)} + \frac{\nu n}{4\mu} \\ L_{22} &= -2\nu\left(1 + \frac{m-\mu l/\lambda}{\lambda+2\mu}\right), \\ L_{23} &= \frac{m-2\lambda}{2(\lambda+\mu)} - \frac{n}{4\mu}, \end{aligned} \tag{2.33}$$

where ν is the Poisson ratio. A detailed derivation of Equations (2.33) is given in Appendix 8.1.

2.5.2 RW AEC definitions and calculation from TOEC

Following the works [Iwa78; May95], the transition from TOEC, estimated from the measurements of Bulk Wave (BW) AEC, to the Rayleigh wave acoustoelastic constants for a semi-infinite homogeneous elastic medium, can be done through the definition of the Grüneisen constants:

$$\gamma_{LM}(q) = -\left[\omega_q^{-1}\frac{\partial\omega_q}{\partial E_{LM}}\right]_{(E_{JK}=0)}, \tag{2.34}$$

where E_{LM} represent homogeneous strains ([May95], Eq. 4.21).

For an isotropic medium, the equation for the relative change in velocity of a Rayleigh wave will take the form [Iwa78; May95]:

$$\frac{\delta V_R}{V_R} = (1/h_0)(hE_{LL} + h_2E_{22}), \tag{2.35}$$

where coefficients h/h_0 and h_2/h_0 are dependent on Second-Order Elastic Constant (SOEC), TOEC and velocities of bulk and Rayleigh waves. Explicit algebraic expressions for these coefficients are given in the Appendix 8.2

For experimental measurements of acoustoelastic constants it is convenient to express RW AEC as a function of stress rather than strain [Duq02]. In this case the relative variation on velocity could be then expressed in terms of static stress:

$$\begin{aligned}
&\frac{\delta V_R}{V_R^0} = A_{R12}^{(1)}\sigma_{11} + A_{R12}^{(3)}\sigma_{33}, \text{ where}\\
&A_{R12}^{(1)} = \frac{1}{M}\left[\frac{N_1}{2}\left(\frac{\alpha_1}{\alpha_0}+1-\frac{C_{12}}{C_{23}}\right)+\frac{N_2}{2}\left(\frac{\alpha_2}{\alpha_0}+1-\frac{C_{22}}{C_{23}}\right)\right],\\
&A_{R12}^{(3)} = \frac{1}{M}\left[\frac{N_3}{2}\left(\frac{\alpha_1}{\alpha_0}+1-\frac{C_{12}}{C_{23}}\right)+\frac{N_4}{2}\left(\frac{\alpha_2}{\alpha_0}+1-\frac{C_{22}}{C_{23}}\right)\right],\\
&M = C_{11}N_1 + C_{12}N_2 + C_{13}N_3;\\
&N_1 = C_{22}C_{33} - C_{23}^2, N_2 = C_{13}C_{23} - C_{12}C_{33}, N_3 = C_{12}C_{23} - C_{13}C_{22};\\
&N_4 = C_{11}C_{33} - C_{13}^2, N_5 = C_{12}C_{13} - C_{11}C_{23}, N_6 = C_{11}C_{22} - C_{12}^2.
\end{aligned} \tag{2.36}$$

Here t^l is the Cauchy stress tensor element, and C_{ij} are second-order elastic constants in Voigt notation. Constants α_0 and α_1 are defined as in [Hay61; Hir81]:

$$\begin{aligned}
\alpha &= \alpha_0 + \alpha_1 u_{11} + \alpha_2 u_{33}, \text{ where } \alpha \equiv \rho V^2\\
\delta V_R/V_R^0 &= (\alpha_1/2\alpha_0)u_{11} + (\alpha_2/2\alpha_0 - \mu/\lambda)u_{33},
\end{aligned} \tag{2.37}$$

2.6 Rayleigh wave velocity dispersion inversion for stress measurement

The dependency of Rayleigh wave' propagation velocity on stress makes it a prospective mean on in-situ evaluation of residual stress depth profile (Figure 1.4) by measuring the Rayleigh wave velocity dispersion. However, the solution of the inverse problem, i.e. reconstructing the stress distribution profiles from the measurement of velocity dispersion or *phase shift* $\delta\varphi(\omega)$ of RW due to presence of the static stress fiield, is facing several difficulties. In particular, the analytical solution exist only for stress profiles, which could be expressed as polynomials in the depth coordinate [Dit96; Dit97].

Using an expression for the phase shift of the Rayleigh wave velocity in an unstressed medium and a stressed medium in the form [Hus85]:

$$\delta\varphi(\omega) = -\frac{\omega}{4P}\int_{X\in V} G(\boldsymbol{X},\omega)d^3\boldsymbol{X}, \tag{2.38}$$

where ω denotes circular frequency, V denotes volume in undeformed coordinate system, and P denotes the average over one time period of power flux per unit width, perpendicular to the travel direction. P could be expressed in terms of the product of the Rayleigh wave group velocity and its kinetic energy density. General form of integral equations for two particular cases - uniaxially applied stress field along and across the RW propagation direction could be written as followed [Dit97]:

$$\delta\varphi^{22}(\omega) = -\frac{L_0\omega}{4P}\int_{-\infty}^{0} a_i^{||}F_i(X_3,\omega)\sigma_{22}(X_3)dX_3, \tag{2.39a}$$

$$\delta\varphi^{21}(\omega) = -\frac{L_0\omega}{4P}\int_{-\infty}^{0} a_i^{\perp}F_i(X_3,\omega)\sigma_{11}(X_3)dX_3, \tag{2.39b}$$

where $i \in \{1,...,5\}$, F_i and a_i are functions, dependent on frequency and SOEC/TOEC, and L_0 is the RW propagartion distance. Superscripts $\delta\varphi^{a\beta}$ are denoting the change in phase of the Rayleigh wave, propagating in direction a, caused by uniaxial stress in β direction. Explicit form of F_i and a_i are given in Appendix 8.3.

Given only the first order approximation for the acoustoelastic effect, the phase shift is a linear function of the stress distribution. The corresponding change in phase velocity can be calculated using the relation:

$$\frac{\delta V}{V} = u_{22} - \frac{\delta\varphi^{22}V_0}{\omega L_0}, \tag{2.40}$$

where u_{22} denotes the surface strain in the direction of propagation. A detailed analysis of the biaxial stress case, considered as the sum of two separate stress states, can be found in [Dit97].

2.7 Nonlinear interaction of elastic waves in solids

In linear theory of elasticity (Section 2.1), the field of two acoustic waves in a given solid volume is a linear superposition of the input wave fields [Lan86]. Given finite deformations, besides the superposition of two initial waves with frequencies ω_1 and ω_2, secondary waves of mixed frequency $\pm p\omega_1 \pm q\omega_2$ generated by material nonlinearity are also expected (p and q are natural numbers).

The nonlinear wave interaction effect, also called elastic wave scattering or wave mixing, has been theoretically described [Jon63; Tay64; Nor79] and observed experimentally [Rol64; Tan73; Dem14] for isotropic and anisotropic materials.

In order to effectively generate an elastic wave with an angular frequency ω_3 through a second order nonlinearity at the desired mixed frequency in a finite volume, phase matching (or resonance) conditions must be fulfilled:

$$\omega_3 = \omega_1 \pm \omega_2, \tag{2.41a}$$

$$\vec{k}_3 = \vec{k}_1 \pm \vec{k}_2, \tag{2.41b}$$

where $\vec{k}_i$, (i=1, 2, 3), are the wave vectors of the three involved waves. Analysis of the allowed interactions and scattering intensities for bulk waves was first performed by Jones and

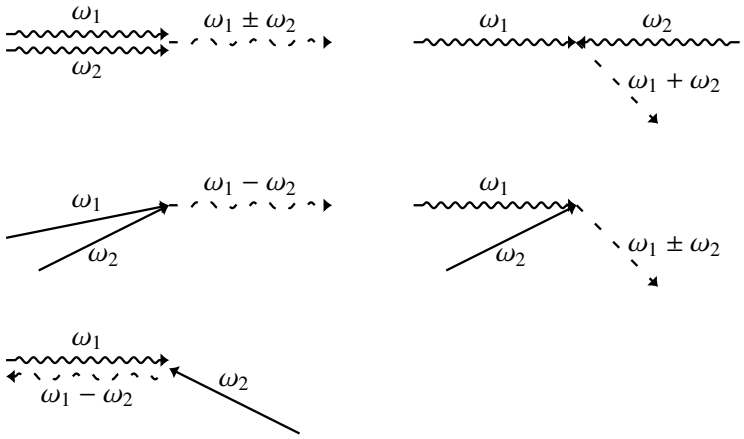


Figure 2.3: Allowed bulk wave-surface wave resonant interactions, presented by Stegeman and Nizzoli [F. 84]. Straight lines represent bulk waves, curly lines denote surface waves, and solid and dashed lines indicate initial and scattered waves, respectively.

Kobett [Jon63]. Additional polarization restrictions and allowed cases for bulk waves are given in Appendix 8.4.

The inclusion of Rayleigh waves as possible interaction members requires additional considerations. As the mixing volume is limited to the RW penetration depth, the presence of a free surface breaks the translational symmetry normal to the surface. Therefore, Equation (2.41b) can be rewritten as:

$$\vec{\kappa}_3 = \vec{\kappa}_1 \pm \vec{\kappa}_2, \tag{2.42}$$

where for bulk waves $\vec{\kappa}_i = \vec{\tilde{k}}_i$ – the projection of $\vec{k}$ onto the *OXY* plane, parallel to the surface; and $\vec{\kappa}_i = \vec{k}_i$ for RW. The corresponding analysis of the resonant[1] interactions of bulk and surface waves in isotropic solids has been performed by Stegeman and Nizzoli [F. 84]. Assuming $\omega_1 > \omega_2$, the allowed interactions are shown in Figure 2.3, where straight and curly lines represent bulk and Rayleigh waves, and solid and dashed lines denote the initial and scattered waves, respectively.

The analysis of nonlinear surface wave phenomena has two major complications. First, description of the three-dimensional displacement field demands the parametrisation, alike shown at Equation (2.12) and (2.13). The second complication is the existence of *nonlinear* boundary conditions (Equations (2.56) and (2.64)): mixing of two or more waves results in a net stress on the surface at the mixing frequencies, and the solutions must contain terms to ensure the surfaces are indeed stress-free to first order at the mixing frequencies.

In this work two cases are considered to calculate the scattering efficiency of an elastic wave from the angle between the original waves and the frequency ratio (Figure 2.4).

- Case 1: calculation of the scattering efficiency of an elastic wave away from the interaction region using the perturbation theory described in [May95].
- Case 2: calculation of displacement amplitudes directly at the boundary of the interaction region. This option is convenient for comparison with the results of the experiment carried out with LDV. These calculations were performed using the extension of model [May95], presented in work [Gar22].

[1] The low-loss leaky modes are not considered there

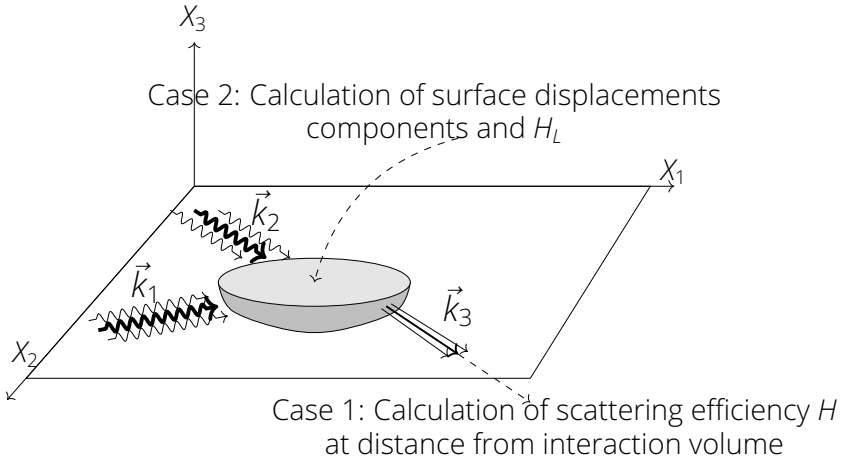


Figure 2.4: Two cases of nonlinear wave interaction' intensity evaluation. Here the interaction volume is shaded with grey, k_1 and k_2 are wavevectors of initial waves. Cases 1 and 2 are related to calculation of H and H_L, correspondingly.

Case 1. Evaluation of intensity of the nonlinear wave interaction in the far field

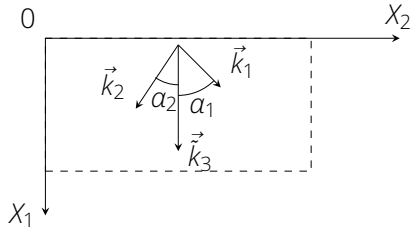
For the evaluation of wave scattering efficiency at some distance from the interaction volume, the perturbation theory [May95] was used.

First Piola–Kirchhoff stress tensor σ may be expanded with respect to the powers of displacement gradient components:

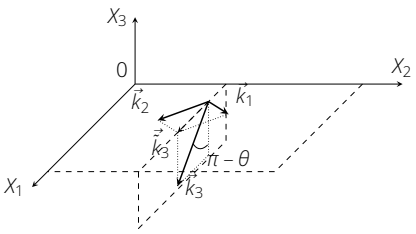
$$\sigma_{LI} = \frac{\partial \Phi}{\partial u_{I,L}} = C_{ILmM} u_{m,M} + \frac{1}{2} S_{ILmMnN} u_{m,M} u_{n,N} + \ldots, \tag{2.43}$$

where the fourth-rank tensor C contains the second-order elastic constants (SOEC, or the Lamé constants λ and μ for isotropic materials), and the sixth-rank tensor S depends on the second- and third-order elastic constants (or l, m, and n for isotropic materials) [Lei60]. Compared to the conventional linearised strain–displacement relation (Equation (2.2)), the Green-Lagrange strain tensor E contains the additional product of displacement gradients $u_{j,A} u_{j,B}$, leading to additional nonlinear terms:

$$E_{AB} = \frac{1}{2} \left[\left(\delta_{jA} + u_{j,A} \right) \left(\delta_{jB} + u_{j,B} \right) - \delta_{AB} \right]. \tag{2.44}$$



(a) Definition of angles: $\alpha = \angle(\vec{k}_1, \vec{k}_2)$, $\alpha_i = \angle(\overrightarrow{OX_1}, \vec{k}_i)$ ($\alpha_1 > 0$, $\alpha_2 < 0$, $\vec{k}_3 \,||\, OX_1$)



(b) Definition of angle $\theta = \angle(\vec{k}_3, \overrightarrow{OX_3})$.

Figure 2.5: Definition of angles and coordinate system

Here E_{AB} is defined in terms of gradients $u_{j,B} = \partial u_j / \partial X_B$ of the displacement vector $\vec{u}$,

$$\vec{u}(\vec{X}, t) = \vec{x}(\vec{X}, t) - \vec{X}. \tag{2.45}$$

The coordinate system was defined such that the X_3-axis is oriented normally to the surface, and the X_1-axis was parallel to the projection of $\vec{k}_3$ to the surface (see Figure 2.5). The solid fills the half-space X_3<0. With these definitions, the equation of motion and the nonlinear boundary conditions can be written as

$$\rho \ddot{u}_l(\vec{X}, t) = \sigma_{LI,L}(\vec{X}, t), \tag{2.46}$$

$$\sigma_{3l}(\vec{X})\Big|_{X_3=0} = 0, \tag{2.47}$$

where ρ is the material density in the undeformed state.The general expression for the input waves can be written as

$$\vec{u}(\vec{X}, t) = e^{i(\vec{k}\cdot\vec{\vec{X}}-\omega t)}\vec{w}(X_3 \mid \vec{\vec{k}})A + c.c., \tag{2.48}$$

where $\vec{\vec{X}}$ is the projection of $\vec{X}$ onto OX_1X_2, the function $\vec{w}(X_3 \mid \vec{k})$ describes the displacement profiles for bulk (2.3) and surface waves (2.2.2), and *c.c.* denotes the complex conjugate. Neglecting attenuation, the displacement field at the sum/difference frequency may be decomposed into two parts, described by two summands in the curly brackets:

$$\vec{u}_3(\vec{X}, t) = e^{i(\vec{\vec{k}}_3\cdot\vec{\vec{X}}-\omega_3 t)}\left\{\sum_j e^{-ik_j X_3}\vec{W}(j)\widehat{H^{(j)}} + \vec{w}^{(loc)}(X_3)\right\}A_1A_2 + c.c. \tag{2.49}$$

The first part is the sum of linearly polarized plane waves, labelled by j, which are propagating away from the surface and having the unit polarization vectors $\vec{W}(j)$. The second part is a surface-localized component, which decays to zero exponentially in the negative X_3-direction. In (2.49) q_j denotes the X_3-component of the three-component wavevector of the j-th plane bulk wave (Equation 2.7 and [May95], (5.54)). This case, the scattering efficiency for this bulk wave is defined as the quantity $\widehat{H^{(j)}}$.

If the resonant conditions of Eq. (2.41) are fulfilled and the scattered wave type is SAW, solution could be found in a form

$$\vec{u}_3(\vec{X}, t) = e^{i(\vec{\vec{k}}_3\cdot\vec{\vec{X}}-\omega_3 t)}(\vec{w}(X_3 \mid \vec{k}_3))(-i)\hat{h}X + \zeta(\vec{w}(X_3 \mid \vec{k}_3)) + c.c. \tag{2.50}$$

By inserting Eq. (2.50) into the equation of motion (2.46), projecting on $\vec{w}(X_3 \mid \vec{k})$, integrating by parts and with use of nonlinear boundary conditions at the surface, one could get the expression for the efficiency $\hat{h}$ of Rayleigh wave generation through nonlinear interaction of two waves:

$$\hat{h} = \frac{\omega_3}{S_R} S_{lLmMnN}\int_{-\infty}^{0}[\hat{Q}_L(-\vec{k}_3)w_l(X_3 \mid \vec{k}_3)]^*[\hat{Q}_M(\vec{k}_2)w_m(X_3 \mid \vec{k}_2)][\hat{Q}_N(\vec{k}_1)w_n(X_3 \mid \vec{k}_1)]dX_3 \tag{2.51}$$

If the scattered wave is a bulk wave, its wave vector can be written as $\vec{k}_3 = (\vec{\vec{k}}_3, -k)$:

$$\vec{u}_3(\vec{X}, t) = e^{i(\vec{k}_3\cdot\vec{X}-\omega_3 t)}(\vec{W}(\vec{k_{3j}})e^{-ikX_3} + \zeta(X_3)) + c.c. \tag{2.52}$$

and the solution for $\widehat{H}$ (component of complex amplitude B of scattered bulk wave: $B = \widehat{H}A_1A_2$), could be represented as:

$$\widehat{H} = \frac{i\omega_3}{S_B} S_{lLmMnN} \int_{-\infty}^{0} [\hat{Q}_L(-\vec{k}_3) w_l(X_3 \mid -\vec{k}_3 J)][\hat{Q}_M(\vec{k}_2) w_m^{(II)}(X_3)][\hat{Q}_N(\vec{k}_1) w_n^{(I)}(X_3)] dX_3, \tag{2.53}$$

where additional operator $\hat{Q}_L = \delta_{L1} iq_1 + \delta_{L2} iq_2 + \delta_{L3} \frac{\partial}{\partial X_3}$ was used. Here the functions $w_l(X_3 \mid -\vec{k}_3 J)$ are displacement fields of a bulk modes, defined through the solution of a linear reflection problem at the free boundary (Section 2.3).

For both cases, S_R and S_B are averages of energy flux per unit length for scattered waves:

$$\begin{aligned} S_R &= 2\omega_3 C_{j1mM} Im \left(\int_{-\infty}^{0} w_j^*(X_3 \mid k_3) \hat{Q}_M(k_3) w_m(X_3 \mid k_3) dX_3 \right) \\ S_B &= 2\omega_3 C_{m3nN} K_N W_m(\vec{k}_3 J) W_n(\vec{k}_3 J) \end{aligned} \tag{2.54}$$

Therefore, scattered wave efficiency could be expressed through decay profiles and wave vector components of initial waves. Later both the coefficients $\hat{h}$ and $\widehat{H}$ will be referred to as the scattering efficiencies H.

Case 2. Calculation of scattering efficiency on the surface of interaction layer

The perturbation theory formulation described earlier provides an estimation of the efficiency of generation of a bulk wave of the form (2.49). The near-surface displacement field on the border of wave overlapping volume can be calculated through perturbation theory, as outlined below[2].

The interaction area and zone of scattered' wave evaluation are shown in Figure 2.4. Here, the wave field generated by material nonlinearity did not yet evolve into a plane wave. Within perturbation theory, the bulk wave displacement field generated by second-order nonlinearity may be determined from the equation of motion:

$$\rho \ddot{u}_l^{(B)} - \frac{\partial}{\partial X_L} C_{lLmM} u_{m,M}^{(B)} = \frac{\partial}{\partial X_L} S_{lLmMnN} u_{m,M}^{(I)} u_{n,N}^{(II)}, \tag{2.55}$$

and boundary conditions at the surface

$$-C_{l3mM}\, u_{m,M}^{(B)}\Big|_{X_3=0} = S_{l3mMnN} u_{m,M}^{(I)} u_{n,N}^{(II)}, \tag{2.56}$$

where $u^{(I)}$ and $u^{(II)}$ are the displacement fields of two input waves [Aul73].

In particular, to calculate the displacement field generated by the nonlinear mixing of two Rayleigh waves, one must find a particular solution for the equation of motion (Equation 2.55) in the following form:

$$\vec{u}^{(p)}(\vec{X}, t) = e^{i(KX_1 - \omega_3 t)} \vec{u}^{(p)}(X_3) + c.c, \text{ where } \vec{u}^{(p)}(X_3) = \sum_{r,r'=L,T} \vec{b}^{(3)}(r, r') e^{(k_1 \hat{a}_r + k_2 \hat{a}_{r'}) X_3}, \tag{2.57}$$

where L and T stand for longitudinal and transverse. Thus, one can rewrite the equation of motion (2.55) for vectors $\vec{b}^{(3)}(r, r')$ as:

$$\left(\rho \omega_3^2 \delta_{lm} + C_{lLmM} Q_L^{(3P)}(r, r') Q_M^{(3P)}(r, r') \right) b_m^{(3)}(r, r') = R_l(r, r'), \tag{2.58}$$

where

$$R_l(r, r') = -S_{lLmMnN} Q_L^{(3P)}(r, r') b_m^{(1)}(r) Q_M^{(1)}(r) b_n^{(2)}(r') Q_N^{(2)}(r'). \tag{2.59}$$

[2] In this section the results, published in a collaborative paper [Gar22], are presented.

Here, $\widehat{a}_r = \sqrt{1-\left(\frac{V_R}{V_r}\right)^2}$, $r, r' = L, T$, and V_R and V_r are the RW and bulk wave velocities, correspondingly. The displacement field of the two incoming Rayleigh waves ($\Lambda = 1, 2$) is given by

$$\vec{U}^{(\Lambda)}(\vec{X}, t) = N_\Lambda e^{i\left(\vec{k}_\Lambda \vec{X} - \omega_\Lambda t\right)} \left(\underbrace{\begin{bmatrix} \cos(a_\Lambda) \\ \sin(a_\Lambda) \\ -i\widehat{a}_L \end{bmatrix}}_{\vec{b}^{(\Lambda)}(L)} e^{k_\Lambda \widehat{a}_L X_3} + \underbrace{\begin{bmatrix} -\sqrt{\widehat{a}_L \widehat{a}_T}\cos(a_\Lambda) \\ -\sqrt{\widehat{a}_L \widehat{a}_T}\sin(a_\Lambda) \\ i\sqrt{\widehat{a}_L / \widehat{a}_T} \end{bmatrix}}_{\vec{b}^{(\Lambda)}(T)} e^{k_\Lambda \widehat{a}_T X_3} \right) + c.c., \tag{2.60}$$

where N_1 and N_2 are RW amplitudes. We define:

$$\vec{Q}^{(\Lambda)}(r) = \begin{pmatrix} ik_{\Lambda,1} \\ ik_{\Lambda,2} \\ k_1 \widehat{a}_r \end{pmatrix} \text{ and } \vec{Q}^{(3P)}(r, r') = \begin{pmatrix} iK \\ 0 \\ k_1 \widehat{a}_r + k_2 \widehat{a}_{r'} \end{pmatrix}, \tag{2.61}$$

where K is the magnitude of the projection of the wave vector on the OX_1X_2 plane. Finding a solution $\vec{u}^{(h)}(\vec{X}, t) = e^{i(kX_1 - \omega_3 t)} \vec{u}^{(h)}(X_3) + c.c.$ to the homogeneous equation of motion, in order to satisfy the traction-free boundary condition on the surface:

$$\vec{u}^{(h)}(X_3) = \sum_{j=P,\ SV,\ SH} \vec{a}^{(j)} e^{-iq_j X_3}, \tag{2.62}$$

where q_j is either real and positive or imaginary with a positive imaginary part, following $q_j^2 = \left(\frac{\omega_3}{V_j}\right)^2 - K^2$. The vectors, $\vec{a}^{(j)}$, may be chosen as

$$\vec{a}^{(P)} = \begin{pmatrix} K \\ 0 \\ -q_p \end{pmatrix} \frac{p_P}{\sqrt{K^2 + |q_P|^2}},\ \vec{a}^{(SV)} = \begin{pmatrix} q_{SV} \\ 0 \\ K \end{pmatrix} \frac{p_{SV}}{\sqrt{K^2 + |q_{SV}|^2}},\ \vec{a}^{(SH)} = \begin{pmatrix} 0 \\ 1 \\ 0 \end{pmatrix} p_{SH}. \tag{2.63}$$

The projections p_P, p_{SV}, and p_{SH} are obtained from the boundary condition at the surface:

$$\sum_{j=P,\ SV,\ SH} C_{l3mM} Q_M^{(3h)}(j) a_m^{(j)} + \sum_{r,r'=L,T} C_{l3mM} Q_M^{(3P)}(r, r') b_m^{(3)}(r, r') + \sum_{r,r'=L,T} S_{l3mMnN} Q_M^{(1)}(r) b_m^{(1)}(r) Q_N^{(2)}(r') b_n^{(2)}(r') = 0. \tag{2.64}$$

Here, we define $\vec{Q}^{(3h)}(j) = \begin{pmatrix} iK \\ 0 \\ -iq_j \end{pmatrix}$.

Finally, the local scattering efficiency H_L is introduced, as a suitable mean of comparison between perturbation theory results and other investigation methods, such as Finite Element Modelling (FEM) simulations, and experimental measurements of displacement field at the interaction area. For all the aforementioned cases, H_L is defined as

$$H_L = \frac{A_3(\omega_1 + \omega_2)}{A_3(\omega_1) A_3(\omega_2)}, \tag{2.65}$$

where $A_3(\omega)$ is the amplitude of the X_3-component of the surface displacement at the frequency ω. Similar to the definition of H in Equation (2.49), H_L has the dimension of inverse length.

3 Methodology

This section describes the numerical studies, the experiments carried out and the developed and verified data processing algorithms. These algorithms and procedures have been established both for improving the accuracy and reliability of measured physical values and for visualisation of experimental data and advanced analysis of FEM data.

The practical part of the work consisted of several main tasks:

1. Study of TOEC/AEC evaluation precision with two available methods (direct measurements and mapping from bulk wave measurements) for *available* industrial grade equipment for materials of interest (Ni-Cr19-Fe19-Nb5-Mo alloy (In718) and Ti-6Al-2Sn-4Zr-6Mo alloy (Ti6246)) and direct measurements of surface-treated acoustoelastic constants.
2. Investigation of RW dispersion measurement limitations using the problem-specific device: High precision Ultrasonic GOniometer (HUGO) for materials of interest (In718 and Ti6246)
3. Design of independent method for evaluation of TOEC (RW AEC) in surface layer:
    a) Numerical study for optimization of experiment' layout
    b) Case study: contactless measurements of nonlinear interaction on metal surface

In addition, feasibility study of fully noncontact excitation and sensing using laser ultrasound have been performed and analysed. To ensure the robustness of measured parameters extraction, several data processing algorithms have been developed, tested and applied in this work. As a part of validation, independent implementation of processing routines in MATLAB and Python 3.7 enviroments have been performed.

3.1 AEC measurements

Two types of samples, machined from In718 and Ti6246 were used for bulk wave and Rayleigh wave acoustoelastic constants evaluation (Figure 3.1). For BW AEC measurements the Type 1 samples were used; for RW AEC measurements both Type 1 and Type 2 samples have been used. In addition to measurements in initial sample state (annealed), samples have been also plastically deformed and examined. Finally, after annealing, direct RW AEC measurements of treated components have been done, as dedicated sample areas have been shot-peened with 5A (mild) and 8A (high) intensity.

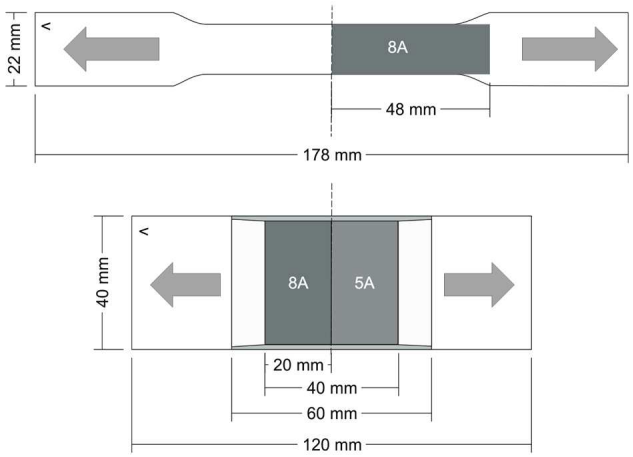


Figure 3.1: Geometry of different sample types and shot-peening scheme. Type 1 (upper) is treated from both sides with intensity 5A and 8A. Type 2 (bottom) is peened from a single side. Type 1 thickness 4.8 mm, Type 2 thickness 3.8 mm. Load direction 1 is shown with grey arrows

3.1.1 TOEC/BW AEC measurements using contact ultrasonic measurements

As isotropic body has three independent third-order elastic constants, at least three independent measurements have to be performed. According to definition of acoustoelastic constants (Equation (2.33)), the direction of uniaxial load and bulk wave polarisation are two parameters of selection. In case of uniaxial loading of dog-bone shaped samples in a tensile machine (Figure 3.1), measurements of velocity variation of pressure wave and shear waves with two polarisations allows to determine acoustoelastic constants L_{21}, L_{22} and L_{23} (Figure 3.2a), and third-order elastic constants.

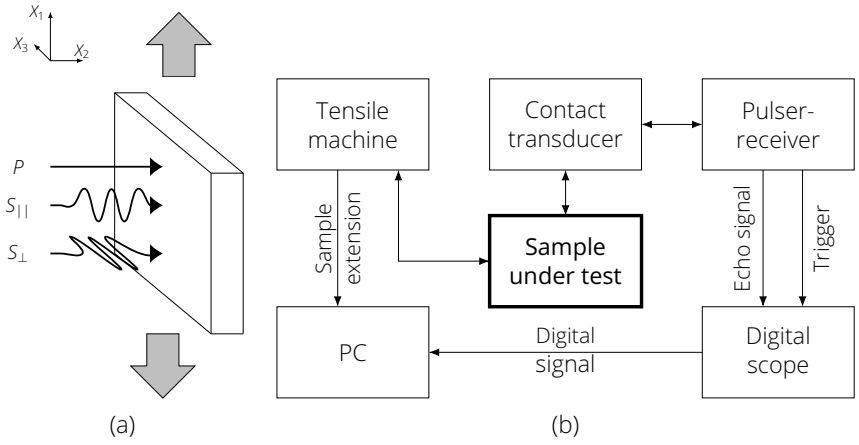


Figure 3.2: Polarisation convention and scheme of experiment for bulk wave AEC measurements. Load direction '1' is shown with the grey arrows. $L_{21} \leftrightarrow S_{||}$, $L_{22} \leftrightarrow P$, $L_{23} \leftrightarrow S_{\perp}$ (Equation (2.33))

In all measurements, a Zwick/Roell tensile machine was used to apply an external uniform tensile load to the specimens at eight different levels under ambient conditions. Actual elongation was measured with an extensometer (Zwick/Roell makroXtens II). Effects related to specimen heating were neglected. Deformations were automatically extracted using the

algorithm described in Section 3.4.1.

To measure BW AEC, ultrasonic pressure and shear wave transducers (Krautkramer K10K and MB4Y) attached normally to the sample surface were used to both generate the elastic wave and to record the multiple echo signal. The excitation pulse was generated using a pulser-receiver (Olympus 5900PR). The received signal was processed with the same pulser-receiver and recorded with a high-performance digital scope (LeCroy 62 Xi-A, 10 GS/s, 8 bit) in order to trace slight changes in the travel times. A schematic representation of the experimental setup is shown in Figure 3.2b. The raw measurement result for each polarisation for each load level was a multiple echo signal (Figures 3.12a and 3.14a).

Details of the group velocity extraction and BW AEC for known sample thickness, measured strain and flight time are given in 3.4.2.

3.1.2 RW AEC measurements using laser interferometry

For direct measurements of the RW AEC (defined in the Equation (2.36), [Gar20]), the the surface wave velocity propagation dependencies on applied load were recorded using LDV (Polytec OFV 353 + DD300). An Interferometer of this kind allows the non-contact measure of the 'out-of-plane' component of the Rayleigh displacement (or velocity) using the Doppler effect. The LDV head was mounted on a three-axis scanner, which allows changing the measurement point coordinate along the wave propagation direction. An ultrasonic transducer on a wedge was attached to the sample to excite the surface wave. The recorded wave propagation distance for the treated and untreated samples was in the range of 30-45 mm for different types of samples. The out-of-plane component of the displacement was scanned along five to eight parallel lines with a 1 mm step and a line offset of 0.5-1 mm. The wedge angle was chosen to generate a Rayleigh wave ($\theta_0 = \arcsin(\frac{C_{RW}}{C_{Wedge}_L})$, Equation (2.20)). Three commercial transducers with different nominal centre frequencies (1.5 MHz, 5 MHz and 10 MHz) were used for excitation. The waveform and frequency spectrum of the excited Rayleigh wave for each transducer are shown in figure 3.3.

For the $RW_{|||}$ propagation direction, Type 1 sample was used (Figure 3.1), and excitation and recording were done at the same face. For the $RW_{\perp}$ case, Type 2 sample was used, and a Rayleigh wave was generated on the backside and propagated around the half-circular edge into the scanning area. The resulting signal was recorded using an Analog-Digital Converter (ADC) board (GaGe 14200, 200 MS/s, 8 bit). The raw result of each scan was an out-of-plane shift, generated by Rayleigh wave propagation, at several scanning points (Figure 3.17, left-hand side).

The SNR of optical measurements is directly related to the fraction of reflected light reaching the detector. Therefore direct RW AEC measurements on a rough shot-peened surface treated surface require a scrupulous experiment (1000 averages were performed

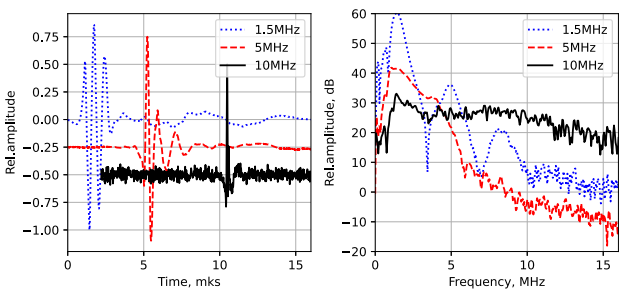
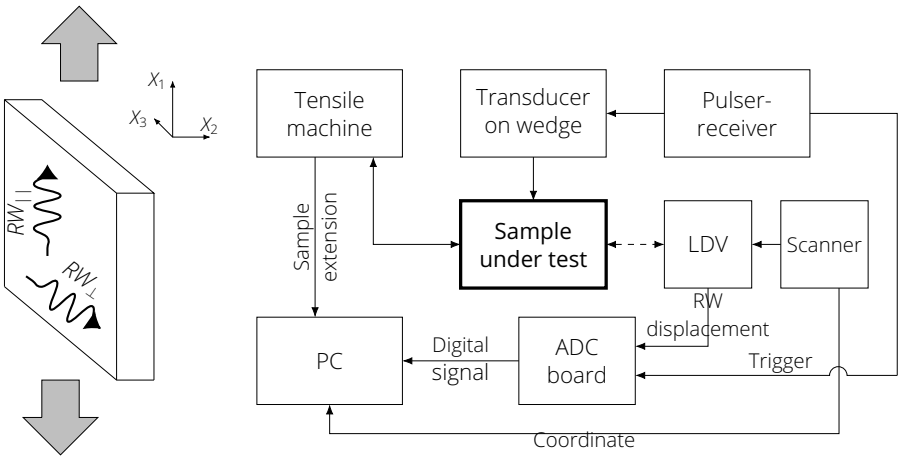


Figure 3.3: Example of commercial transducers temporal and frequency response.

for each scanning point on a dense grid) and robust data processing. Details of the data processing are given in 3.4.3.



(a) The direction of loading and propagation of the elastic wave.

(b) Experimental setup layout.

Figure 3.4: Notation and scheme of experiment for Rayleigh wave AEC measurements. Load direction '1' is shown with the grey arrows. $A^{(1)}_{R12} \leftrightarrow RW$, $A^{(3)}_{R12} \leftrightarrow RW_{\perp}$

3.2 Immersed measurements of RW dispersion using the ultrasonic goniometer HUGO

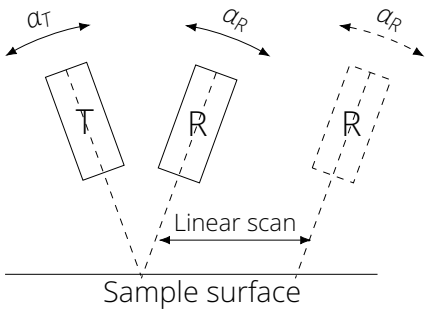
Rayleigh wave dispersion measurements on surface treated materials have been performed using the HUGO [Bar12]. This device was specially designed and developed at Fraunhofer IKTS for such measurements, and consists of two submerged transducers (transmitter and receiver) mounted on movable arcs, which allow the dip angles to be adjusted. One of the arcs is mounted on a platform which can be moved along the line. Therefore, two types of measurements are available:

1. recording of the reflected wave amplitude as a function of the angle between the transducers: the angle with the maximum energy loss associated with the energy transfer of the initial pulse into the surface acoustic wave can be found. Knowing the velocity of elastic waves in water, the RW velocity can be estimated accurately.

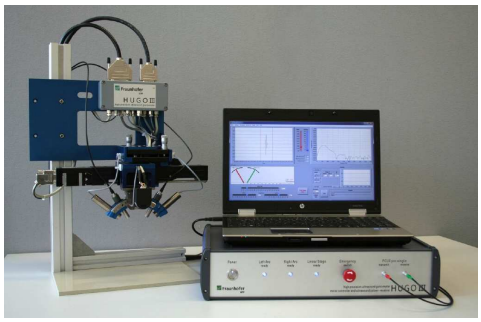
2. record of Rayleigh wave propagation with linear stage motion after finding the optimum angle for Rayleigh wave generation

The second approach was used to accurately estimate the Rayleigh wave velocity dispersion for 'Type 1' samples of Ti6246 and In718 at shot-peening intensities of 0A, 5A and 8A.

For all samples and treatment intensities, the surface acoustic wave propagation was recorded on a dense grid with small spatial step (0.025-0.05 mm) with 200 averages. A record example is shown in Figure 3.20. Details of processing are described in Section 3.4.4.



(a) Schematic representation of the available measurement modes



(b) Device exterior view (w/o immersion tank)

Figure 3.5: High-precision Ultrasonic Goniometer HUGO

3.3 Design of in-situ method of nonlinear elastic parameters estimation

Numerical simulation: selection of interaction modes

First, the most promising interaction modes in the relevant frequency range (1-10MHz) [1] were selected by comparing the calculated scattering efficiencies. The elastic constants used as model input are given in Table 3.1.

Assuming that the involved bulk waves were propagating at small angles with respect to the surface — that is, $\theta = \angle(\vec{k}_3, \overrightarrow{OZ}) \sim 95°$ for the bulk waves — the relative efficiencies for the allowed cases (Equations (2.41)–(2.42)) were calculated as shown in Figure 3.6. Due to the polarization restrictions, noncollinear interactions with horizontally polarized shear waves are forbidden.

The value of θ corresponds to near grazing propagation, and was chosen according to the experiment described in the following Section 3.3. Two Rayleigh waves were excited, and surface displacement was detected by laser vibrometry at the same surface. In this case, scattered bulk waves at small angles should be more visible than bulk waves, which radiate at steeper angles into the volume. Results of the calculations are shown in Table 4.3 and in the Appendix 8.6.

On the basis of these simulations, the following mixing cases were selected as being most efficient for subsequent detailed analysis:

1. RW + RW → P: two Rayleigh waves generating a bulk longitudinal wave at the sum of input frequencies; and

2. RW + RW → SV: two Rayleigh waves generating a bulk transversal wave with vertical polarization at the sum of input frequencies.

These cases have been also used for the experimental investigation of the detectability of the scattered component of two Rayleigh waves generating a bulk wave at near grazing angle.

In addition, for selected interactions (two Rayleigh waves generating the bulk wave), analysis of scattered wave amplitude at the surface on top of interaction volume (Section 2.7) has been performed. Results of these simulations have been validated by comparison with

[1] Here the approximate frequency range is defined by the Rayleigh wave penetration depth, chosen to be in the same order of magnitude as the surface treatment penetration depth of 300-800μm.

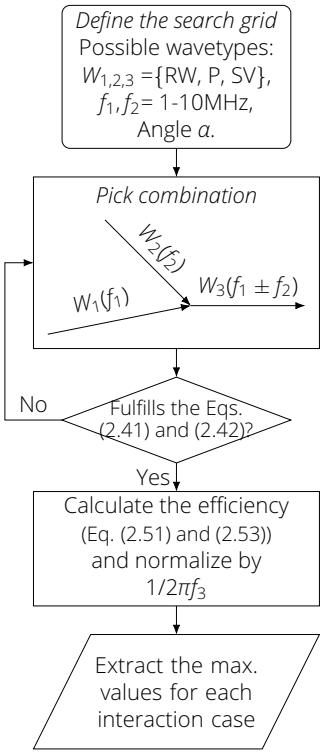


Figure 3.6: Efficiency calculation and selection of the most promising nonlinear wave interactions. Interactions including the shear wave with horizontal polarization are omitted due to polarization restrictions. Here α is the angle between $\vec{k_1}$ and $\vec{k_2}$ (Figure 2.5a).

Table 3.1: Material parameters of aluminum alloy (Al7075) used for simulations. Density and reference TOEC are taken from the literature [Moh19]; SOEC (Lamé constants) derived from velocity measurements.

Parameter	Symbol	Unit	Value
Density	ρ	[kg/m^3]	2750
Pressure wave velocity	V_p	[m/s]	6373
Shear wave velocity	V_s	[m/s]	3161
Rayleigh wave velocity	c	[m/s]	2925
Lamé's first constant	λ	[GPa]	56.74
Lamé's second constant	μ	[GPa]	27.48
First Murnaghan constant (reference value)	l	[GPa]	-250.0
Second Murnaghan constant (reference value)	m	[GPa]	-350.0
Third Murnaghan constant (reference value)	n	[GPa]	-350.0

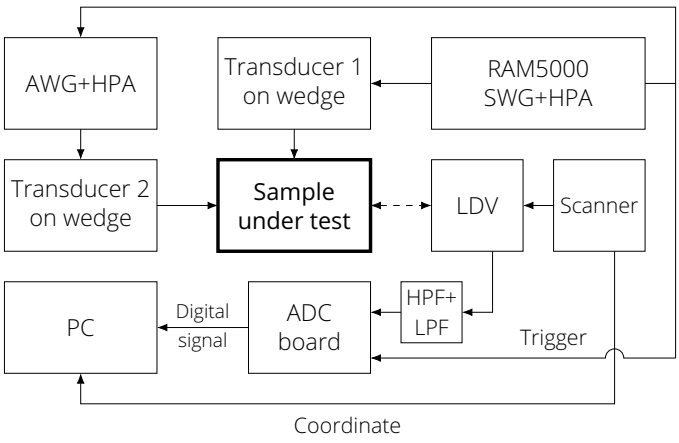
the FEM simulations, performed by Dr. Peng Zuo (IC London) as a part of collaborative work [Gar22].

Recording of the nonlinear interaction of RW using laser interferometry

The experiments followed two basic goals: investigating the feasibility of detecting the resonant interaction of two source waves (Rayleigh waves) in metal using commercially available equipment, and determining the variation in the local scattering efficiency H_L in the real sample, by changing the angle between sources for a fixed frequency ratio of the input waves.

A mirror polished aluminum alloy plate was used as a sample. Two commercial transducers with central frequencies of 1.5 and 3.5 MHz were mounted onto wedges, and optimized for Rayleigh wave excitation in aluminum. Glycerin was used as a coupling medium, in order to provide stable and long-lasting coupling. The electrical excitation of the transducers was realized by two independent signal generators and amplifiers to minimize the electrical crosstalk between sources. Generator frequencies (1.45 and 3.3 MHz) were chosen slightly off the nominal transducer central frequencies, accounting for amplifier and transducer frequency responses, and considering the optimal frequency ratio obtained from semi-analytical calculations (see Section 3.3). The angle between sources was swept from 45° to 180°, with a step size of 5°, using a special holder device (shown in Figure 3.7b).

The wavefield was captured with a laser Doppler vibrometer mounted onto a three-axis scanner. For each fixed angle between the two sources, the displacement component normal to the surface (out-of-plane component) was recorded in a square area of $10 \times 10\,\mathrm{mm}^2$, with a step size of 0.1 mm in both directions. The vibrometer signal was converted using an 8-bit ADC, averaged 600 times, and stored digitally. In order to increase the ADC resolution in the frequency band of interest (i.e., around the frequency of the scattered wave), an analog High-Pass Filter (HPF) was added to suppress the fundamental components. The schematic representation of the setup is shown in Figure 3.7. The amplitudes of the displacement along the vertical axis X_3 for the fundamental components were in the range of 15–25 nm. The amplitude of the scattered component was in the range of 0.5–20 pm, which is at least ten times larger than the resolution limit of the vibrometer.



(a) Here: SWG - sine waveform generator, AWG - arbitrary waveform generator, HPA - high-power amplifier, HPF+LPF - high-pass (4MHz) and low-pass (11MHz) filter.



(b) Top-view of scan area

Figure 3.7: Wave mixing experiment: scheme and photo of scan area

Additional measurements have been carried out to validate the resolution capacity of the experimental setup for detecting the nonlinear interaction of surface waves and to verify that the signal at the sum frequency of two initial waves is not generated by instrumentation. The optical path of the vibrometer was changed from the normal reflection from

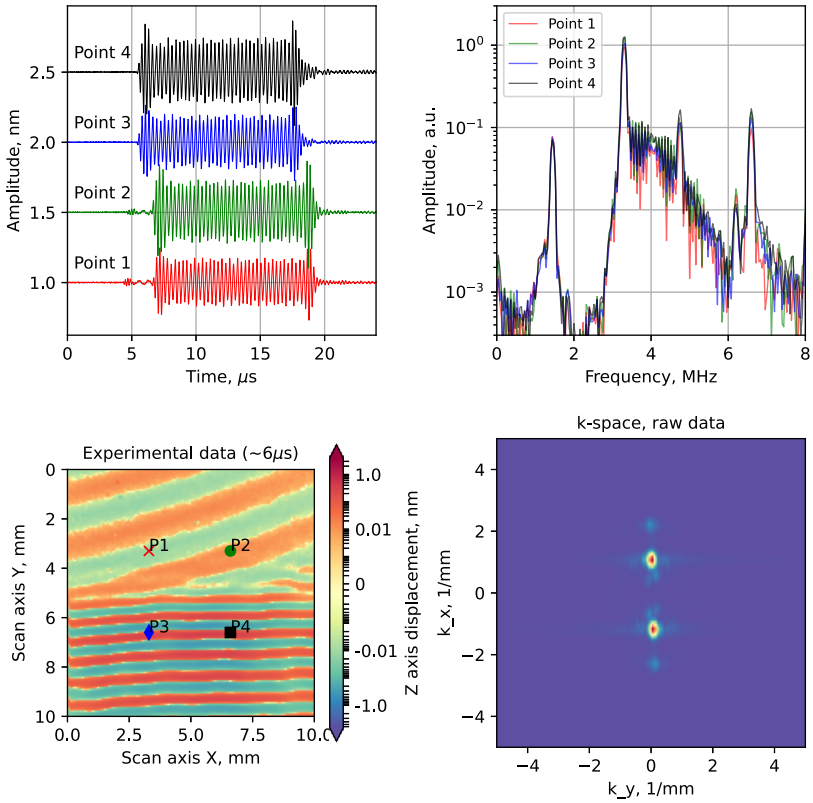


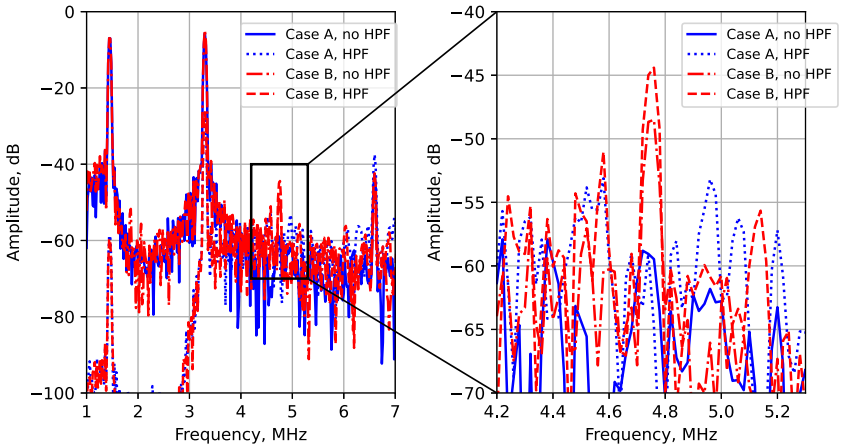
Figure 3.8: Example of raw scan data (angle between the source waves $\alpha \approx 165°$). Four temporal responses at different scan points and corresponding frequency responses are shown on top left and top right subfigure, correspondingly. Snapshot of the wavefield at the moment of two wavefronts arriving into the scan area (6 μs) is given on bottom left subplot (here the log. colormap is used to highlight the 1.45 MHz component, suppressed by HPF). Two-dimensional spatial Fourier transfrorm is shown on the bottom right subplot.

a single polished metal surface to the double reflection from two almost parallel polished surfaces (Figure 3.9b).

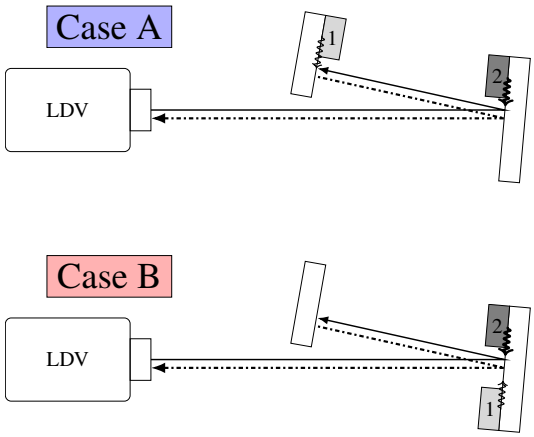
Double reflection allows the contribution of wave mixing to be isolated from the imperfections of the data acquisition setup (Figure 3.7), as the digital signal will contain equal instrumental error, generated by the high-amplitude fundamental components in the acquisition chain. To achieve that, after rearranging the setup from Case A (isolated sources) to Case B (wave mixing) the amplitude of the wave, generated by rearranged transducer 1 was changed accordingly by reducing the high power amplifier gain. All other data acquisition parameters remained unchanged.

The measurement results are given in Figure 3.9, and show a clear response at the mixing frequency (4.75 MHz) in presence of elastic wave interaction (Case B), at least 10 dB above the instrumental noise (Case A), which itself contains no distinct instrumental-induced (LDV, filters, ADC) component at the interaction frequency.

In order to simplify the analysis of acquired experimental data, as well as to test and validate the processing algorithms, described below, an interactive MATLAB graphical interface have been developed (Figure 3.10).

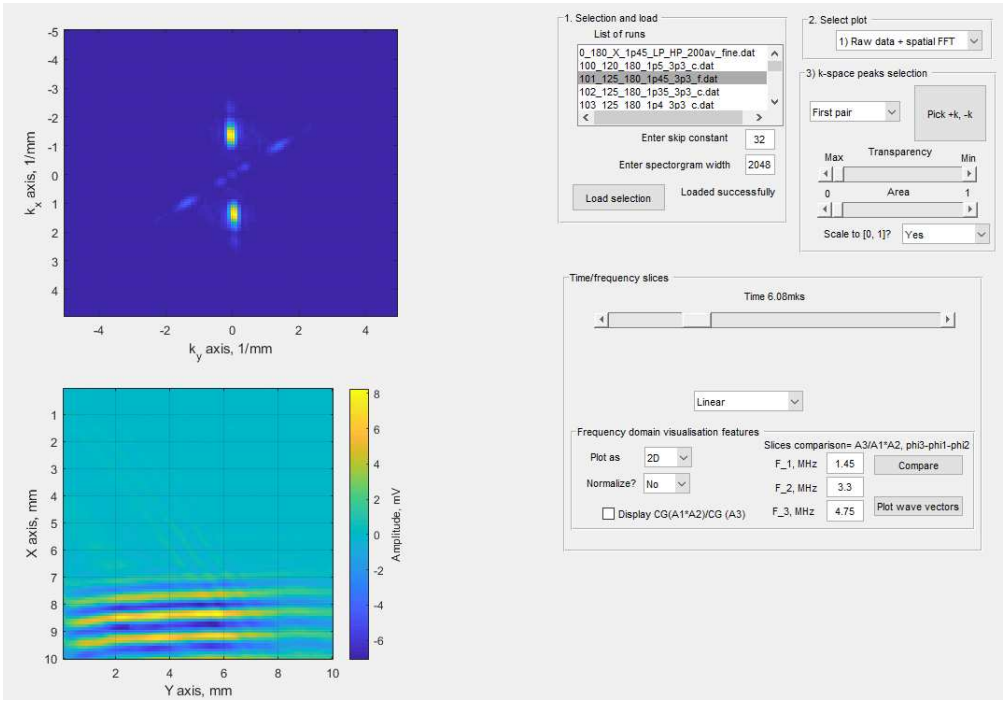


(a) Frequency responses for isolated sources (Case A) and in presence of elastic wave interaction (Case B).

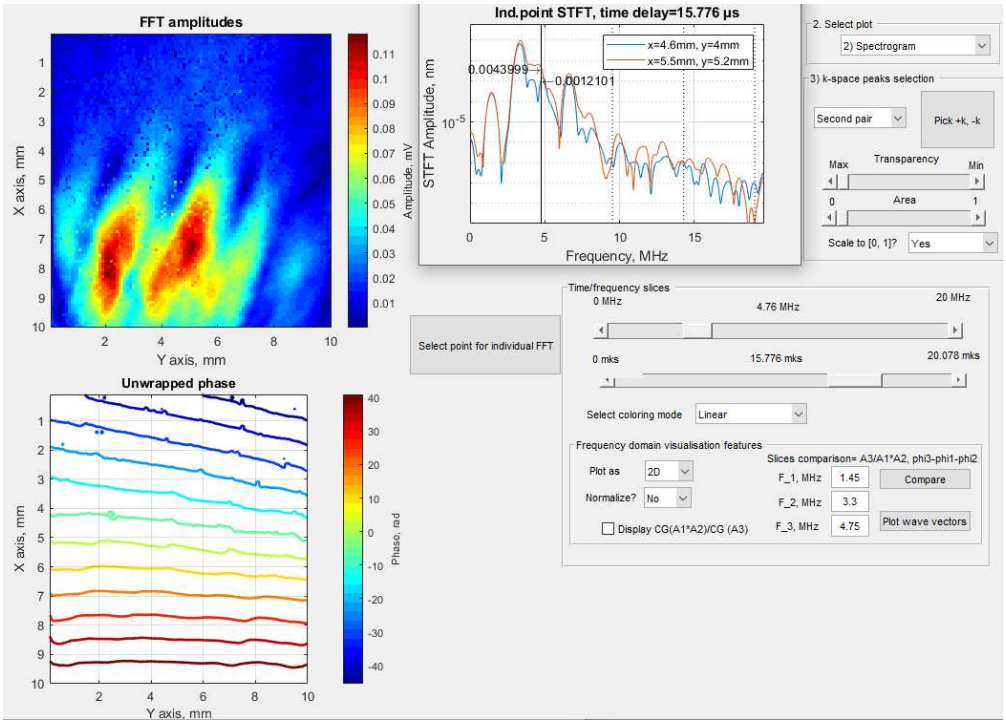


(b) Scheme and optical path of two cases, used for auxiliary measurements.

Figure 3.9: Measurement results and principal scheme of additional comparative study: two transducers mounted at the different polished metal plates (Case A); and two transducers mounted at the same polished metal plate (Case B) with identical optical path. The light beam is focused on the left plate. Transducer 1 (1.45 MHz wave) and transducer 2 (3.3 MHz wave) are depicted with grey rectangles on the scheme.



(a) Selection of run and raw data visualisation in time domain: snapshot and two-dimensional spatial Fourier transform.



(b) Visualisation in frequency domain. Selected points frequency responses and Short-Time Fourier Transform (STFT) slices: amplitudes and unwrapped phase plane for selected frequency and time delay step.

Figure 3.10: Interactive MATLAB graphical interface for analysis and advanced visualisation of experimental LDV data.

3.4 Algorithms

The vast amount of experimental and simulation data had to be evaluated accurately; therefore several algorithms and scripts were developed and validated both with generic and real test data. In this section a brief description of each developed tool is given.

3.4.1 Automated strain extraction from raw extension data

In total more than 40 tensile tests has been performed (BW: 2 materials x 3 wave polarisations x 5 measurement points, RW: 2 materials x 2 sample types X 4 treatment states). The demanded loading profile was determined before the measurement in a Zwick/Roell control software, and the actual extension has been measured with the extensometer and extracted as (time from measurement start, absolute elongation) array. Actual strain data for each loading step have been calculated by division of extension for given step over the extensometer base.

Raw record of extensometer, along with the extracted data levels is shown at the Figure 3.11. Before the actual measurements, pre-loading (five slow zero load- full load cycles for homogenizing the grain orientation and check of sample clamping quality), have been performed.

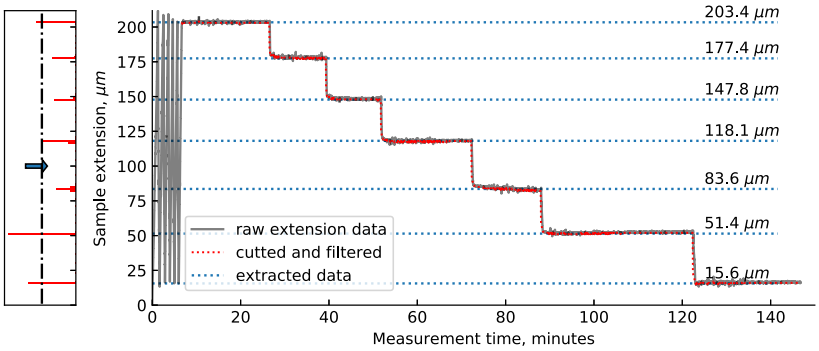


Figure 3.11: Extraction of actual sample extensions during the tensile machine testing

Number of loading steps (n_{steps}), pre-loading and actual measurement discretisation steps were the input parameters for the loading profile and record of extension. Therefore, the actual extensions have been extracted as followed.

1. Cut out the pre-loading part, leaving only the main part of the measurement (stepped profile).
2. Apply the moving average filter to extension data (average over 5 sampling points) and round to one decimal.
3. Compute the histogram values H_V (number of occurrences) and bin centres H_{BC} for a pre-defined histogram parameters (number of bins or bin width).
4. Define the initial *threshold* level: h=max(H_V)/2 and empty *extracted peaks* array E_P. Perform a descent until the number of extracted peaks will reach the number of loading steps. Initial threshold level and descent direction are shown at histogram on the left-hand side of Figure 3.11 with dash-dotted line and arrow, correspondingly.
   While *size*(E_P) < n_{steps} AND h > 2:
   a) E_P=H_{BC}(H_V > h)
   b) h=h-1

3.4.2 Comparison of the group velocity evaluation methods for the BW AEC measurements

The principal issue in determination of Time Of Flight (TOF) of ultrasonic wave is the absence of standard definition of TOF/velocity for pulse-echo measurements. According to ISO 5577 (6.1.22-6.1.26), several modes are equivalent:

1. *flank-to-flank*: measurement of the time difference between similar edges (flanks) of multiple echoes, usually defined as rising (leading) or falling (trailing) edge, at a specified amplitude

2. *peak-to-peak*: measurement of the time difference between the maximum amplitudes of multiple echoes

3. *zero crossing*: measurement of the time difference between corresponding zero crossings of multiple echoes

Comparison of elastic wave velocities, based on these definition, have been done; in addition, two other methods, typical for DSP applications, have been added:

4. *autocorrelation*: measurement of the time difference between the maximum values of the autocorrelation function of multiple echoes signal x:

$$\widehat{R}_{xx}(m) = \begin{cases} \sum_{n=0}^{N-m-1} x_{n+m} x_n^*, m \geqslant 0, \\ \widehat{R}_{xx}(-m), m < 0, \end{cases} \tag{3.1}$$

5. *cross-correlation*: measurement of the time difference between the maximum values of cross-correlation function between the windowed first echo y and multiple echoes signal x:

$$\widehat{R}_{xy}(m) = \begin{cases} \sum_{n=0}^{N-m-1} x_{n+m} y_n^*, m \geqslant 0, \\ \widehat{R}_{yx}(-m), m < 0, \end{cases} \tag{3.2}$$

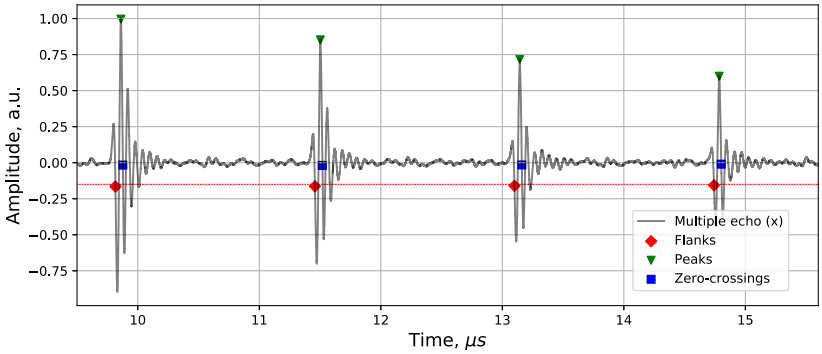
Here x_n and y_n are the discrete signal amplitudes at the n-th sampling point. The asterisk denotes the complex conjugation operation in the general case (in this case all amplitudes are real).

Figures 3.12 and 3.14 show examples of multiple echo signals of pressure and shear wave recordings. These figures also show points extracted according to the definitions described above. Variations in TOF, extracted from records, presented in Figures 3.12 and 3.14, are shown in Figure 3.15. First echoes are used as a reference point, extracted peaks used as a baseline.

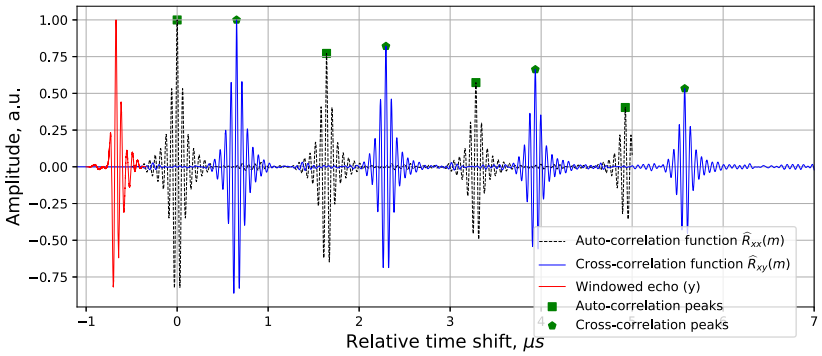
The total number of measurements exceeded 250 records (2 material types x 5 measuring points per sample x 3-5 records per measuring point x 8(9) load levels). This dataset allowed comparing the robustness of the implemented algorithms for each type of interaction wave.

The relative TOF ($TOF_i/\overline{TOF}$) extraction error for the whole dataset for each method is given in Fig. 3.16 (a detailed description of the comparison metric is given in the figure caption).

Another DSP approaches, such as cepstrum liftering and envelope peak extraction using Hilbert transform [Opp09], have shown both inferior performance and worse computational efficiency.



(a) Multiple echo signal and different TOF definitions



(b) TOF extraction with auto-correlation and cross-correlation functions

Figure 3.12: Processing example for *P*-wave in In718

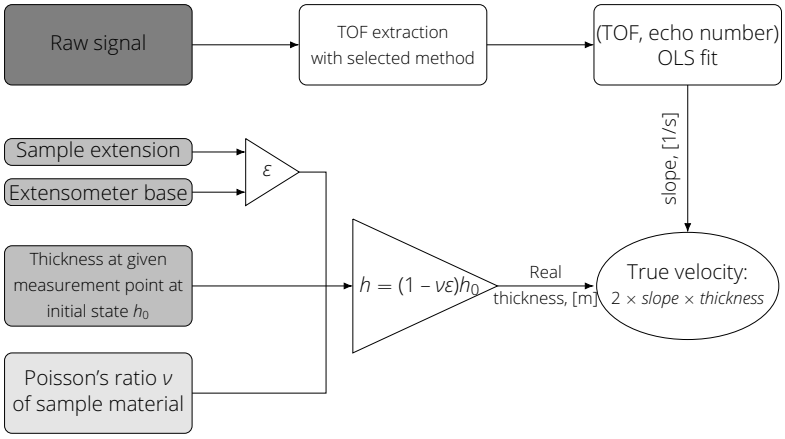
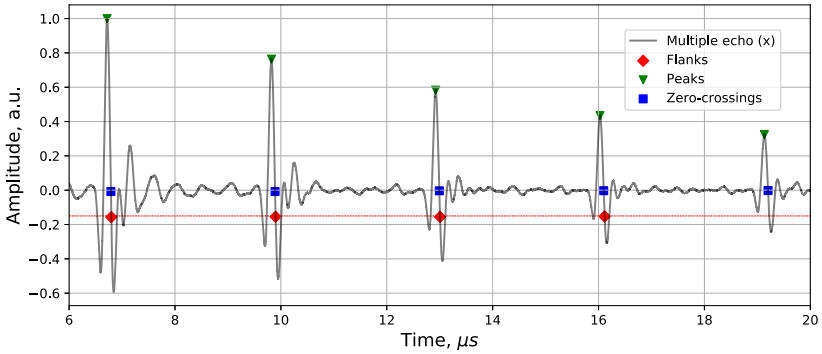
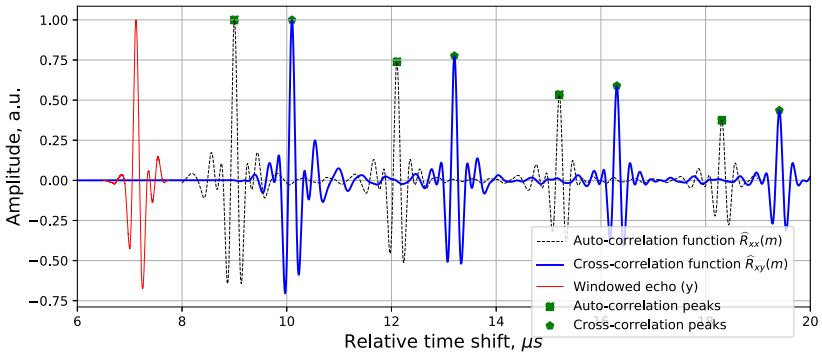


Figure 3.13: Velocity calculation: dataflow. Here Ordinary Least Squares fit (OLS) is used for slope estimation.

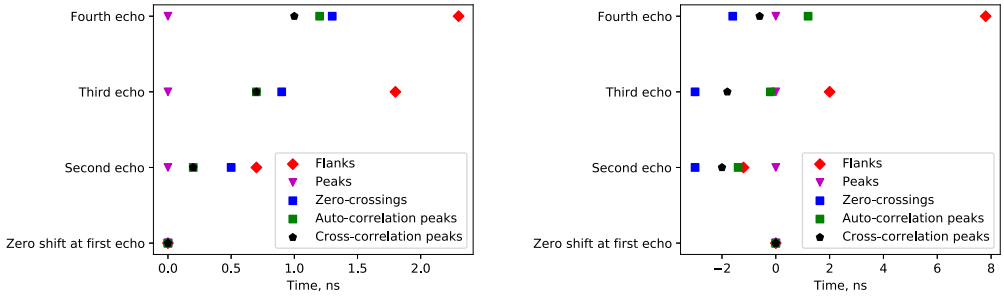


(a) Multiple echo signal and different TOF definitions



(b) TOF extraction with auto-correlation and cross-correlation functions

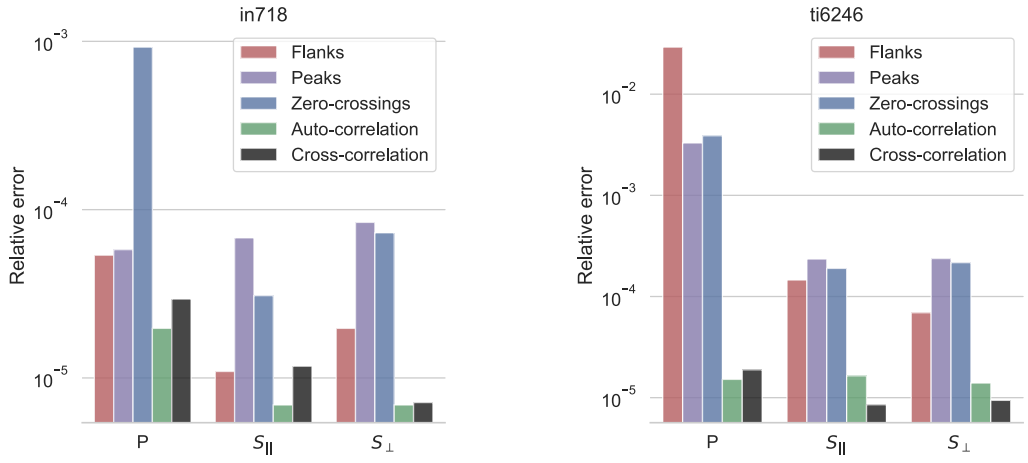
Figure 3.14: Processing example for $S_{||}$ wave (polarisation convention given in Figure 3.2a) in In718.



(a) P-wave

(b) $S_{||}$

Figure 3.15: TOF variations, extracted from data shown in Figures 3.12 and 3.14. All detected time delays are shifted to the same reference point, peak method is used as a baseline.



(a) In718

(b) Ti6246

Figure 3.16: Comparison of the relative error of the algorithms used to estimate TOF. *Relative error* on the vertical axis is the standard deviation of the relative TOF calculated for all measurement points and load levels. Smaller values correspond to more robust TOF extraction algorithms. Dividing by the average TOF value for each measurement point and load level eliminates the effects of local variations in thickness and changes in TOF due to acoustoelastic effect.

3.4.3 Group velocity evaluation using the iterative algorithm for the low SNR data

An additional procedure for the velocity extraction was needed due to the rather low Signal-to-Noise Ratio (SNR) of the LDV measurements, especially for the treated samples at higher frequencies. Each scan line have been treated independently as a line scan, and processed as following:

1. Selection of the point with the highest SNR (reference scan point).
2. Calculation of cross-correlation function between the reference point and given point at the scan line.
3. Extraction of the cross-correlation function maximum time delay (between the reference point and given point).
4. Estimation of RW velocity by the linear approximation in the (scanner coordinate - cross-correlation peak delay) space with an RANdom SAmple Consensus (RANSAC) iterative algorithm [Cho09].

RANSAC, or the random sampling and consensus algorithm, is an iterative algorithm for estimating model parameters in the presence of *outliers*. In this case, outliers were defined as points with the SNR below the threshold level, or secondary peaks extracted from the cross-correlation function. In general, RANSAC consists of two steps, iterated until the required level of accuracy is reached:

1. Select the random minimal sample set (*2 points for the line fit*) from the input dataset (*line scan*), fit the model
2. Add the points to the sample set, which are consistent with the model with a predefined error

The procedure is stopped if the fit quality target value or the maximum number of iterations is reached. The threshold and fit quality parameters have been selected manually. Example of the line scan processing with the RANSAC algorithm is shown in Figure 3.17.

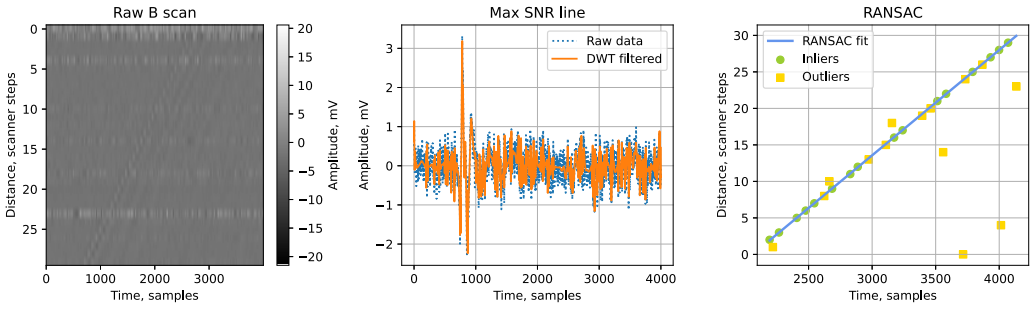


Figure 3.17: Example of direct LDV scan processing. Left sub-figure - raw scan, middle subfigure - raw record at the given point and result of filtering, right subfigure - result of iterative fitting.

An example of the data processing for the A_{R12} evaluation is shown in Figure 3.18. The A_{R12} coefficients are evaluated with the Ordinary Least Squares fit (OLS) (see Appendix 8.5).

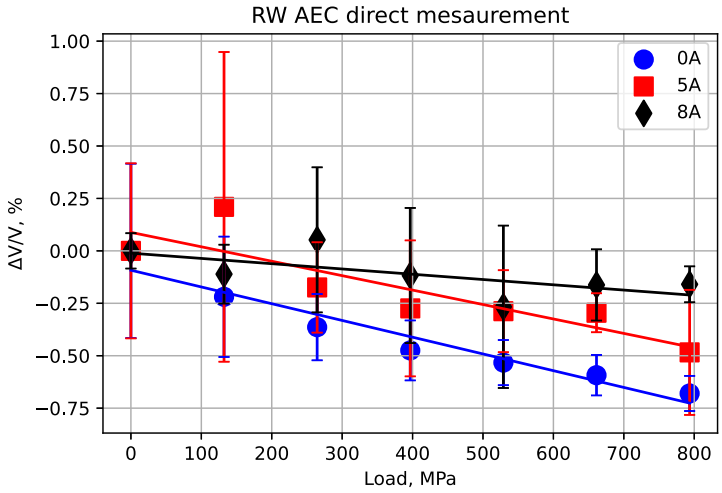


Figure 3.18: Example of A^3_{R12} measurements for In718 at f_c=5MHz.

3.4.4 Phase velocity extraction

The OLS fit (described in Appendix 8.5) or RANSAC line fit (described in Section 3.4.3) for peaks extracted in the time domain can estimate the group velocity of an elastic wave for the frequency band defined by the ultrasound transducer (Figure 3.3). As mentioned above, the Rayleigh wave velocity is dispersive in the surface treated and therefore inhomogeneously stressed layer. Thus, the extraction of phase velocity $v_p = \omega/k$ and its dependence on Rayleigh wave frequency provides additional information about the velocity variation at different penetration depths.

Having linear scan records of the displacement $U(x,t)$ along the wave propagation direction, by performing 1D Fast Fourier Transform (FFT) one can obtain the growth of the wrapped phase at each frequency of interest:

$$U(x,\omega) = FFT(U(x,t)), \tag{3.3}$$

$$\varphi(x,\omega) = atan2(\Im U(x,\omega), \Re U(x,\omega)), \tag{3.4}$$

where the function *atan*2 returns the wrapped phase φ in range $[-\pi,\pi)$ (Figure 3.19). By

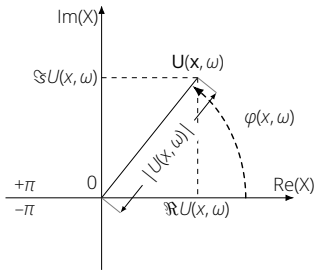


Figure 3.19: Wrapped phase φ, defined in range $[-\pi,\pi)$

phase unwrapping, or substituting $\pm 2\pi$ to eliminate phase jumps, and therefore reconstructing the *unwrapped phase* Γ dependence on the propagation distance, followed by a fitting in the (coordinate, unwrapped phase) domain, the phase velocity for each frequency component can be obtained. As in the previous cases, the RANSAC algorithm was

used to make the phase velocity extraction procedure more robust to measurement noise. Depending on the origin of the data, the following procedures were implemented.

Immersed measurements: HUGO scan

The high SNR of immersed ultrasonic measurements allows the phase velocity variation to be extracted over a wide frequency range from a single scan with a broadband excitation pulse signal. In this case the central frequency and bandwidth of the transmitting and receiving transducer limit the operating frequency range. In order to extend it, two series of measurements were carried out with a low (4 MHz, equal to transmitter) and high (10 MHz) central frequency of the receiving transducer. These measurements were combined using the procedure described below. An example of an immersed linear scan measurement and its attenuation is shown in Figure 3.20.

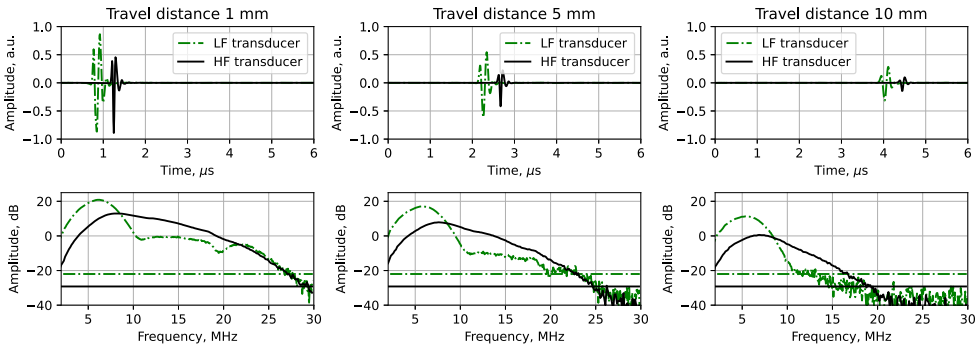


Figure 3.20: HUGO linear scan for RW dispersion measurements and wave attenuation for nontreated surface. Here: LF - low frequency receiving transducer (same as transmitter), HF - wideband high-frequency receiving transducer.

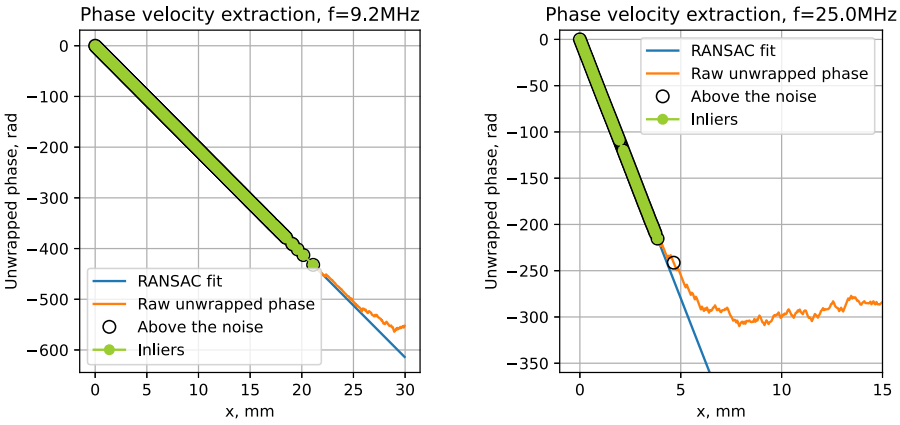


Figure 3.21: Example of RANSAC-based phase velocity extraction from the HUGO linear scan data. Here the points above the noise threshhold (+12dB) are highlighted with black.

First, the operating bandwidth for each case was determined, with the threshold defined as shown in 3.23. This method was chosen on the basis that ADC sampling rate (100MS/s) was significantly higher than the actual operating bandwidth (0-10MHz for the

low-frequency (LF) transducer and 4-25MHz for the high-frequency (HF) transducer) and the rapid attenuation of high-frequency components. The phase velocity for each (distance-time delay) displacement scan and data fusion were done according to an algorithm:

1. Perform an 1D FFT for each record: U(x, t) → U(x, ω)
2. Evaluate the noise threshold as shown in Figure 3.23 (upper row). For each frequency line ω_i:
   a) Shift the phase to zero by dividing by U(0 ,ω_i) at the scan starting point and unwrap the phase
   b) Select the points with FFT amplitude higher, than the threshold level and apply the iterative RANSAC line fit method in (travel distance, unwrapped phase) space (Figure 3.21).
   c) Calculate the phase velocity:

$$V_p = 2\pi f \left(\frac{x}{\varphi}\right), \tag{3.5}$$

   where the last part is the slope of the line, fitted in the previous step.
3. Merge the LF and HF data with procedure described in Figure 3.23: use the LF transducer data for low-frequency area, data from both transducers in mid-frequency range and the HF transducer data in high frequency range.

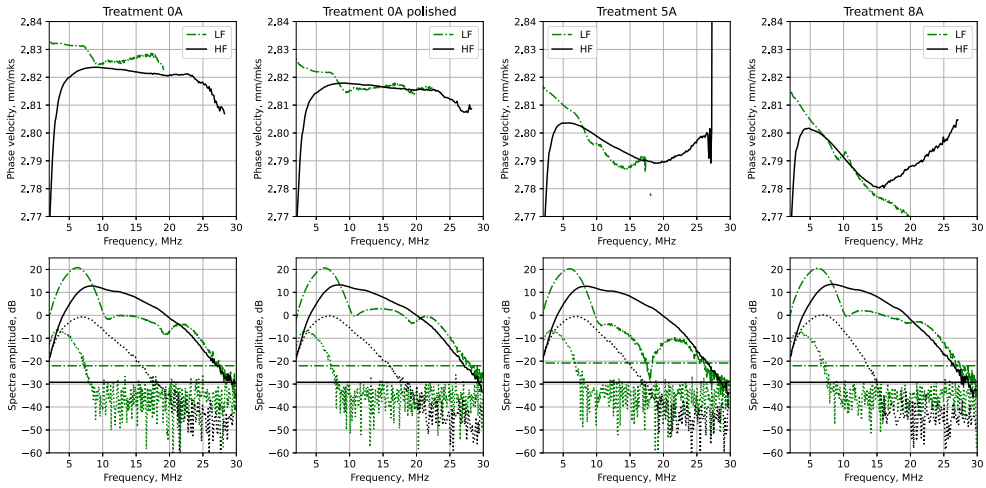


Figure 3.22: Rayleigh wave dispersion for surface-treated In718: raw data from two transducers. The curves on the bottom row show the FFT amplitudes at the beginning and end of the scan line. The merging result is shown in Figure 4.4.

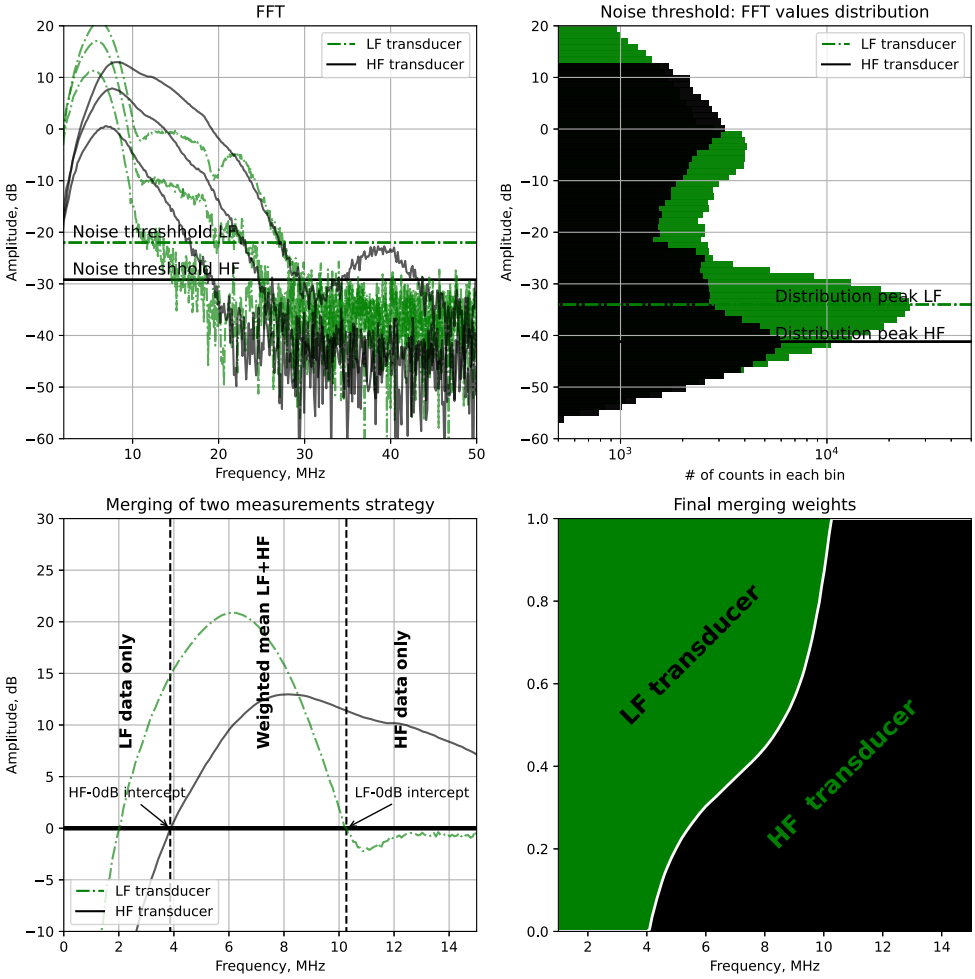


Figure 3.23: Automated determination of the noise threshold for immersion measurements (HUGO) and seamless merging of dispersion data measured by low-frequency (LF) and high-frequency (HF) sensors. In the upper left Figure, the same data as in Figure 3.20, (1 mm, 5 mm and 10 mm scanning points propagation paths) is given. Upper subfigures shows the definition of the noise threshold (1D FFT distribution peak + 12dB or SNR +12dB, or signal is at least 4 times stronger than noise). The bottom subplots show the definition of weights for merging the dispersion curves. The 0 dB threshold is manually selected as the linear response limit for the LF transducer for a given amplifier factor.

3.4.5 Multidimensional phase unwrapping and wave vectors/phase velocity extraction

Basic idea

Typical 2D LDV scan data consists of a scalar or vector displacement field U recorded in surface (x,y) coordinates and time t. This dataset can be processed in several ways:

- by performing a 3D FFT $U(x,y,t) \rightarrow U(k_x,k_y,f)$ one can extract the dominant wave vectors and analyse the energy density distribution in space k-f (wave number - frequency).
- by performing spatial FFT $U(x,y,t) \rightarrow U(k_x,k_y,t)$ the arrival time of the wave packet to the reflecting obstacle can be automatically extracted from the change of direction of wave vectors. Certain components of the wave packet can be selected and filtered/selected in the spatial domain using a generated mask (e.g. binary) in k-space and inverse FFT.

For the wave mixing experiment using LDV , another method, namely 2D phase unwrapping, has been developed which has proven to be robust and applicable to specific problems. The need for a new tool was driven by the presence of two or more wave packets in the scan area, as well as additional parasitic broadband components from amplifier harmonics and gate opening which make an analysis by conventional methods inconvenient.

The essence of the method is to apply 2D phase unwrapping algorithms to Short-Time Fourier Transform (STFT) slices: $U(x,y,t) \rightarrow U(x,y,f,\tilde{t})$. STFT slicing is shown in Figure 3.24. Correctly reconstructed phase contains information about the distribution of wave vectors and phase velocities over the scan area for the frequencies of interest. Thus local spatial variations in direction and/or velocity of the wave propagation can be taken into account. This can be useful for visualizing wave vector fields and for proving the phase resonance condition (2.41) on given part of the scanning field.

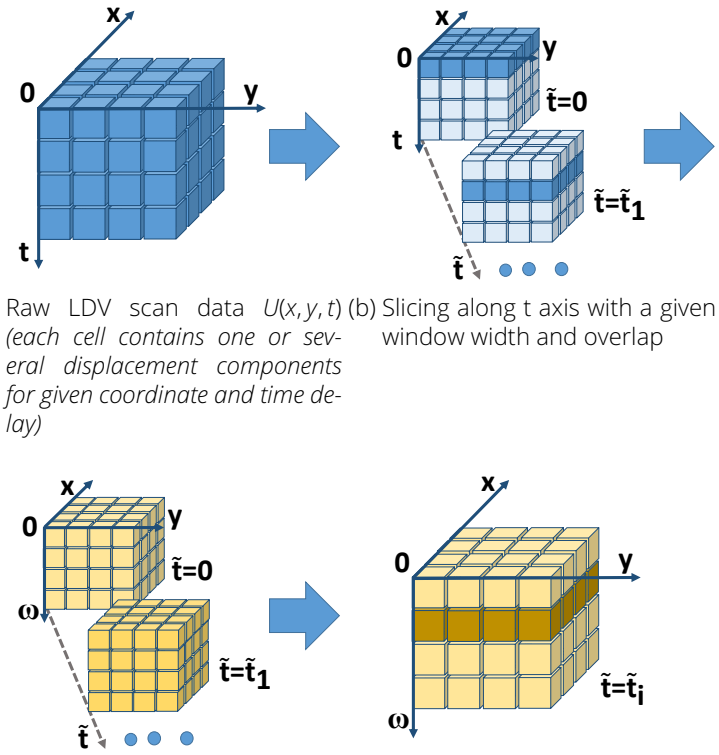
Comparison and selection of 2D phase unwrapping algorithm

Phase unwrapping (reconstruction of "true" phase Γ by adding $2\pi n$, $n \subset \mathbb{Z}$, to the wrapped phase values $\varphi, \varphi \subset [-\pi,\pi]$) is a complex inverse numerical problem with no unique solution [Str99; Ghi94; Her02; Zha18]. Several 2D phase unwrapping implementations available in the MATLAB File Exchange community have been compared using the generated synthetic data. Below is a list of the algorithms used for comparison:

1. unweighted least squares method [Ghi94] (implemented by M. F. Kasim)
2. transfer of the intensity equation [Zha18] (implemented by the authors, Z. Zhao et al.)
3. sorting by reliability following a noncontinuous path (2D-SRNCP) [Her02] (implemented by M. F. Kasim/implemented by M. Mullen)
4. branch cut phase unwrapping (2D Goldstein) [Gol88], (implemented by B. Spottiswoode)

The main difference between these 2D algorithms is the definition of the penalty function and the padding strategy. In addition, a superposition of MATLAB built-in 1D phase unwrapping procedures was added for comparison.

These algorithms were compared with synthetic data simulating the wavefield of a small source with a given wavelength for the range of dimensionless parameters specified in the



(a) Raw LDV scan data $U(x, y, t)$ *(each cell contains one or several displacement components for given coordinate and time delay)*

(b) Slicing along t axis with a given window width and overlap

(c) FFT of selected data block

(d) Slicing in $(\tilde{t}, \omega)$ domain for the phase unwrapping

Figure 3.24: Short-time Fourier transform (STFT) and slicing for the phase unwrapping

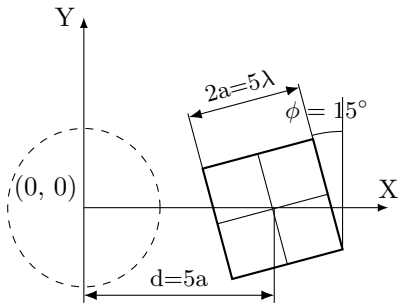


Figure 3.25: Coordinate convention for 2D phase unwrapping algorithm selection with synthetic source at point (0, 0) with wavelength λ. Varied parameters: side of square scan area $2a$ (4λ, 8λ and 16λ), distance to source d ($2.5a$ $5a$, $10a$), rotation angle φ (0° – 45°) and SNR (40dB, 20dB, 12dB and 6dB). The square scan area (100x100 scan steps) is shown with a thick line.

caption of Figure 3.25. For a fixed wavelength λ the size of the scan area (2a*2a for 100 scan steps in each direction), the distance from the centre of the scan area to the source d and the angle between the scan axes and the direction between the wave source and scan centre. This parametrization allows comparing the robustness of the algorithms to different wavefront curvatures and relatively low number of scanning points per wavelength. The robustness of the algorithms to low SNR was compared with the addition of random noise. An example of the synthesised wrapped data is shown in Figure 3.26. This figure shows

the wrapped phase at the synthetic wave frequency in colour (the FFT slicing is explained in Figure 3.24).

Figures 3.27 and 3.28 show a comparison of the robustness of the algorithms to the above parameters. In analogy with the definition of the elastic net penalizing function [Has09], the *phase reconstruction error R* is defined here as the product of the mean absolute difference D_1 and the mean standard deviation D_2 between the "true" $\Gamma(x,y)$ and the "reconstructed" $\widetilde{\Gamma(x,y)}$ 2D phase planes:

$$D_1 = \overline{|\Gamma - \overline{\Gamma} - (\widetilde{\Gamma} - \overline{\widetilde{\Gamma}})|}, \tag{3.6}$$

$$D_2 = \sqrt{\overline{(\Gamma - \overline{\Gamma} - (\widetilde{\Gamma} - \overline{\widetilde{\Gamma}}))^2}}, \tag{3.7}$$

$$R = \log_{10}(D_1 D_2), \tag{3.8}$$

where overline means averaging in the (x,y) plane. The *gradient reconstruction error* is defined similarly for k_x and k_y.

The phase and gradient reconstruction results (Figures 3.27 and 3.28) give an indication of the limitations of the 2D phase reconstruction algorithms. As expected, SNR is the most important parameter for stability and quality of the phase reconstruction: at SNR 20 dB and higher all algorithms show comparable results. The number of scan points per wavelength is the second most important parameter. In case of low SNR, the wavefront shape and orientation as well as the number of scanning points per wavelength can also influence the quality of the reconstruction.

The algorithm [Zha18] showed the best stability and quality of phase reconstruction. However, it has the drawback of manually selecting the starting point, which limits its application to large datasets.

In addition to the comparison of reconstruction errors, two problem-specific heuristic criteria were added for the final choice of algorithm:

1. Adequate reconstruction (similar amplitudes and directions) of wave vectors/phase velocities for the experimental data.

2. Stability at wavefront boundaries and edges (experimental data).

For the present case (high SNR$\sim$ 40dB and additional analog filtering in the design of the experiment), the 2D-SRNCP algorithm [Ghi94] was used as both computationally efficient and robust.

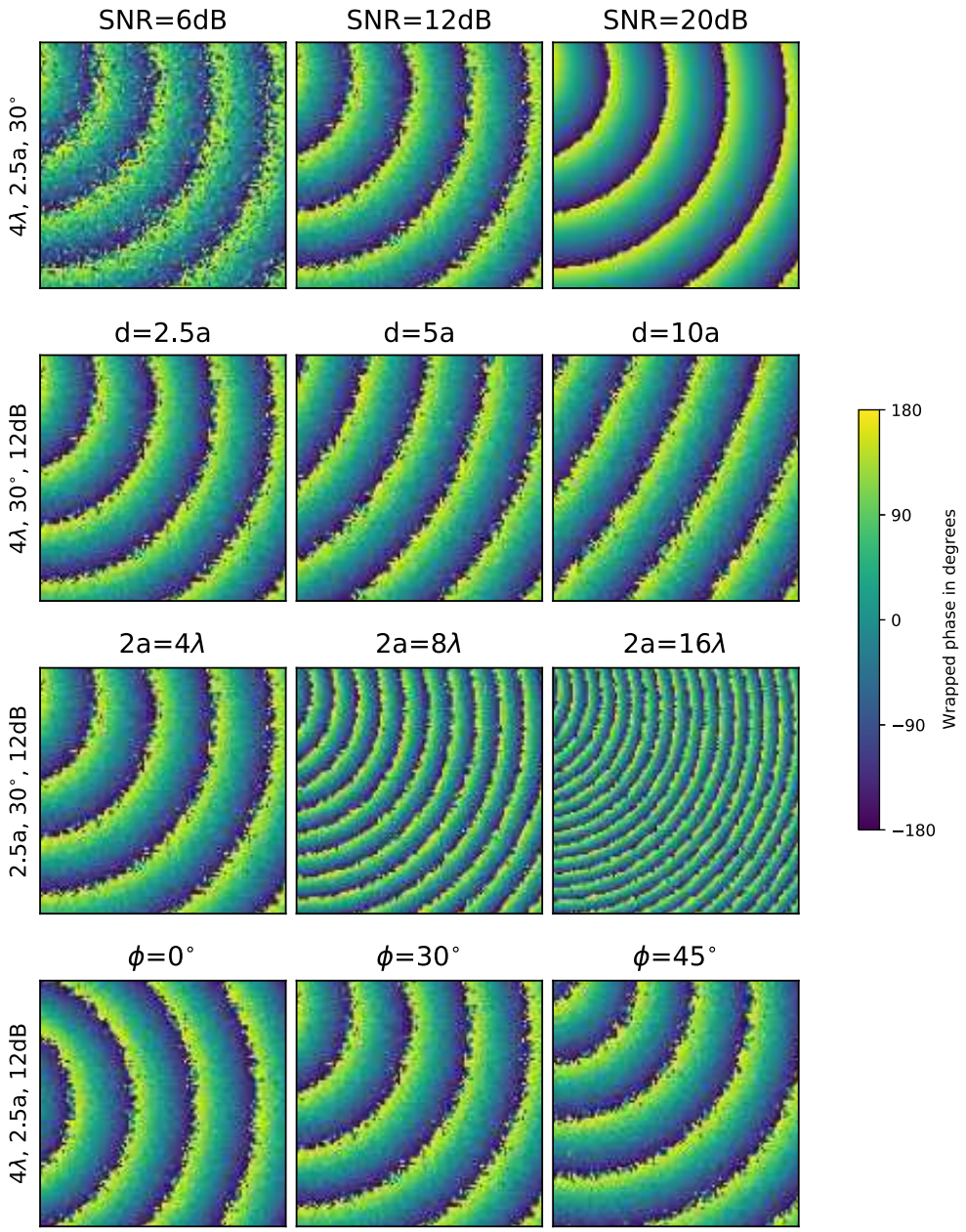


Figure 3.26: Example of synthesized wrapped phase fields for various parametrisation coefficients. Fixed parameters for each row are given on left side.

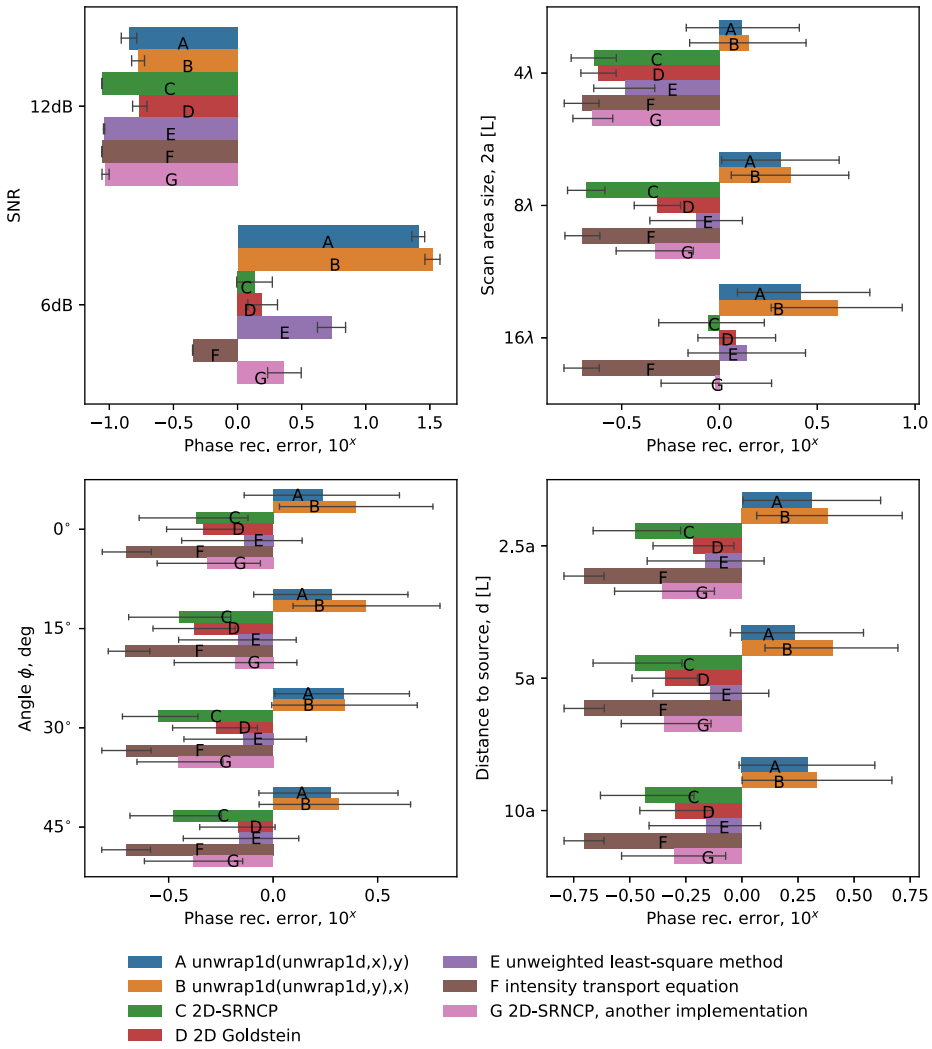


Figure 3.27: Dependency of the *phase reconstruction errors* of several 2D phase unwrapping algorithms on different scan parameters. For higher SNRs than 12dB all 2D algorithms behave similarly. Errorbars show the standard deviation over all varied parameters, except varied at the subplot vertical axis.

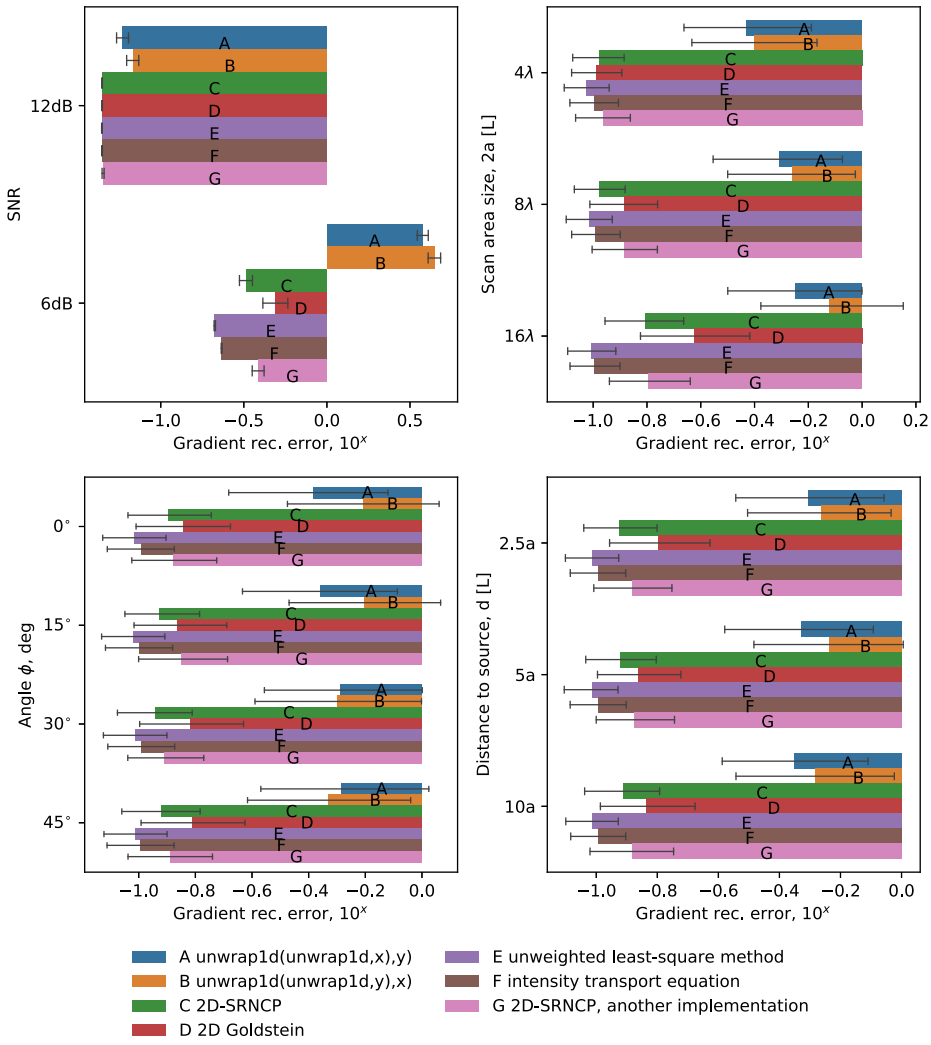


Figure 3.28: Dependency of the *gradient reconstruction errors* of several 2D phase unwrapping algorithms on different scan parameters. Smaller values shows the higher similarity of true and reconstructed gradient fields.

Wave vector and phase velocity extraction algorithm

With a 3D array of complex numbers, one may reconstruct the 2D phase planes for the frequency of interest by applying a certain 2D phase unwrapping algorithm to a given slice. From the phase values Γ obtained in this way, one may easily extract the wave vectors and phase velocities by taking the gradient of the 2D unwrapped phase:

$$\vec{k}_{\omega}(x,y) = -\overrightarrow{\nabla}\Gamma_{\omega,\tilde{t}_i}(x,y) \tag{3.9}$$

$$V = \frac{\omega}{|\vec{k}|}, \tag{3.10}$$

where $\Gamma_{\omega,\tilde{t}_i}(x,y)$ is the result of two-dimensional phase unwrapping at a fixed angular frequency ω and STFT with time step $\tilde{t}_i$, and V is the phase velocity. Since the processing is performed for a fixed plane parallel to OXY, only the planar components of the bulk wave vector can be extracted (if they exist). Thus, the wave vectors and phase velocities at the frequencies of interest can be extracted from the spectrogram slices as follows:

1. two-dimensional phase unwrapping (with smoothing by averaging in a small spatial domain);
2. calculation of phase gradient (with smoothing by averaging in a small spatial domain);
3. splitting a large area into small blocks and extracting the median wave vector (median component k_x and k_y from the set of values for a given block).

The beneficial effect of convolution filtering is shown in Figure 3.29: each convolution step reduces scattering of the extracted parameter and improves smoothness of the recovered field.

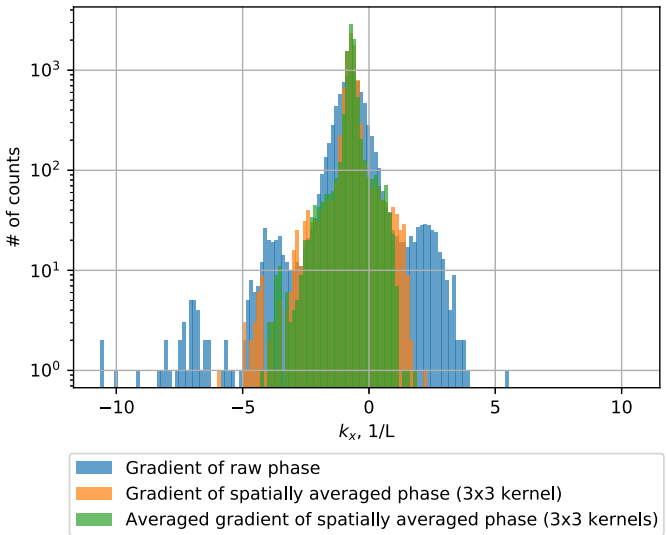
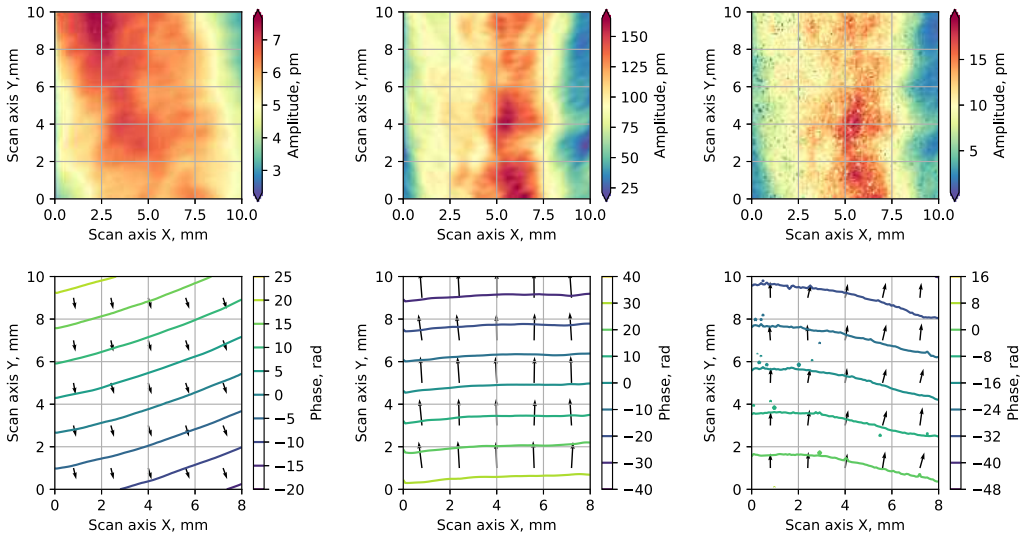


Figure 3.29: Effect of convolutional filtering on variance of extracted gradient component k_x.

The applicability of 2D phase unwrapping to LDV measurements to extract local wave vectors and phase velocities of surface elastic waves has been tested on synthetic and real LDV measurements. An example of wave vector processing and extraction for real measurement data is shown in Figure 3.30.



(a) 1.45 MHz (b) 3.3 MHz (c) 4.75MHz

Figure 3.30: Example of processing results for measured displacement data at frequencies of two overlapping surface waves for an angle of 165° between sources. The upper row shows the FFT amplitude distribution over the scan area. The lower row shows the results of phase reconstruction and wave vector extraction (arrows) over the scan area.

The presented approach can be used not only to extract local wave vectors and phase velocities but also to account for the real shape of the elastic wave source in the near field region. This approach has several advantages, such as high computational speed, clarity and interpretability.

On the other hand, the use of 2D phase-unwrapping algorithms requires high quality experimental data (high signal to noise ratio and measurements for at least six to ten cycles at the frequency of interest). It is also fundamentally impossible for this approach to distinguish multiple modes propagating at the same frequency.

3.4.6 Extraction of the radiation direction of elastic wave and its polarisation for sparse multidimensional data

The procedure described in 3.4.5 can only be applied for 2D surface measurements or FEM modelling, but not for 3D FEM modelling with multiple scattered wave modes (longitudinal and transverse). Along with the numerical problems of three-dimensional phase unwrapping, the principal inability to distinguish the contribution of each mode to the phase change makes it impractical. In contrast, three-dimensional laser Doppler vibrometry (currently widely available only up to 500 kHz) and numerical simulations using finite difference, finite volume or finite element methods allow to obtain all three components of the spatial displacement and their evolution over time to be tracked. Using the full vector field[2] $\vec{U}(x, y, z, t)$, the direction of propagation of bulk waves travelling at a known speed and the dominant polarisation in the presence of several components can be determined using another approach.

[2] displacement, velocity or acceleration

The following procedure has been implemented: assuming the presence of a coherent plane wave with a certain three-dimensional wave vector in a multidimensional FEM or experimental data volume, the phase shift between successive grid points for the virtual iterated wave vector can be calculated. This phase shift can be used to compensate for the phase shift of the temporal FFT $\vec{U}(x, y, z, \omega)$ known offset vector field at any frequency of interest, similar to known beamforming algorithms in the frequency domain. If the plane wave of interest is present in the simulation or measurement volume, the complex FFT coefficients with phase compensation are coherently summed to a large value. When the virtual wave vector used to calculate the phase shift and the wave propagation direction in the volume data do not match, the sum of the FFT coefficients is relatively small. Therefore, by changing the direction of the iterated wave vector in spherical coordinates (θ, φ) for known values $\left|\vec{k}\right|$, one can obtain a volumetric radiation pattern for each volumetric wave mode.

Exact algorithm is described below:

1. Generate the mesh of position vectors $\vec{r}(x, y, z)$ for the known FEM or experimental grid.
2. For every point (θ_i, φ_j) of the spherical coordinate grid with a 1° step in both polar and azimuthal directions and for a known frequency f and velocity V of the scattered wave:
   a) Calculate spherical coordinate system unit vectors $\vec{e}_r$, $\vec{e}_{\theta_i}$ and $\vec{e}_{\varphi_i}$ (defined in [Iso]) and the virtual wave vector $\vec{k}(\theta_i, \varphi_j)$

$$\vec{k}(\theta_i, \varphi_j) = 2\pi f/V \cdot \vec{e}_r \tag{3.11}$$

   b) Calculate the phase-shift factors F for known $\vec{k}(\theta_i, \varphi_j)$ and $\vec{r}(x, y, z)$

$$F_{\theta_i,\varphi_j}(x, y, z, f) = e^{i(\vec{k}(\theta_i,\varphi_j)\cdot\vec{r}(x,y,z))} \tag{3.12}$$

   c) Compensate the phase shift in complex displacement vectors (obtained by FFT of raw FEM simulation data) through multiplication by F

$$\vec{D}_{PC}(x, y, z, f) = \vec{D}(x, y, z, f)F_{\theta_i,\varphi_j}(x, y, z, f) \tag{3.13}$$

   where $\vec{D}$ and $\vec{D}_{PC}$ are raw and phase-compensated complex displacement vectors, correspondingly.

   d) Calculate the absolute value of the scalar product of the sum of complex $\vec{D}_{PC}$ with unit vectors $\vec{e}_r$, $\vec{e}_{\theta_i}$ and $\vec{e}_{\varphi_i}$ (resulting in P, SV, and SH wave-polarization vectors for the wave traveling in the $\vec{e}_r$ direction).

$$A_S(\theta_i, \varphi_j, \text{wavetype}, f) = \left| \left(\sum_{x,y,z} \vec{D}_{PC}(x, y, z, f) \right) \cdot \vec{e}_{\text{wavetype}} \right| \tag{3.14}$$

   where A_S is the scattering amplitude of the given wavetype in the given direction.

This procedure was first tested on synthetic data and then applied to multidimensional FEM[3] data (the evolution of three displacement components over time for the three-dimensional spatial grid). Using the algorithm, described above, the scattering direction in volume and the dominant polarisation were obtained.

[3] FEM simulations were performed by Dr. Peng Zuo (IC London) as part of collaboration [Gar22].

3.4.7 Local scattering efficiency by perturbation theory for wide-band primary pulses

With perturbation theory (Section 2.7) one can determine the intensity of a secondary wave generated by a nonlinear interaction of two monochromatic primary waves. However, these results cannot be directly compared with experimental results or FEM simulations for several reasons.

First, we do not have access to the freely propagating (plane) wave, but only to the wave field components at (experiment) or near (FEM simulation) the surface. Secondly, the input waves in the experiment were not monochromatic: during excitation, the powerful amplifier and transducer generate side nonlinearities. In addition, the fact that both the experimental and the available FEM source signals were time-limited extended the bandwidth of the fundamental waves, which contribute to the generated waves and thus to the non-linear mixing component.

These facts have to be taken into account in the perturbation approach in order to obtain values which can be compared with the experimental and FEM results. Therefore, the following procedure has been implemented:

1. parameterize the recorded frequency response (FR) of individual RW transducers ($\Lambda = 1, 2$) using the 3D FFT, and assuming only a single plane Rayleigh wave to be present, with the form
$$FR_\Lambda(\omega) = FFT(A_Z^{(\Lambda)}(X, Y, t)) = A_Z^{(\Lambda)}(k_x, k_y, \omega) = A_Z^{(\Lambda)}(\omega), \tag{3.15}$$
where A_Z is the measured out-of-plane displacement.

2. Calculate the out-of-plane displacement for the scattered wave $SW(\omega)$ for each possible combination of FR_1 and FR_2 spectral lines in the frequency range of interest (1–5 MHz) for varying source angle α from 45° to 180°, in 5° increments.

3. For each angle between sources and each frequency ω_i from the list (1.45, 3.3, 4.75 MHz), we obtain the resulting amplitude, which is a combination of the source waves and the scattered component:
$$A_Z(\omega_i) = \underbrace{|\langle FR_1(\omega) + FR_2(\omega) + SW(\omega)\rangle|}_{||\omega-\omega_i|<50kHz}, \tag{3.16}$$
where angle brackets denote averaging of complex amplitudes.

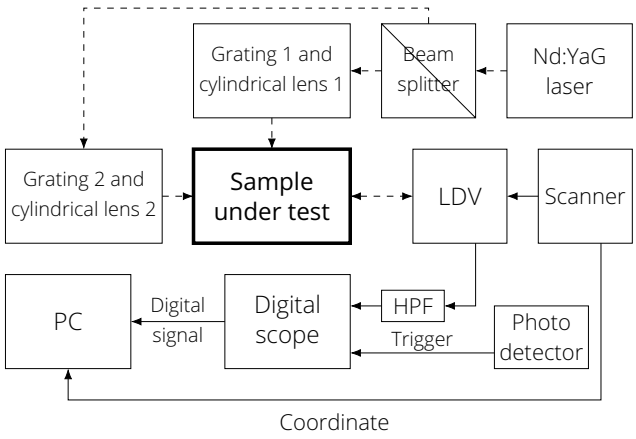
4. Calculate the local scattering efficiency H_Z (defined in equation (2.65)) for each angle between the sources.

The frequency band 50 *kHz* contains three spectral lines for the sampling rate and recording length used throughout the experiments. A comparison of Figures 4.7 and 4.8 can give an indication of how broadband excitation affects overall efficiency, and the increasing influence of this effect for relatively small angles between sources. This effect could also be the reason for the lack of a sharp peak in the Figure 4.7.

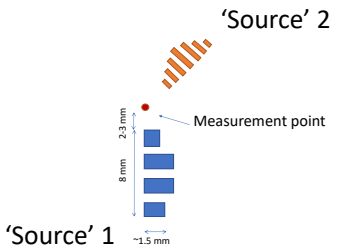
3.5 Supplementary study of applicability of contactless laser ultrasonics

A short complementary study on the applicability of a completely non-contact LUT to generate Rayleigh waves of a certain length with a Nd:YAG laser and to detect the nonlinear interaction with an LDV was carried out in the Acoustics and Biophysics Laboratory at KU Leuven. The working principle of LUT is based on a sudden thermal expansion created by heating the surface of a sample with a given pattern, which generates elastic waves.

A schematic representation of the setup and the resulting excitation points RW is shown in Figure 3.31. A short pulse with 10 Hz repetition rate generated by a 1064 nm pulsed laser (Quanta-Ray Spectra Physics) was split into two semicircles. Splitted light beam later was modulated by linear steel gratings with variable slit widths (Figure 3.32), placed at some distance to the sample surface. Splitted and modulated beam was focused by convex cylindrical lenses (the focal line of the lenses is parallel to the diameter of the semicircles) in vicinity of the sample surface.



(a) Here: Nd:YAG laser- high-power 1064 nm wave source, HPF - high-pass (4MHz) filter.



(b) Front view of laser ultrasonic excitation pattern.

Figure 3.31: LUT feasibility study: scheme and front view.

The results are shown in Figure 3.33. With a maximum source wave amplitude on the order of 1 nm, for the effects considered, the scattered wave amplitude must be on the order of 0.01-0.1 pm, which is at the edge of resolution limit of the available commercial LDV. Increasing the excitation amplitude is problematic due to the resulting ablation - removal of the surface layer of the material by the high-power laser beam. In addition, for some geometries, excitation through the grating results in a large number of spurious high-frequency components due to Fresnel diffraction, which also complicates the analysis of the data obtained.

Thus, the relatively low level of amplitude of the excited Rayleigh waves, and therefore low signal-to-noise, as well as a number of problems inherent to LUTs (low repetition rate, additional high frequency components due to optical effects) make this method a suboptimal choice for noncollinear wave mixing experiments at this stage.

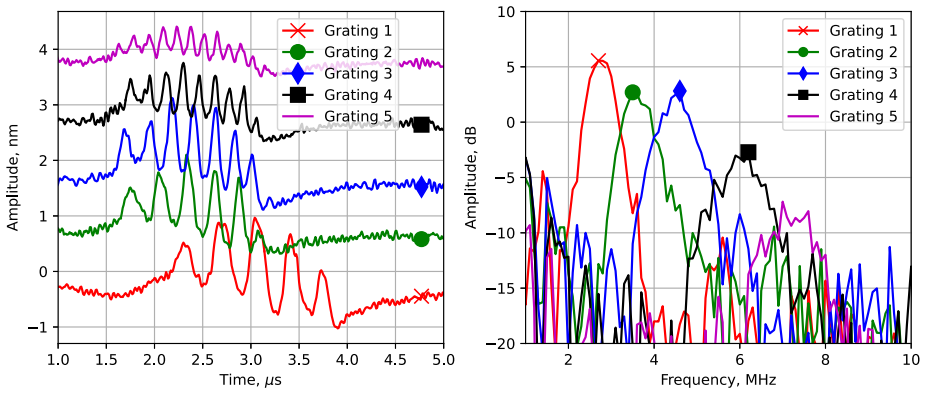


Figure 3.32: Temporal and frequency response for different gratings, evaluated without the HPF. Curves in the left subfigure are divided with an 1nm offset for readability.

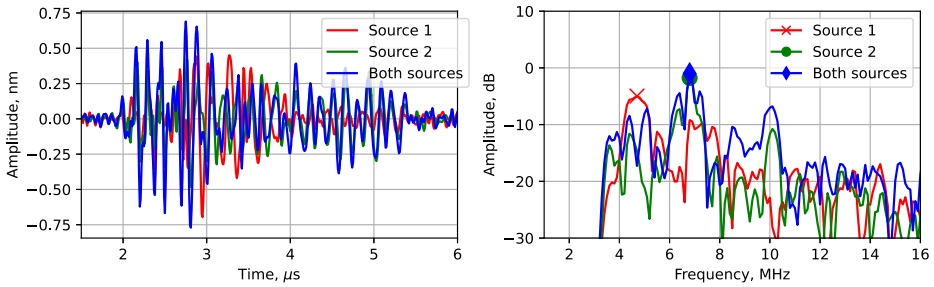


Figure 3.33: Case study: Applicabiltiy of noncontact LUT for generation of detection of wave mixing. No distinguishable wave interaction is detected.

4 Results

This chapter presents the results obtained and a brief analysis of the sources of experimental errors and uncertainties. These results include directly measured TOEC (3.1.1) and RW AEC (3.1.2) and their comparison via Grüneisen constants, RW AEC measurements for surface treated materials (3.1.2), Rayleigh wave dispersion over a wide frequency range (up to 25 MHz) (3.2). In addition, first results of numerical and experimental investigation of nonlinear elastic wave interaction (3.3) using the algorithms introduced in the previous chapter are also presented.

4.1 TOEC values for relevant superalloys

Third-order elastic constants were calculated according to the following scheme:

1. straight line fit with the OLS method (8.5) in (strain, relative velocity variation) domain,
2. extraction of slopes - acoustoelastic constants (Equation (2.32)),
3. calculation of the third-order elastic constants using Equations (2.33).

TOEC vaues, calculated from the direct BW AEC measurements (Section 3.4.2), and the comparison with the published results for the given superalloys, are given in Table 4.1. The available results for the In718 sample are in good correlation with the measured values. The high scattering of Ti6246 acoustoelastic constants (seen in Figure 4.1) was expected from previous works [Rje13], and can be explained by the spatial variation in the microstructural properties.

Material	l, GPa	m, GPa	n, GPa
In718 (5 points)	-556±5	-624±5	-484±5
In718 (3 points) [Rje13]	-524±4	-603±4	-478±2.3
In718 (3 points) [Hub12]	-472±19	-564±15	-489±7
Ti6246 (5 points)	-312±125	-309±71	-442±51
Ti6246 (3 points) [Rje13]	-356±35	-390±21	-475±15

Table 4.1: Third-order elastic constants (TOEC) values, calculated from BW AEC for annealed samples, and a comparison with the available literature values.

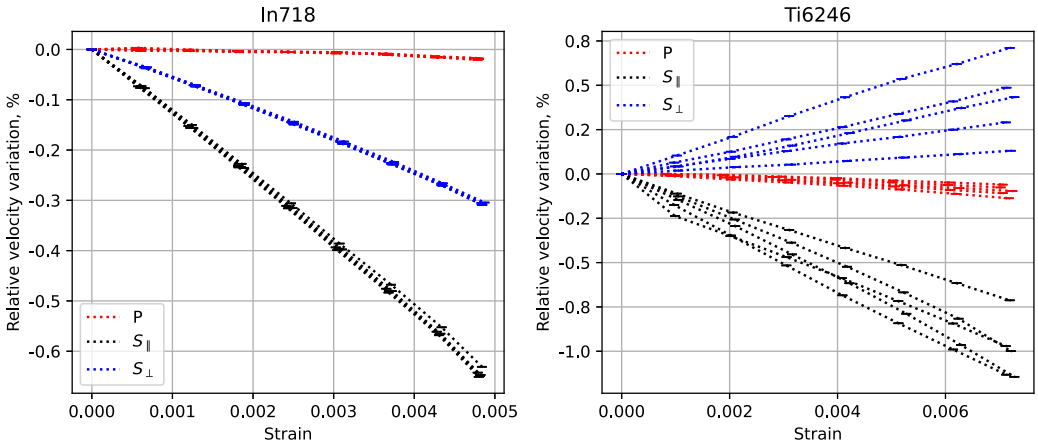


Figure 4.1: Raw measurement of elastic wave velocity variation for BW AEC evaluation. Each curve corresponds to a different measuring point, the vertical dashes show the standard deviation. The high scattering of nonlinear elastic characteristics of the Ti6246 alloy (on the right) is related to the variations in the microstructure.

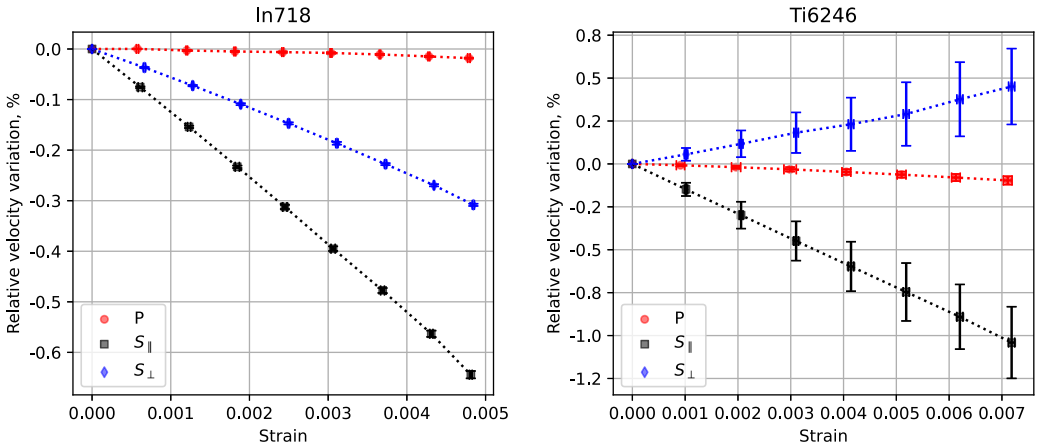


Figure 4.2: Relative velocity variation of the bulk wave modes due to uniaxial strain load for In718 and Ti6246 alloys. Here the standard deviation for strain and relative velocity variation for 5 different measurement points are given with dashes. P - pressure wave, S - shear wave with two possible polarizations (Figure 3.2a).

4.2 RW AEC values for relevant superalloys

The results of direct measurements of acoustoelastic constants, some of which were carried out for the first time (for surface treated materials), and a brief analysis of the sources of uncertainty in the experiment are presented below.

Results of RW AEC extractions for samples with different treatments are shown in table 4.2. A different history means that the same samples were measured after plastic deformation, annealing and shot peening. The RW AEC were measured with transducers with different centre frequency and bandwidth, giving different treatment depths (approximately 7 TD for 1.5 MHz, 2 TD for 5 MHz and 1 TD for 10 MHz transducers, respectively). This table

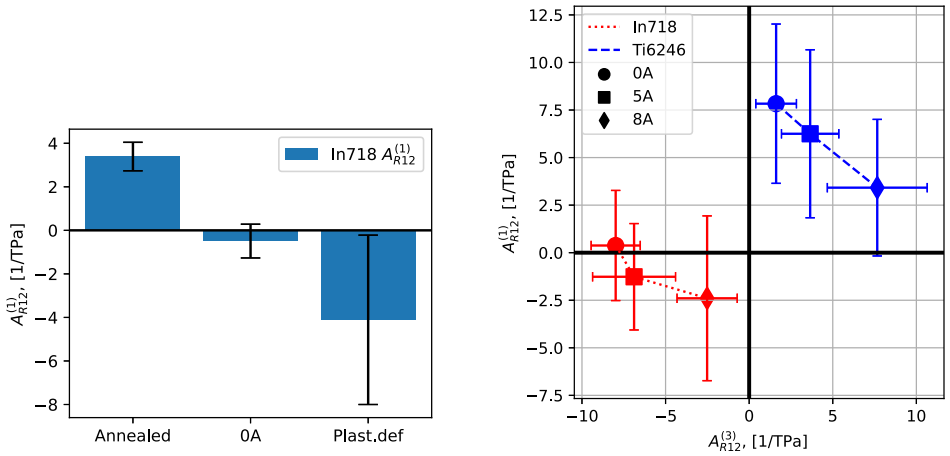
includes the values, mapped from the annealed sample BW AEC measurements (shown in bold), as well as several published results. Comparisons were done with the Lamé constants derived from literature density values and BW velocity measurements at zero load ($\rho_{In} = 8220\ kg/m^3$, $V^P_{In} = 5814\ m/s$, $V^S_{In} = 3096\ m/s$, $\rho_{Ti} = 4650\ kg/m^3$, $V^P_{Ti} = 6126\ m/s$, $V^S_{Ti} = 3150\ m/s$). As can be seen, the measured values of the constants $A^{(1)}_{R12}$ depend on the state of the material. BW AEC → TOEC → RW AEC mapping (Section 2.5.2) gives results close to the directly measured values only for $A^{(1)}_{R12}$ for titanium. The reasons for the deviation of the remaining *mapped* RW AEC from the *directly measured* values require further investigation.

In Figure 4.3a, the parameter $A^{(1)}_{R12}$ measured for three different states of the same sample In718 is shown by a vertical histogram. These states are shown on the horizontal axis: sample after annealing, after partial surface treatment (measurements were taken on the untreated area) and after plastic deformation. Because of the apparent anomalous behaviour, the measurements for state 0A were repeated several times but always showed a similar result. Both the magnitude and the sign of RW AEC depends on the processing history of the In718 alloy.

The effect of hardening intensity on the sign and magnitude of RW AEC for In718 and Ti6246 is shown in Figure 4.3b. Unlike titanium alloy, for which the "cumulative" nonlinearity $A^{(1)}_{R12}+A^{(3)}_{R12}$ retains its magnitude, for Inconel both acoustoelastic constants change strongly in magnitude and/or sign, which jeopardises its subsequent application for the assessment of residual stresses in the surface treated structure.

Material	f_c(MHz)	$A^{(1)}_{R12}(1/TPa)$	$A^{(3)}_{R12}(1/TPa)$
In718 (PD)	1.5	-4.11 ± 3.89	-1.73 ± 3.03
In718 (AA)	1.5	3.39 ± 0.66	-0.92 ± 0.77
In718 ([Köh10a])		2.36	-1.20
In718 (BW)		*2.18 ± 0.07*	*-1.31 ± 0.03*
In718 (0A)	1.5	-0.49± 0.78	
In718 (0A)	5	0.38 ± 2.90	-7.98 ± 1.47
In718 (0A)	10	0.23 ± 2.81	
In718 (5A)	5	-1.27 ± 2.80	-6.88 ± 2.48
In718 (5A)	10	-0.95 ± 1.84	
In718 (8A)	5	-2.40 ± 4.33	-2.51 ± 1.80
In718 (8A)	10	6.06 ± 1.25	
Ti6246 (PD)	1.5	0.32 ± 2.60	-2.36 ± 3.20
Ti6246 (AA)	1.5	3.36 ± 0.25	1.46 ± 2.10
Ti6246 ([Köh10a])		2.79	1.62
Ti6246 (BW)		*3.3 ± 2*	*5.81 ± 1.97*
Ti6246 (0A)	5	7.83 ± 4.19	1.61 ± 1.22
Ti6246 (5A)	5	6.25 ± 4.42	3.65 ± 1.72
Ti6246 (8A)	5	3.42 ± 3.59	7.66 ± 2.99

Table 4.2: Direct-measured RW AEC for the different states of material and comparison with the literature and mapped values (here, PD—plastically deformed; AA—after annealing; **BW** - mapped from the *BW AEC measurements*, available literature values are shown with the reference number). *Treatment and measurements at 0A, 5A, 8A states have been performed after annealing.*



(a) In718 $A_{R12}^{(1)}$ for three different sample states *(all without treatment, 0 A—measurements at nontreated part of the treated sample)*, f_c=1.5 MHz.

(b) RW AEC variation for 0 Almen (non-treated), 5 Almen, and 8 Almen shot-peening intensity for In718 and Ti6246 alloys, f_c = 5 MHz. Vertical axis—$A_{R12}^{(1)}$; horizontal axis—$A_{R12}^{(3)}$

Figure 4.3: Direct measurements of Rayleigh wave acoustoelastic constants for different states of surface treatment (Table 4.2).

All measurements were performed under laboratory conditions using commercial equipment. Additionally, reproducibility and the effect of setup parameters on measurement accuracy were analyzed using synthetic tests in MATLAB by varying the jitter delay between the excitation and recording and changing the accuracy of scanner positioning.

4.3 Rayleigh wave dispersion measurements

A semi-automatic method has been developed to combine measurements from ultrasonic transducers with different frequency ranges to increase the overall measurement bandwidth and improve the accuracy of the dispersion curves. The original method is described in 3.4.4, the measurement result for the respective samples is shown in Figure 4.4. Compared to the previous processing procedure [Bar12], the efficient frequency range has been increased by 10 MHz. HUGO has been designed specifically for measuring dispersion curves using the immersion method. Thus, the requirements for high signal to noise ratio and scanning accuracy are met by default. In this case the critical parameter to further improve the measurement accuracy is the monitoring of the elastic wave velocity in the water, which is temperature dependent and determines the critical angle.

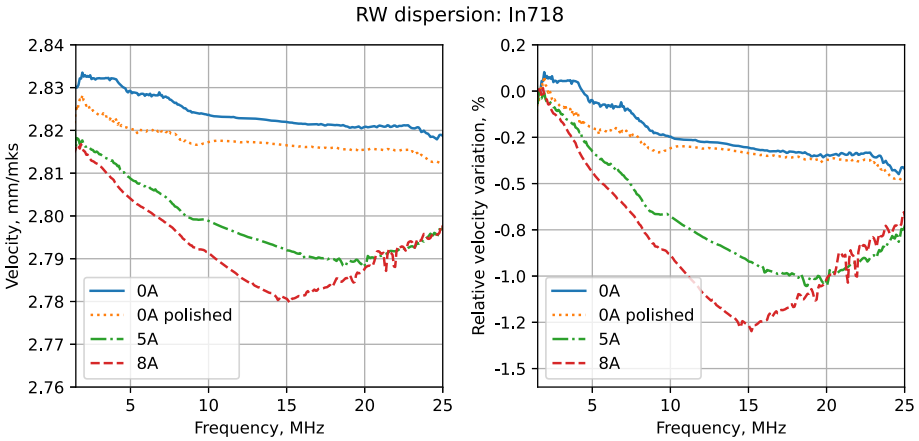


Figure 4.4: Rayleigh wave dispersion for surface-treated In718.

4.4 Nonlinear interaction of elastic waves and its potential for AEC estimation

In this section the results of theoretical and experimental investigation of possible nonlinear interactions of Rayleigh waves with nearly incident bulk waves are presented. The scattering efficiency is evaluated using perturbation theory (Section 2.7). For verification of experimental results and perturbation model simulations, as well as the algorithms developed, the results of additional FEM simulation, performed by Dr. Peng Zuo, are shown in several figures. These FEM simulations of nonlinear interaction of two Rayleigh waves, performed in Abaqus/Explicit package, resulted in three-component displacement vectors, which were simulated over a 4D (x, y, z, t) grid over a wide range of angles between the primary waves. Detailed description of FEM simulation is given in [Gar22].

All of the following graphs and explanations use the coordinate system shown in Figure 2.5.

4.4.1 Perturbation model

The results of the calculation of the scattering efficiency H of nearly incident scattered bulk waves ($\theta = 95°$) are shown in the Table 4.3 and shown in detail in Appendix 8.6. These values can be interpreted as the relative amplitude of the scattered wave at a significant distance from the interaction volume. Any pair of parameters from the list (f_1/f_2, α, α_2, θ) determines the other two, as well as the relative interaction efficiency for a given Rayleigh wave interaction. Similarly, the maximum efficiency values can be similarly, maximum efficiency values can be found by changing any two parameters in this list.

In addition, surface displacements in the interaction region have been calculated using a perturbation model (Section 2.7) and compared with the FEM simulation results (Figure 4.5). The perturbation model was in reasonable agreement with the FEM simulation results, adequately predicting order of magnitude of the displacement and following the general trend of the dependence of the scattered wave amplitude on the angle between the initial waves. In addition to this, the sensitivity of the local scattering efficiency H_Z to nonlinear elastic constants has been determined (see Section 4.4.4).

	Mixing case	ω_1/ω_2	Interaction efficiency Maximum	Median
$\omega_3 = \omega_1 + \omega_2$	RW+RW→P	0.07	3.43E+00	1.72E+00
	RW+RW→SV	0.68	1.08E+00	5.43E-01
	RW+P→P	0.83	2.23E-01	3.40E-02
	RW+P→SV	0.82	1.65E-02	9.56E-03
	RW+SV→P	0.07	1.52E-01	7.47E-02
	RW+SV→SV	0.96	2.73E-02	4.00E-03
$\omega_3 = \omega_1 - \omega_2$	P-RW→RW	14.41	1.03E+01	1.28E+00
	P-RW→P	13.49	5.76E-01	9.79E-02
	P-RW→SV	15.83	2.03E-01	4.81E-02
	P-P→RW	2.99	1.00E+04	2.13E-02
	P-SV→RW	15.10	1.87E-01	2.42E-02
	SV-RW→RW	7.93	3.99E+02	1.40E+00
	SV-RW→SV	8.25	7.80E+00	1.74E-02
	SV-P→RW	1.27	6.65E-03	4.59E-03
	SV-SV→RW	1.48	1.09E+04	2.74E-02

Table 4.3: Efficiencies H of allowed input combinations for scattered grazing bulk waves, considering Rayleigh waves (RW), pressure waves (P), and shear vertical waves (SV). Detailed simulation results are given in Figures 8.3–8.17. Wave interactions are abbreviated as [Source wave 1][scattered wave frequency][Source wave 2]→[scattered wave]. Due to normalisation features, the efficiencies for "+" and "-" cases should not be directly compared.

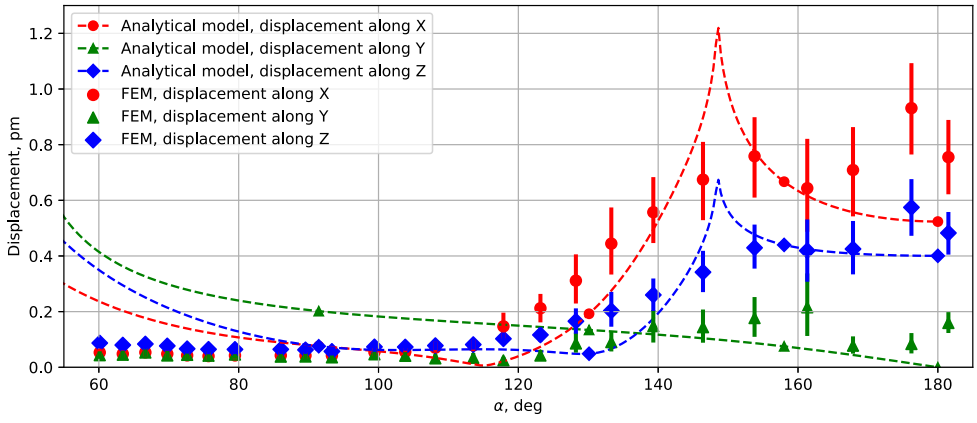


Figure 4.5: Dependence of the scattered wave displacement components (4.75 MHz) on the angle α between the primary waves. The vertical lines in the FEM data show the 95% confidence interval of the offsets obtained as described in Section 3.4.5. Here the TOEC values were multiplied by a factor of 150 to compensate for the low amplitudes of the original waves (short simulations).

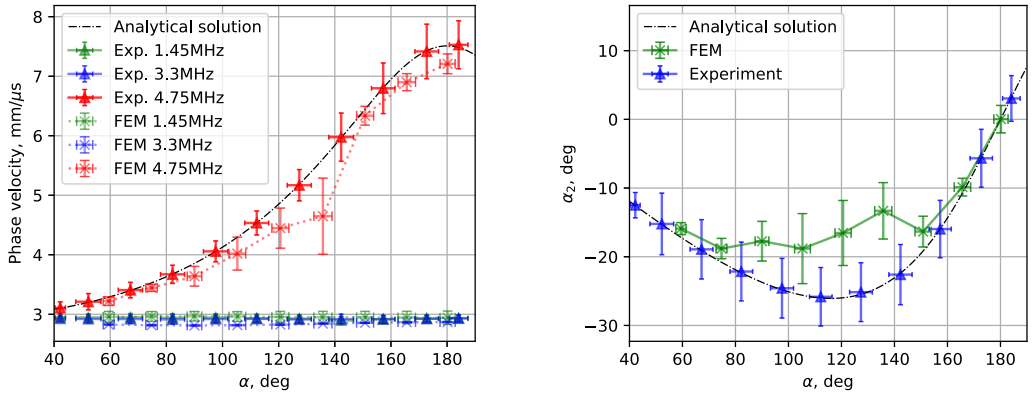
4.4.2 Experimental results

First, the sensitivity of the experimental setup to nonlinear Rayleigh wave interaction in metals has been demonstrated (details are given in Section 3.3).

The raw measurements (Figure 3.8) and its comparison with the available raw FEM data showed that the amplitude of the elastic wave interaction was about an order of magnitude higher than expected by analytical model and FEM (Figure 4.5).

Results of experiments, processed as described in Section 3.4.5, are shown in Figures 4.6 and 4.8. As can be seen from Figure 4.6, the experimentally measured directivities of the scattered waves were in good agreement with Equation (2.41) and the available FEM results. This fact also supports the statement that the measured component $\tilde{k}_3$ of the wave vector, follows the resonant (phase-matching) condition (2.41) and in fact, belongs to a scattered wave.

A comparison of local scattering efficiencies H_L (defined in Equation (2.65)), calculated analytically and extracted from experimental data, is given in Figure 4.8. As the real input signals contained not only the sine bursts at the desired frequencies, but also spurious wide-band components and amplifier-generated additional harmonics (Figure 3.8), the responses measured from isolated sources were used as input for the analytical model (this procedure is described in Section 3.4.7). The resulting measured and analytically predicted scattering efficiencies were of the same order of magnitude, following the same trend in range $\alpha \in (130°, 180°)$, having though a different increment.



(a) Comparison of analytical solution with $\tilde{k}_3$ from FEM and experimental data (Equation (3.9)).

(b) Comparison of analytical solution with $\tilde{k}_3$ directions, extracted from FEM and experimental data.

Figure 4.6: Fulfilment of resonance condition for scattered wave vector projection $\tilde{k}_3$ (Equation (2.42)). Experimental data and available FEM are processed as described in Section 3.4.5. FEM discrepancies at $\alpha \in (90°, 135°)$ are related to the limited number of Rayleigh wave source elements, which leads to larger variations for reconstructed phase surfaces in the near field for some geometrical configurations. Vertical and horizontal lines at the points denote numerical and measurement errors, respectively (standard deviation of parameters retrieved during processing).

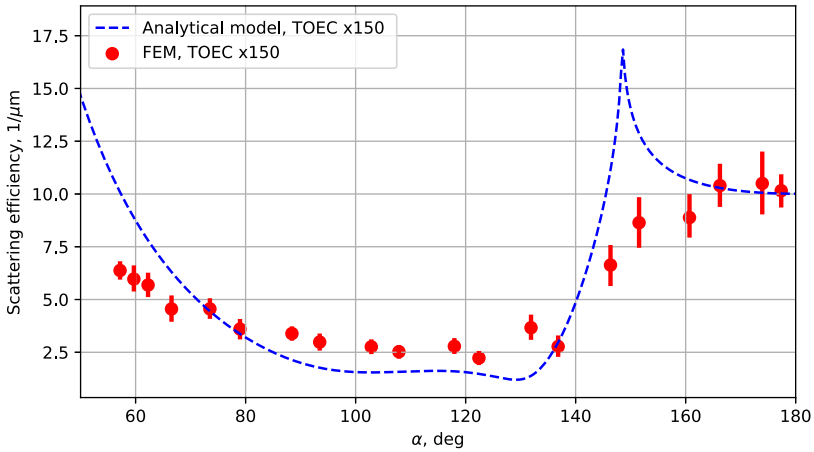


Figure 4.7: Comparison of local scattering efficiency H_Z from perturbation model and available FEM data (TOEC values multiplied by a factor of 150). The vertical lines on the FEM data show the 95% confidence interval of H_Z values, extracted as described in Section 3.4.5. Average amplitudes, $A_Z(\omega_1)$ and $A_Z(\omega_2)$, extracted from the FEM were used as input for the perturbation model.

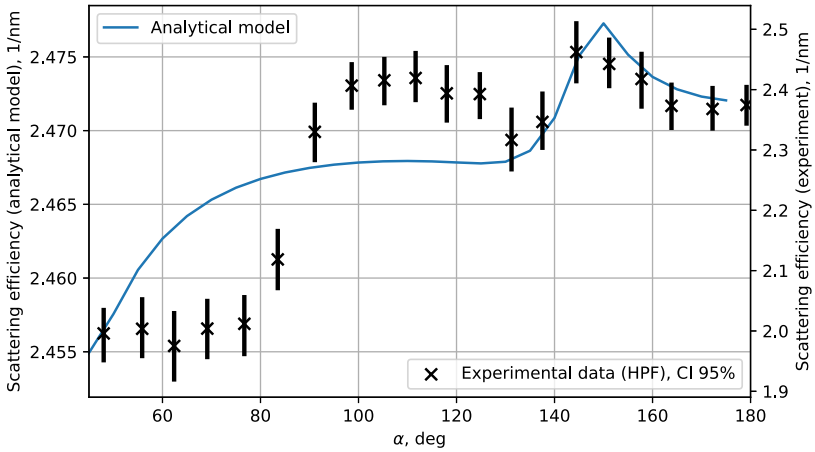


Figure 4.8: Comparison of local scattering efficiencies H_L (defined in Equation (2.65)) from perturbation model and experiment. The vertical lines on the experimental data show the 95% confidence interval of H_L values, extracted as described in Section 3.4.5. In order to account for the spurious effects from the experimental setup (especially the signal distortions by the amplifier at the start of a burst), measured frequency responses for both sources were used as inputs for the perturbation model (details in Section 3.4.7).

4.4.3 Extraction of propagation direction and dominant polarization from multidimensional data

Figure 4.9 shows the result of this extraction procedure, applied to the raw multidimensional FEM data[1] of the interaction of two RWs under an angle of 165 degrees between sources with frequencies of $f_1 = 1.45$ *MHz* and $f_2 = 3.3$ *MHz*. The narrow distribution of the extracted intensity radiation pattern and the position of its maximum, in agreement with the k-vector orientation according to the resonance condition (Equation (2.41)), suggests that, near the surface, the scattered wave field already has the form of a plane wave. Due to polarisation restrictions, the shear wave with horizontal polarization exists only in interaction volume.

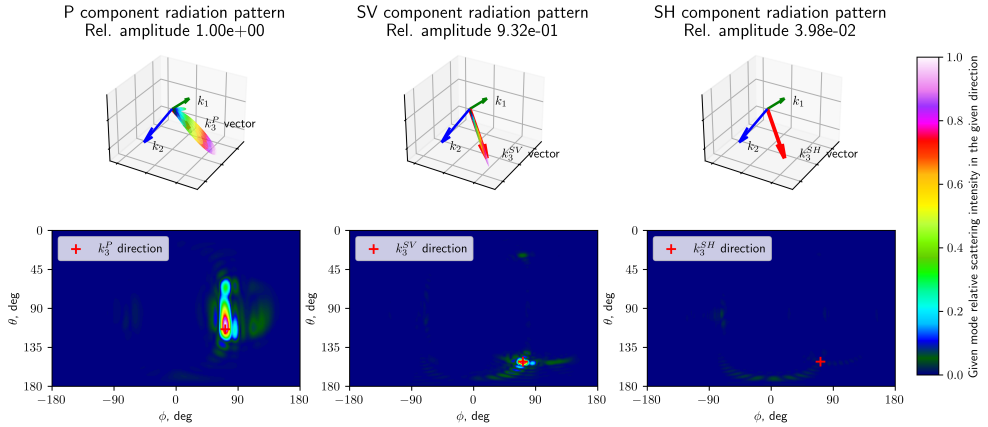


Figure 4.9: Extraction of volumetric propagation direction for three polarization components at the interaction frequency (4.75 MHz) and comparison with the resonant condition. Upper row: 3D radiation pattern for the given mode and the scaled wave vectors. Bottom row: color map of relative interaction efficiency in (φ, θ) coordinates and $\vec{k}_3$ orientation. The vectors $\vec{k}_1$ and $\vec{k}_2$ were directly extracted from available FEM data using the procedure described in Section 3.4.5. The vector $\vec{k}_3$ was derived from Equation (2.41) and the known value of $\left|\vec{k}_3\right|$.

This algorithm could be applied to any multidimensional data with known phase velocity and/or dispersion relations.

4.4.4 Sensitivity of local scattering efficiency to TOEC variation

As discussed in the previous chapters, at least three independent measurements are required to determine the three TOEC in nonlinear isotropic body. An analysis of the sensitivity of the elastic wave scattering efficiency to each of the elastic constants to be determined can help in the design of the experiment. The maximum/minimum sensitivity zones of each of the constants will prompt the optimum configuration for determining each of the third-order elastic constants.

Based on the perturbation theory formulated in Section 2.7, a brief analysis of sensitivity of the local scattering efficiency (2.65) to variations of TOEC has been performed. H_L can be written as a linear combination of the Murnaghan elastic constants l, m and n, plus a

[1] Interaction of two Rayleigh waves were simulated using the Abaqus/Explicit FEM software and three-component displacement vectors over a 4D (x, y, z, t) grid were extracted. Detailed description is given in [Gar22]

term which is independent of the TOEC:

$$H_L = H_L^0 + l\frac{\partial H_L}{\partial l} + m\frac{\partial H_L}{\partial m} + n\frac{\partial H_L}{\partial n}, \tag{4.1}$$

where H_L^0 and the sensitivities $\frac{\partial H_L}{\partial l}$, $\frac{\partial H_L}{\partial m}$ and $\frac{\partial H_L}{\partial n}$ depend on the second-order elastic constants, frequency ratio and angle between the initial waves. The dependence of the sensitivities on the angle between initial waves α for fixed f_1/f_2=1.45MHz/3.3MHz is given in Figure 4.10.

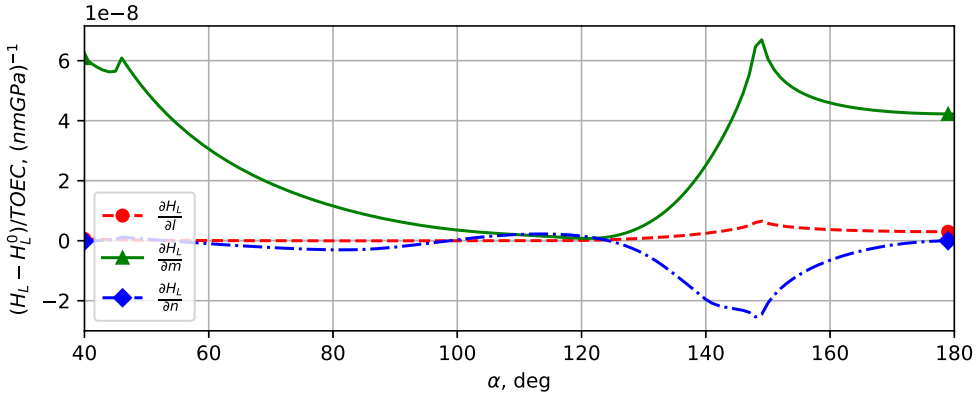


Figure 4.10: Sensitivity of local scattering efficiency H_L to the third order elastic constants (defined in Equation 4.1) versus the angle α between the primary waves.

Possible application of this result is discussed in the next chapter.

5 Discussion

5.1 Key parameters for the accuracy of the BW AEC and RW AEC measurements

First, TOEC have been measured by recording the variations in time-of-flight during the loading with the tensile machine. Direct measurements of bulk wave acoustoelastic constants impose the following requirements on the experimental setup:

- high sampling rate: in order to reliably resolve the minor variations in time-of-flight ΔTOF on the order of 0.01-1% of TOF, the minimal recording sampling rate SR should meet the following heuristic criterion:

$$SR \gtrapprox \frac{2}{\Delta TOF} = \frac{2}{0.01\%(2d/V)} \underset{V\sim 6mm/\mu s}{\overset{d\sim 5mm}{\approx}} 10GS/s \tag{5.1}$$

- High level of achieved strains/stresses (strains of at least 0.2 % for the alloys under investigation). For simple cases of uniaxial loading of solid specimens by means of a tensile machine, this condition may conflict with item 1, due to the competing specimen thickness demands.
- Several measurement points/areas.

Developed signal processing algorithms and routines, described in Sections 3.4.1 and 3.4.2, allow for semi-automated extraction of the desired parameters - Murnaghan constants (l, m, n).

Regarding the contactless measurements of RW AEC, the following parameters were identified as the most important for the accuracy.

- Signal-to-noise ratio: limitations on the amplitude of the electrical pulse and the efficiency of the piezoeffect on the amplitude of the excited wave and indirect scattering of light from the surface of the rough surface treated material.
- Positioning accuracy of the laser vibrometer beam: differences in measurement errors between vertical and horizontal axis scanning due to the features of industrial scanner design can be seen in Figure 4.3b, where $A^{(1)}_{R12}$ and $A^{(3)}_{R12}$ values are obtained with the vertical and horizontal line scans, correspondingly.

The necessity of use of direct measurements has been shown through comparison with the BW AEC values, measured for the same samples and mapped to the RW AEC. In the

given case, the mapped values and the values obtained by direct measurement for the annealed samples, have shown different results, except for the A^1_{R12} case for Ti6246. For the rest cases, the direct and mapped RW AEC values have shown a significant difference.

As shot-peened superalloys, RW AEC are highly sensitive to the treatment intensity and RW penetration depth, one should always account for the state of the material, penetration depth or bandwidth of interest, and wave propagation orientation. Thus, the aforementioned parameters should be determined in the actual region of interest, taking into account both the macro- and micro-structure of the material under test. The influence of the surface treatment on nonlinear elastic properties varies with the alloy type as well. In718 RW AEC tend to have stronger variations with the shot peening intensity, than the Ti6246.

5.2 Nonlinear interaction of Rayleigh waves as a prospective in-situ method for evaluation of surface layer nonlinear elastic constants

Allowed nonlinear interactions of surface and bulk waves were investigated using perturbation theory, providing a basic understanding of the influence of input frequencies and wave vectors of initial waves on the direction and intensity of the scattered wave. Quantitative analysis of the dependence of the interaction efficiency on the frequency ratio and angles between propagation directions for surface waves have been performed, as well as an evaluation of surface displacement amplitudes. Several processing algorithms for the extraction of parameters of interest from multi-dimensional data were introduced. The obtained parameters were wave vectors, phase velocities, radiation direction, wave interaction efficiency and dominant polarization. These methods are applicable to both FEM simulations and experimentally measured displacements. These tools were validated and successfully applied in this work and may be useful for future research of nonlinear wave interaction phenomena.

Next, the principal possibility for the detection of nonlinear mixing of surface and bulk waves in metals has been shown experimentally, as well as the current limitations of the available measurement setup have been highlighted:

- Limitation of the maximum amplitude of the excited elastic waves with commercial piezoelectric transducers.
- Features of short-time high frequency high voltage signals generation: high amount of harmonics induced and broadband parasitic components during the gate opening and closing of amplifier.
- Limited resolution of the 8-bit ADC.

Under the limitations of the setup (i.e., the maximal amplitudes of input Rayleigh waves were in the range of 10–25 nm), the dependence of the interaction efficiency on the angle between input wave vectors was assessed. These results were in rough qualitative agreement with the perturbation model.

The difference between predicted and measured scattering amplitude and the dependence of the interaction efficiency on the angle between source wave vectors for the perturbation model and the experimental data need further investigation. However, several potential reasons for the discrepancy can already be mentioned. First, the deviations between the literature values of TOEC, used for simulations, and the real one, as TOEC are strongly dependent not only on material type, but also on the processing history. At second, the effects, related to the microstructure of the sample at the surface layer (such as

microcracks, vacancies, dislocations and other) are ignored by the theoretical model using the assumption of isotropy, which could significantly affect the 'effective' higher-order elastic constants in the surface layer. Moreover, the limitations of the existing experimental setup (8-bit ADC resolution and transducer coupling variations, related to the positional change of the transducers on the surface) may have introduced additional errors.

As a further result, the information on the sensitivity of the wave amplitude generated by the two surface waves on the sample surface to non-linear elastic constants (Figure 4.10) have been obtained. It is important for the design of future experimental methods, allowing for the determination of near-surface TOEC, as the minimum of 3 independent measurements are required to determine the (l, m, n) constants triplet. For example, measurements for an angle α between 100 and 120 degrees can be used to determine the H_L^0. In the interval of 50 degrees it could be possible to determine the constant m. Knowing this, the constants l and n for intervals in 80 and 150 degrees, respectively, could be determined.

The future development of an experimental setup should include the application of customized transducers and electrical amplifiers in order to reach the desired amplitude levels of the source surface waves and high-power low-pass filters to minimize the spurious high-frequency components from the excitation path. After reaching Rayleigh wave amplitudes of roughly 50–100 nm for a 10 µs sine burst at 2–5 MHz, wave mixing measurements may become feasible for practical applications.

With the further improvement of numerical and analytical models, as well as the introduction of a purpose-tailored measurement setup, the in situ evaluation of surface-layer TOECs could become feasible by inversion of the angle- and frequency- dependent local scattering efficiencies H_Z. Finally, as the RW AECs could be obtained from TOECs, this inversion procedure will be one step further towards the long-term goal: acoustoelastic measurements for residual stress evaluation in surface treated components.

5.3 Suggestions for the design of future experiments to determine surface acoustoelastic constants

The achieved accuracy of measurements of surface acoustoelastic constants for surface-treated materials, evaluated for the first time (and varying from qualitative up to 20%) highlighted the need of a cutting-edge precision of experiment as well as the potential for future improvements in the measurement strategy. To improve the accuracy of the measurement of RW AEC for treated materials using noncontact methods (LUT or LDV), the following measures could be potentially applied:

- Application of high-precision step scanner and performing the scans with a spatial resolution in order of
$$\Delta x \sim \frac{\lambda_{RW}}{8} \sim \frac{400}{f_{MAX}} \mu m, \tag{5.2}$$
where λ_{RW} is the wavelength of Rayleigh wave and f_{MAX} is the maximal frequency of interest in MHz to allow for robust phase unwrapping and phase velocity reconstruction.
- Place the focusing lens at a minimum distance to the sample to maximise the SNR.
- (in case of piezoelectric excitation) application of sine burst/chirp sine signals to enhance the SNR in the frequency range of interest.

The sketch drawing of the prospective setup for contactless RW AEC measurement is shown in Figure 5.1.

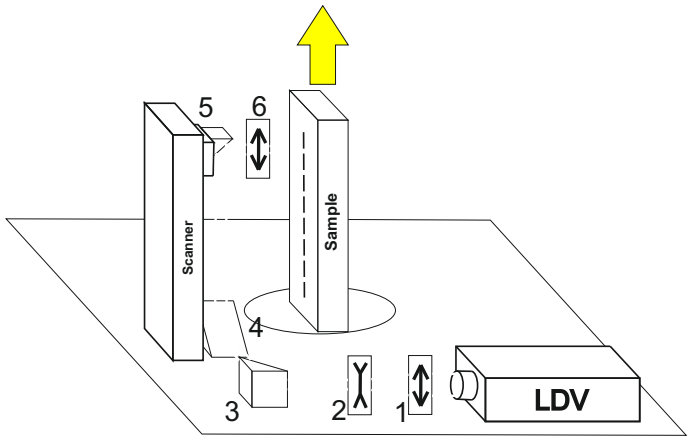


Figure 5.1: Schematic illustration of the RW AEC non-contact measurement setup. LDV, optical system and scanner are mounted on a platform rigidly connected to a tensile machine. In this Figure 1 and 6 are convex lenses for focusing the interferometer beam; 2 is a concave lens for creating a parallel beam; 3 and 4 - mirrors to rotate the beam parallel to the scanning axis (shown with a dashed line); 5 - mirror mounted on the movable part of the scanner to rotate the beam normally to the plane of the sample; 6 - convex lens mounted on the movable part of the scanner to focus the interferometer beam on the surface of the sample. The direction of loading is shown by the bold arrow.

With minimal modifications, the setup shown in the Figure 5.1 could be used to measure acoustoelastic constants at elevated temperatures.

Another possible way to measure Rayleigh acoustoelastic constants and their dependence on depth for surface treated metals would be to use high SNR immersive measurements together with an applied load. If the maximum level of strain on the order of 0.2% is reachable, Rayleigh wave dispersion measurements can provide information on both the dependence of the RW dispersion and the RW AEC dependence on the depth. With use of superbroadband transducers or with an automatic merging of dispersion curves in several frequency bands from the several probes using the algorithm presented in Section 3.4.4, it will be possible to reconstruct dispersion curves for velocity and dependence of RW AEC values on depth in the range from 1 to 30 MHz and above. A rough sketch for such setup is shown in the Figure 5.2.

It is worth noticing the following practical problems which may arise when attempting to implement such a method:

- Firstly, each of the possible solutions for the problem of measurements in water under external mechanical loading (sealing of the water tank, use of waterproof actuators, use of water jet coupling (squirters)) is related to technological difficulties.
- Secondly, additional FEM/experimental investigations of the actual stress-strain state are necessary when applying this method to real structural elements of complex shape (hollow blades or turbine disks). In addition, deformations and their influence on the shape of the scanning area have to be taken into account in the measurements.
- Finally, it is necessary to control the elastic wave velocity in the water in the measuring area, which is directly dependent on the water temperature. For example, this can be accounted by regular additional measurements with a U-shaped sample with known wall spacing, made of material with a low thermal expansion coefficient.

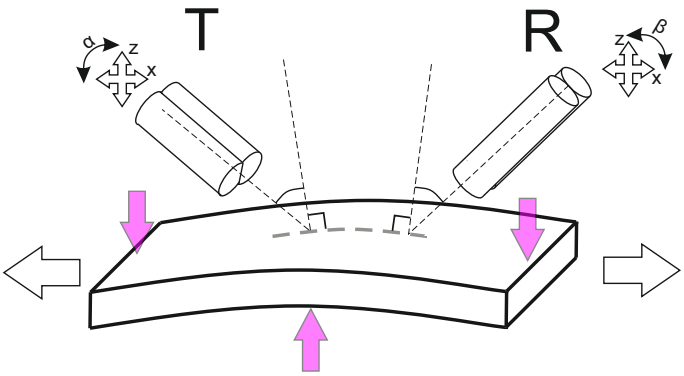


Figure 5.2: Schematic illustration of the concept for measuring the Rayleigh wave acoustoelastic constants for surface treated materials using immersion testing. Here, T is the transmitter and R is the receiver, exciting and measuring the RW, respectively. The required degrees of freedom (2 translational and 1 rotational for receiver and transmitter) are shown in the Figure. The possible types of loading are shown by arrows: by means of a waterproof actuator placed in a water tank (shaded arrows) and external tensile machine (white arrows).The scan line is shown as gray dashed line.

6 Conclusion

In this work the accuracy of available ultrasonic methods for determination of nonlinear elastic constants for stress level characterisation in metal samples and their practical applicability for the measurements in surface-treated specimens have been analysed and a novel in-situ approach have been introduced.

As a reference level for the quality of acoustoelastic experiment, as well as for determination of the TOEC l, m and n for In718 and Ti6246 superalloys, a series of velocities measurement under tensile loading have been carried out. The accuracy of laboratory measurements of bulk wave acoustoelastic constants (on the order of 1%) is an order of magnitude smaller than their local variations due to alloy structure and microdefects. Thus, a further increase in the resolution of the experiment is not reasonable.

Series of direct measurements of Rayleigh wave acoustoelastic constants, demanded for connection the variation in surface wave velocity to the surface layer stress state, for treated and untreated materials were made. These measurements have shown that even in the surface layer of untreated metals the Rayleigh wave acoustoelastic constants may differ from those obtained by mapping from the bulk ones, therefore posing a requirement for the direct measurements of RW AEC for each treatment state for the following application.

The final part of this work was the investigation of possibility of measuring the demanded TOEC or acoustoelastic constants in surface layer by nonlinear interaction of elastic waves in an isotropic material. This novel method was investigated by means of perturbation theory modelling and experiment and compared with FEM research data, obtained as part of joint work. The measurements have shown that the direction of scattered waves is well predicted by the existing models, while the scattering intensity is prognosed only qualitatively. Several possible reasons have been discussed in previous chapter.

In the future, with improvements in both the excitation and measurement parts, the method may have the potential for in-situ determination of the nonlinear elastic constants demanded to determine the residual stress levels in the metal. To increase the excitation amplitudes of the original waves, amplifiers and piezo-composite transducers optimised for the required excitation frequency, should be applied. Recent advances in production of lithography-processed metamaterials as resonators and vibration absorbers in MHz range also could help to improve the storage and transfer of vibrational energy from piezoelectric transducer to sample. In addition, high-power low pass filters should minimize the amount of amplifier-induced components above the excitation frequency. Finally, the recording with at least 16-bit ADC resolution will eliminate the need for high-pass filters and simplify post-processing, comparison and analysis.

Thus, maximum amplitudes excited by the piezoelectric effect and scanning accuracy are limiting the further development and potential application of residual stress measure-

ment methods using Rayleigh wave dispersion. Once the initial wave amplitudes are on the order of 50-100 nm, local in-situ measurements of the surface nonlinear elastic constants become feasible.

The development of a family of automatic and semi-automatic (requiring a single parameter tuning) procedures, visualisation methods and algorithms was an important part of this work. The resulting solutions for determining the group velocity from low SNR measurements, extraction of wave vectors and velocity fields from two-dimensional scans, and an algorithm for extraction and merging dispersion curves obtained from the transducers with different bandwidth could be useful in future research in the field of nonlinear ultrasound. Additional procedures, such as automated strain level extraction and visualisation of wave radiation direction and dominant polarisation for multidimensional data could be of interest in various fields of applied mechanics and non-destructive testing.

7 References

[AN10a] B. A. Abu-Nabah et al. “Limitations of Eddy Current Residual Stress Profiling in Surface-Treated Engine Alloys of Various Hardness Levels”. In: AIP, 2010. DOI: 10.1063/1.3362225.

[AN10b] Bassam A. Abu-Nabah et al. “The Effect of Hardness on Eddy Current Residual Stress Profiling in Shot-Peened Nickel Alloys”. In: *Journal of Nondestructive Evaluation* 29.3 (June 2010), pp. 143–153. DOI: 10.1007/s10921-010-0072-6.

[Ary18] Pouria Aryan, Santhakumar Sampath, and Hoon Sohn. “An Overview Of Nondestructive Testing Methods For Integrated Circuit Packaging Inspection”. In: *Sensors* 18.7 (June 2018), p. 1981. DOI: 10.3390/s18071981.

[Ast] *Test Method for Determining the X-Ray Elastic Constants for Use in the Measurement of Residual Stress Using X-Ray Diffraction Techniques*. DOI: 10.1520/e1426-14r19e01.

[Aul73] B.A. Auld. *Acoustic Waves And Fields In Solids. Part 1*. Ed. by. John Wiley & Sons, 1973. ISBN: 0-471-03702-8.

[Bai] Libing Bai and Gui Yun Tian. “Stress measurement using pulsed eddy current thermography”. In.

[Bar03] D. J. Barnard. “Monitoring Fatigue Damage Accumulation With Rayleigh Wave Harmonic Generation Measurements”. In: (2003). DOI: 10.1063/1.1570294.

[Bar12] M. Barth et al. “Universal ultrasonic goniometer for Rayleigh and surface skimming longitudinal wave dispersion measurements”. In: *Conference*. AIP, 2012. DOI: 10.1063/1.4716439.

[Ben13] Frank A. Bender et al. “The generation of second harmonic waves in an isotropic solid with quadratic nonlinearity under the presence of a stress-free boundary”. In: *Wave Motion* 50.2 (Mar. 2013), pp. 146–161. DOI: 10.1016/j.wavemoti.2012.08.009.

[Blo04] Mark P. Blodgett and Peter B. Nagy. “Eddy Current Assessment Of Near-surface Residual Stress In Shot-peened Nickel-base Superalloys”. In: *Journal of Nondestructive Evaluation* 23.3 (Sept. 2004), pp. 107–123. DOI: 10.1023/b:jone.0000048866.40648.fe.

[Bot18] Frantisek Botko et al. “Preliminary Study of Residual Stress Measurement Using Eddy Currents Phasor Angle”. In: *Advances in Manufacturing Engineering and Materials*. Springer International Publishing, Sept. 2018, pp. 386–397. DOI: 10.1007/978-3-319-99353-9_41.

[Bra54] G. Bradfield. "Improvements in ultrasonic flaw detection". In: *Journal of the British Institution of Radio Engineers* 14.7 (July 1954), pp. 303–308. DOI: 10.1049/jbire.1954.0041.

[Bra96] Don E Bray and Roderick K Stanley. *Nondestructive evaluation: a tool in design, manufacturing and service*. CRC press, 1996.

[Bre85] Leonid Brekhovskikh and Valery Goncharov. "Mechanics Of Continua And Wave Dynamics". In: (1985). DOI: 10.1007/978-3-642-96861-7.

[Bri25] Léon Brillouin. "Les tensions de radiation; leur interprétation en mécanique classique et en relativité". In: *Journal de Physique et le Radium* 6.11 (1925), pp. 337–353. DOI: 10.1051/jphysrad:01925006011033700.

[Cam89] Colin Campbell. *Surface Acoustic Wave Devices And Their Signal Processing Applications*. Boston: Academic Press, 1989. ISBN: 9780121573454.

[Car01] S. Carlsson and P.-L. Larsson. "On The Determination Of Residual Stress And Strain Fields By Sharp Indentation Testing." In: *Acta Materialia* 49.12 (July 2001), pp. 2193–2203. DOI: 10.1016/S1359-6454(01)00123-9.

[Car02] H. Carreon, P. B. Nagy, and M. P. Blodgett. "Thermoelectric Nondestructive Evaluation of Residual Stress in Shot-Peened Metals". In: *Research in Nondestructive Evaluation* 14.2 (June 2002), pp. 59–80. DOI: 10.1080/09349840209409705.

[Chi11] D.J. Child, G.D. West, and R.C. Thomson. "Assessment Of Surface Hardening Effects From Shot Peening On A Ni-based Alloy Using Electron Backscatter Diffraction Techniques". In: *Acta Materialia* 59.12 (July 2011), pp. 4825–4834. DOI: 10.1016/j.actamat.2011.04.025.

[Cho09] Sunglok Choi, Taemin Kim, and Wonpil Yu. "Performance Evaluation of RANSAC Family". In: (2009). DOI: 10.5244/C.23.81.

[Coo54] E.G. Cook and H.E. Valkenburg. "Surface Waves At Ultrasonic Frequencies". In: *ASTM Bulletin* 198 (1954), pp. 81–84.

[Cre67] D.I. Crecraft. "The measurement of applied and residual stresses in metals using ultrasonic waves". In: *Journal of Sound and Vibration* 5.1 (Jan. 1967), pp. 173–192. DOI: 10.1016/0022-460X(67)90186-1.

[Dem12] A. Demčenko et al. "Non-collinear wave mixing for non-linear ultrasonic detection of physical ageing in PVC". In: *NDT & E International* 49 (July 2012), pp. 34–39. DOI: 10.1016/j.ndteint.2012.03.005.

[Dem14] A. Demčenko, V. Koissin, and V.A. Korneev. "Noncollinear wave mixing for measurement of dynamic processes in polymers: Physical ageing in thermoplastics and epoxy cure". In: *Ultrasonics* 54.2 (Feb. 2014), pp. 684–693. DOI: 10.1016/j.ultras.2013.09.011.

[Dem15] A. Demčenko, L. Mainini, and V.A. Korneev. "A study of the noncollinear ultrasonic-wave-mixing technique under imperfect resonance conditions". In: *Ultrasonics* 57 (Mar. 2015), pp. 179–189. DOI: 10.1016/j.ultras.2014.11.009.

[Dgz] *https://www.dgzfp.de/Schulungen*.

[Dit96] John J. Ditri and Derrick Hongerholt. "Stress distribution determination in isotropic materials via inversion of ultrasonic Rayleigh wave dispersion data". In: *International Journal of Solids and Structures* 33.17 (July 1996), pp. 2437–2451. DOI: 10.1016/0020-7683(95)00165-4.

[Dit97] John J. Ditri. “Determination of nonuniform stresses in an isotropic elastic half space from measurements of the dispersion of surface waves”. In: *Journal of the Mechanics and Physics of Solids* 45.1 (Jan. 1997), pp. 51–66. DOI: 10.1016/S0022-5096(96)00075-0.

[Duq02] Marc Duquennoy et al. “Theoretical determination of Rayleigh wave acoustoelastic coefficients: comparison with experimental values”. In: *Ultrasonics* 39.8 (June 2002), pp. 575–583. DOI: 10.1016/S0041-624X(02)00262-7.

[EAS03] EASA. *Part-21 / AMC / GM*. 2003.

[ER13] Edwill Escobar-Ruiz et al. “Non-linear Ultrasonic NDE of Titanium Diffusion Bonds”. In: *Journal of Nondestructive Evaluation* 33.2 (Dec. 2013), pp. 187–195. DOI: 10.1007/s10921-013-0217-5.

[F. 84] F. Nizzoli and G. I. Stegeman. “Surface Excitations”. In: *Modern Problems in Condensed Matter Science*. Ed. by V.M. Agranovich and R. Loudon. Vol. 9. Modern Problems in Condensed Matter Science. New York : North-Holland, 1984. Chap. 2, pp. 236–305.

[FAA09] FAA. *Guidance for Parts Manufacturer Approval of Turbine Engine and Auxiliary Power Unit Parts under Test and Computation*. 2009.

[Fre60] Julian R. Frederick. “Use of Ultrasonic Surface Waves in the Determination of Residual Stress in Metals”. In: *The Journal of the Acoustical Society of America* 32.11 (Nov. 1960), pp. 1499–1499. DOI: 10.1121/1.1935177.

[Gar20] Sergey Gartsev and Bernd Köhler. “Direct measurements of Rayleigh wave acoustoelastic constants for shot-peened superalloys”. In: *NDT & E International* 113 (July 2020), p. 102279. ISSN: 0963-8695. DOI: 10.1016/j.ndteint.2020.102279.

[Gar22] Sergey Gartsev et al. “Nonlinear interaction of Rayleigh waves in isotropic materials: Numerical and experimental investigation”. In: *Ultrasonics* 122 (May 2022), p. 106664. DOI: 10.1016/j.ultras.2021.106664.

[Gau98] J. Gauthier, T.W. Krause, and D.L. Atherton. “Measurement of residual stress in steel using the magnetic Barkhausen noise technique”. In: *NDT & E International* 31.1 (Feb. 1998), pp. 23–31. DOI: 10.1016/s0963-8695(97)00023-6.

[Ghi94] Dennis C. Ghiglia and Louis A. Romero. “Robust two-dimensional weighted and unweighted phase unwrapping that uses fast transforms and iterative methods”. In: *Journal of the Optical Society of America A* 11.1 (Jan. 1994), p. 107. DOI: 10.1364/JOSAA.11.000107.

[Gol60] Goldberg. “On interaction of bulk propagational and shear waves”. In: *Akustichesckij Zhurnal* (1960).

[Gol88] Richard M. Goldstein, Howard A. Zebker, and Charles L. Werner. “Satellite radar interferometry: Two-dimensional phase unwrapping”. In: *Radio Science* 23.4 (July 1988), pp. 713–720. DOI: 10.1029/rs023i004p00713.

[Gol91] Arthur Goldberger. *A course in econometrics*. Cambridge, Mass: Harvard University Press, 1991. ISBN: 0674175441.

[Gra81] Karl F. Graff. *A History Of Ultrasonics*. Elsevier, 1981, pp. 1–97. DOI: 10.1016/B978-0-12-477915-0.50006-3.

[Gri61] T.N. Grigsby and E.J. Tajchman. “Properties of Lamb Waves Relevant to the Ultrasonic Inspection of Thin Plates”. In: *IRE Transactions on Ultrasonic Engineering* 8.1 (Mar. 1961), pp. 26–33. DOI: 10.1109/T-PGUE.1961.29277.

[Has09] Trevor Hastie, Robert Tibshirani, and Jerome Friedman. *The Elements of Statistical Learning: Data Mining, Inference, and Prediction, Second Edition*. SPRINGER NATURE, Feb. 2009. 745 pp. ISBN: 0387848576.

[Has18] Mostafa Hasanian and Cliff J. Lissenden. "Second order ultrasonic guided wave mutual interactions in plate: Arbitrary angles, internal resonance, and finite interaction region". In: 124.16 (Oct. 2018), p. 164904. DOI: 10.1063/1.5048227.

[Hay61] M. Hayes and R. S. Rivlin. "Surface waves in deformed elastic materials". In: *Archive for Rational Mechanics and Analysis* 8.1 (Jan. 1961), pp. 358–380. DOI: 10.1007/BF00277451.

[Her02] Miguel Arevallilo Herráez et al. "Fast two-dimensional phase-unwrapping algorithm based on sorting by reliability following a noncontinuous path". In: *Applied Optics* 41.35 (Dec. 2002), p. 7437. DOI: 10.1364/AO.41.007437.

[Her06] Jan Herrmann et al. "Assessment Of Material Damage In A Nickel-base Superalloy Using Nonlinear Rayleigh Surface Waves". In: *Journal of Applied Physics* 99.12 (June 2006), p. 124913. DOI: 10.1063/1.2204807.

[Hil06] Andrew J Hillis et al. "Global crack detection using bispectral analysis". In: *Proceedings of the Royal Society A: Mathematical, Physical and Engineering Sciences* 462.2069 (Feb. 2006), pp. 1515–1530. DOI: 10.1098/rspa.2005.1620.

[Hil10] S. Hillmann et al. "Experimental-based discussion for the separation of residual stresses and cold work in shot peened IN718 using high frequency Eddy current spectroscopy". In: AIP, 2010. DOI: 10.1063/1.3362224.

[Hir81] M. Hirao, H. Fukuoka, and K. Hori. "Acoustoelastic Effect Of Rayleigh Surface Wave In Isotropic Material". In: *Journal of Applied Mechanics* 48.1 (Mar. 1981), pp. 119–124. DOI: 10.1115/1.3157553.

[Hub12] Sebastian Hubel et al. "Basic Investigations to Establish an Ultrasonic Stress Evaluation Technique for Aero Engine Materials". In: *NDT in Aerospace 2012 - Th.1.B.3* (2012).

[Hub14] Sebastian Hubel et al. "Ultrasonic evaluation of residual stresses in aero engine materials using bulk and Rayleigh surface waves". In: (2014). DOI: 10.1063/1.4864876.

[Hug53] D. S. Hughes and J. L. Kelly. "Second-Order Elastic Deformation of Solids". In: *Physical Review* 92.5 (Dec. 1953), pp. 1145–1149. DOI: 10.1103/PhysRev.92.1145.

[Hus82] D. Husson and G. S. Kino. "A Perturbation Theory For Acoustoelastic Effects". In: *Journal of Applied Physics* 53.11 (Nov. 1982), pp. 7250–7258. DOI: 10.1063/1.331623.

[Hus85] D. Husson. "A Perturbation Theory For The Acoustoelastic Effect Of Surface Waves". In: *Journal of Applied Physics* 57.5 (Mar. 1985), pp. 1562–1568. DOI: 10.1063/1.334471.

[Ish18a] Yosuke Ishii, Shiro Biwa, and Tadaharu Adachi. "Non-collinear interaction of guided elastic waves in an isotropic plate". In: *Journal of Sound and Vibration* 419 (Apr. 2018), pp. 390–404. DOI: 10.1016/j.jsv.2018.01.031.

[Ish18b] Yosuke Ishii, Koichi Hiraoka, and Tadaharu Adachi. "Finite-element analysis of non-collinear mixing of two lowest-order antisymmetric Rayleigh–Lamb waves". In: *The Journal of the Acoustical Society of America* 144.1 (July 2018), pp. 53–68. DOI: 10.1121/1.5044422.

[Iso] *Quantities and units — Part 2: Mathematics, Standard,* International Organization for Standardization, Geneva, CH, 2019.

[Iwa78] Yukio Iwashimizu. "The Rayleigh wave in a finitely deformed isotropic elastic material". In: *The Journal of the Acoustical Society of America* 64.3 (1978), p. 910. DOI: 10.1121/1.382051.

[Jha09] Kyung-Young Jhang. "Nonlinear ultrasonic techniques for nondestructive assessment of micro damage in material: A review". In: *International Journal of Precision Engineering and Manufacturing* 10.1 (Jan. 2009), pp. 123–135. DOI: 10.1007/s12541-009-0019-y.

[Jin17] Jiao Jingpin et al. "Nonlinear Lamb wave-mixing technique for micro-crack detection in plates". In: *NDT & E International* 85 (Jan. 2017), pp. 63–71. DOI: 10.1016/j.ndteint.2016.10.006.

[Joh81] G. C. Johnson. "On the Applicability of Acoustoelasticity for Residual Stress Determination". In: *Journal of Applied Mechanics* 48.4 (Dec. 1981), pp. 791–795. DOI: 10.1115/1.3157735.

[Jon63] Gerald Lee Jones and Donald R. Kobett. "Interaction of Elastic Waves in an Isotropic Solid". In: *The Journal of the Acoustical Society of America* 35.1 (Jan. 1963), pp. 5–10. DOI: 10.1121/1.1918405.

[Ju19a] Taeho Ju et al. "Nondestructive evaluation of thermal aging of adhesive joints by using a nonlinear wave mixing technique". In: *NDT & E International* 103 (Apr. 2019), pp. 62–67. DOI: 10.1016/j.ndteint.2019.02.006.

[Ju19b] Taeho Ju et al. "One-way mixing of collinear waves in an adhesive layer". In: *The Journal of the Acoustical Society of America* 145.1 (Jan. 2019), pp. 110–120. DOI: 10.1121/1.5084734.

[Kal82] N. Kalyanasundaram, R. Ravindran, and P. Prasad. "Coupled amplitude theory of nonlinear surface acoustic waves". In: *The Journal of the Acoustical Society of America* 72.2 (Aug. 1982), pp. 488–493. DOI: 10.1121/1.388076.

[Kal83] N. Kalyanasundaram. "Nonlinear mixing of surface acoustic waves propagating in opposite directions". In: *The Journal of the Acoustical Society of America* 73.6 (June 1983), pp. 1956–1965. DOI: 10.1121/1.389586.

[Kof04] Bernard L. Koff. "Gas Turbine Technology Evolution: A Designers Perspective". In: *Journal of Propulsion and Power* 20.4 (July 2004), pp. 577–595. DOI: 10.2514/1.4361.

[Köh10a] B. Köhler et al. "Characterization of surface treated aeroengine alloys by Rayleigh wave velocity dispersion". In: *Conference*. AIP, 2010. DOI: 10.1063/1.3362402.

[Köh10b] Bernd Köhler et al. "Rayleigh wave velocity dispersion for characterization of surface treated aero engine alloys". In: *Proceedings of the ECNDT*. 2010.

[Kor14] V. A. Korneev and A. Demčenko. "Possible second-order nonlinear interactions of plane waves in an elastic solid". In: *The Journal of the Acoustical Society of America* 135.2 (Feb. 2014), pp. 591–598. DOI: 10.1121/1.4861241.

[Kor98] V.A. Korneev, K.T. Nihei, and L.R. Myer. *Nonlinear interaction of plane elastic waves*. Tech. rep. Berkeley Lab, June 1998. DOI: 10.2172/290877.

[Kra90] Josef Krautkrämer. *Ultrasonic testing of materials*. Berlin, Heidelberg: Springer Berlin Heidelberg, 1990. ISBN: 978-3-662-10680-8.

[KY93] B.T. Khuri-Yakub. "Scanning acoustic microscopy". In: *Ultrasonics* 31.5 (Sept. 1993), pp. 361–372. DOI: 10.1016/0041-624X(93)90070-G.

[Lan86] LD Landau and EM Lifshitz. "Theory of Elasticity, 3rd". In: *Pergamon Press* 3 (1986).

[L.D44] Landau L.D. and Lifschitz E.M. *Mechanics of the solid medium: hydrodynamics and elasticity theory (in russian)*. 1st ed. Vol. 3. Theoretical Physics. OGIZ GITTL, 1944.

[Lea70] E. G. Lean and C. C. Tseng. "Nonlinear Effects in Surface Acoustic Waves". In: *Journal of Applied Physics* 41.10 (Sept. 1970), pp. 3912–3917. DOI: 10.1063/1.1658386.

[Lei60] G. Leibfried and W. Ludwig. "Gleichgewichtsbedingungen in der Gittertheorie". In: *Zeitschrift fur Physik* 160.1 (Feb. 1960), pp. 80–92. DOI: 10.1007/bf01337481.

[Liu01] Q Liu et al. "Use of surface-treatment life extension methods for aircraft components". In: *ICF10, Honolulu (USA) 2001*. 2001.

[Liu11] Minghe Liu et al. "Experimental study of nonlinear Rayleigh wave propagation in shot-peened aluminum plates—Feasibility of measuring residual stress". In: *NDT & E International* 44.1 (Jan. 2011), pp. 67–74. DOI: 10.1016/j.ndteint.2010.09.008.

[Lur05] A. I. Lurie and Alexander Belyaev. "Theory of Elasticity". In: (2005). DOI: 10.1007/978-3-540-26455-2.

[M.02] Alberto Ruiz M. and Peter B. Nagy. "Diffraction Correction For Precision Surface Acoustic Wave Velocity Measurements". In: *The Journal of the Acoustical Society of America* 112.3 (Sept. 2002), pp. 835–842. DOI: 10.1121/1.1497368.

[Mad10] Elhoucine Madhi et al. "On the influence of cold work on resistivity variations with thermal exposure in IN-718 nickel-base superalloy". In: AIP, 2010. DOI: 10.1063/1.3362221.

[Man87] Chi-Sing Man and W. Y. Lu. "Towards an acoustoelastic theory for measurement of residual stress". In: *Journal of Elasticity* 17.2 (1987), pp. 159–182. DOI: 10.1007/BF00043022.

[Mat14] K. H. Matlack et al. "Review of Second Harmonic Generation Measurement Techniques for Material State Determination in Metals". In: *Journal of Nondestructive Evaluation* 34.1 (Nov. 2014). DOI: 10.1007/s10921-014-0273-5.

[May95] Andreas P Mayer. "Surface acoustic waves in nonlinear elastic media". In: *Physics Reports* 256.4-5 (1995), pp. 237–366.

[Mee81] G. W. Meetham, ed. *The Development of Gas Turbine Materials*. Springer Netherlands, 1981. DOI: 10.1007/978-94-009-8111-9.

[Mez74] R.S. Mezrich, K.F. Etzold, and D.H.R. Vilkomerson. "Ultrasonovision". In: (1974). DOI: 10.1109/ULTSYM.1974.196275.

[Min54] C. Minton. "Inspection of metals with ultrasonic surface waves". In: *Nondestructive Testing* 12.4 (1954), pp. 13–16.

[Moh19] Munawwar Mohabuth et al. "On the determination of the third-order elastic constants of homogeneous isotropic materials utilising Rayleigh waves". In: *Ultrasonics* 96 (July 2019), pp. 96–103. DOI: 10.1016/j.ultras.2019.02.006.

[Mon04] Jean-Pierre Monchalin. "Laser-Ultrasonics: From the Laboratory to Industry". In: (2004). DOI: 10.1063/1.1711602.

[Mor07] David Morgan. *Surface acoustic wave filters : with applications to electronic communications and signal processing*. Amsterdam London: Academic Press, 2007. ISBN: 9780123725370.

[Mor10] Maxim Morozov, Gui Yun Tian, and Philip J. Withers. "The pulsed eddy current response to applied loading of various aluminium alloys". In: *NDT & E International* 43.6 (Sept. 2010), pp. 493–500. DOI: 10.1016/j.ndteint.2010.05.004.

[Mor19a] P. Mora and M. Spies. “On the validity of several previously published perturbation formulas for the acoustoelastic effect on Rayleigh waves”. In: 91 (Jan. 2019), pp. 114–120. DOI: 10.1016/j.ultras.2018.07.020.

[Mor19b] P. Mora and M. Spies. “Perturbation theory for acoustoelastic effects in heterogeneous media”. In: *Wave Motion* 86 (Mar. 2019), pp. 1–10. DOI: 10.1016/j.wavemoti.2018.12.002.

[Mor22] Pierric Mora et al. “Nonlinear generation of a zero group velocity mode in an elastic plate by non-collinear mixing”. In: 119 (Feb. 2022), p. 106589. DOI: 10.1016/j.ultras.2021.106589.

[Mur51] FD Murnaghan. *Finite Deformation of an Elastic Solid, New York (1951)*. John Wiley and Sons, 1951.

[Nag06] P. B. Nagy. “Opportunities and Challenges for Nondestructive Residual Stress Assessment”. In: *AIP Conference Proceedings*. AIP, 2006. DOI: 10.1063/1.2184508.

[Ndt] *https://www.grandviewresearch.com/industry-analysis/non-destructive-testing-equipment-services-market*.

[Nor79] R. Normandin and G. I. Stegeman. “Surface-wave generation by nonlinear mixing of bulk waves”. In: *Journal of Applied Physics* 50.1 (Jan. 1979), pp. 87–90. DOI: 10.1063/1.325622.

[Oli21] Samuel Chukwuemeka Olisa, Muhammad A. Khan, and Andrew Starr. “Review of Current Guided Wave Ultrasonic Testing (GWUT) Limitations and Future Directions”. In: *Sensors* 21.3 (Jan. 2021), p. 811. DOI: 10.3390/s21030811.

[Opp09] Alan V. Oppenheim et al. *Discrete-Time Signal Processing*. Pearson (Verlag), 2009. ISBN: 978-0-13-198842-2.

[Pad76] T. C. Padmore and G. I. Stegeman. “Surface-wave nonlinearities: Nonlinear bulk-wave generation by two oppositely directed collinear surface waves”. In: *Journal of Applied Physics* 47.4 (Apr. 1976), pp. 1209–1228. DOI: 10.1063/1.322843.

[Pap08] M Ph Papaelias, C Roberts, and C L Davis. “A Review On Non-destructive Evaluation Of Rails: State-of-the-art And Future Development”. In: *Proceedings of the Institution of Mechanical Engineers, Part F: Journal of Rail and Rapid Transit* 222.4 (July 2008), pp. 367–384. DOI: 10.1243/09544097JRRT209.

[Pla83] H.J. Plaster. “The history and developments of the impact treatment processes”. In: *Journal of Mechanical Working Technology* 8.2-3 (Aug. 1983), pp. 203–216. DOI: 10.1016/0378-3804(83)90038-4.

[Pre04] Paul Prevey, Narayanan Jayaraman, and Ravi Ravindranath. “Mitigation of FOD and Corrosion Fatigue Damage in 17-4 PH Stainless Steel Compressor Blades With Surface Treatment”. In: (Mar. 2004), p. 11.

[Pre06] Paul S. Prevey et al. “Case Studies of Fatigue Life Improvement Using Low Plasticity Burnishing in Gas Turbine Engine Applications”. In: *Journal of Engineering for Gas Turbines and Power* 128.4 (Sept. 2006), pp. 865–872. DOI: 10.1115/1.1807414.

[Ray85] Lord Rayleigh. “On Waves Propagated along the Plane Surface of an Elastic Solid”. In: *Proceedings of the London Mathematical Society* s1-17.1 (Nov. 1885), pp. 4–11. DOI: 10.1112/plms/s1-17.1.4.

[Rje13] Marek Rjelka et al. “Third Order Elastic Constants and Rayleigh Wave Dispersion of Shot Peened Aero-Engine Materials”. In: *Materials Science Forum* 768-769 (Sept. 2013), pp. 201–208. DOI: 10.4028/www.scientific.net/MSF.768-769.201.

[Rje18] Marek Rjelka. "Simulationsgestützte Modellierung der elastischen Eigenschaften mikrorissbehafteter Materialien und deren nichtlineare Wechselwirkung mit geführten Wellen – Ein Beitrag zur zerstörungsfreien Charakterisierung des Eigenspannungsgradienten". PhD thesis. TU Dresden, 2018.

[Rol64] Fred R. Rollins, Lyle H. Taylor, and Paul H. Todd. "Ultrasonic Study of Three-Phonon Interactions. II. Experimental Results". In: *Physical Review* 136.3A (Nov. 1964), A597–A601. DOI: 10.1103/physrev.136.a597.

[Ros10] Joseph Rose. "Successes and challenges for ultrasonic testing in NDT and SHM". In: *Materials Evaluation* 68 (May 2010), pp. 494–500.

[Ros12] N.S. Rossini et al. "Methods of measuring residual stresses in components". In: *Materials & Design* 35 (Mar. 2012), pp. 572–588. DOI: 10.1016/j.matdes.2011.08.022.

[Ros84] R G Ross et al. "Thermal conductivity of solids and liquids under pressure". In: *Reports on Progress in Physics* 47.10 (Oct. 1984), pp. 1347–1402. DOI: 10.1088/0034-4885/47/10/002.

[Rui04] Alberto Ruiz and Peter B. Nagy. "Laser-ultrasonic surface wave dispersion measurements on surface-treated metals". In: *Ultrasonics* 42.1-9 (Apr. 2004), pp. 665–669. DOI: 10.1016/j.ultras.2004.01.045.

[Sav70] G. N. Savin and Y. I. Koifman. "The general nonlinear theory of elasticity". In: *Soviet Applied Mechanics* 6.12 (Dec. 1970), pp. 1275–1295. DOI: 10.1007/bf00888819.

[Sch06] Volker Schulze. *Modern Mechanical Surface Treatment - States, Stability, Effects*. New York: John Wiley & Sons, 2006. ISBN: 978-3-527-60716-7.

[Sch14] Gary S. Schajer. *Practical Residual Stress Measurement Methods*. Ed. by Gary S. Schajer. Wiely, 2014. ISBN: 9781118342374.

[Shu93] D. J. Shull et al. "Harmonic generation in plane and cylindrical nonlinear Rayleigh waves". In: *The Journal of the Acoustical Society of America* 94.1 (July 1993), pp. 418–427. DOI: 10.1121/1.407053.

[Sok29] S.Y. Sokolov. "Zur Frage der Fortpflanzung ultra-akustischer Schwingungen in verschiedenen Korpern". In: *Elektrische Nachrichten-Technik* 6 (1929), pp. 454–461.

[Sol15] Igor Solodov et al. "Highly-efficient and noncontact vibro-thermography via local defect resonance". In: *Quantitative InfraRed Thermography Journal* 12.1 (Jan. 2015), pp. 98–111. DOI: 10.1080/17686733.2015.1026018.

[Str99] J. Strand, T. Taxt, and A.K. Jain. "Two-dimensional phase unwrapping using a block least-squares method". In: *IEEE Transactions on Image Processing* 8.3 (Mar. 1999), pp. 375–386. DOI: 10.1109/83.748892.

[Sun18] Maoxun Sun et al. "Scanning non-collinear wave mixing for nonlinear ultrasonic detection and localization of plasticity". In: *NDT & E International* 93 (Jan. 2018), pp. 1–6. DOI: 10.1016/j.ndteint.2017.09.010.

[Sza75] T. L. Szabo. "Obtaining subsurface profiles from surface-acoustic-wave velocity dispersion". In: *Journal of Applied Physics* 46.4 (Apr. 1975), pp. 1448–1454. DOI: 10.1063/1.321793.

[Tan73] William J. Tanski and Walter G. Mayer. "Further investigation of noncollinear surface-wave interactions". In: *Journal of Applied Physics* 44.1 (Jan. 1973), pp. 506–507. DOI: 10.1063/1.1661920.

[Tay64] Lyle H. Taylor and Fred R. Rollins. “Ultrasonic Study of Three-Phonon Interactions. I. Theory”. In: *Physical Review* 136.3A (Nov. 1964), A591–A596. DOI: 10.1103/physrev.136.a591.

[Tia16] Gui Tian et al. “Eddy Current Pulsed Thermography with Different Excitation Configurations for Metallic Material and Defect Characterization”. In: *Sensors* 16.6 (June 2016), p. 843. DOI: 10.3390/s16060843.

[Tri04] Terry M. Tritt, ed. *Thermal Conductivity*. Springer US, 2004. DOI: 10.1007/b136496.

[Tyn27] E. P. T. Tyndall and J. M. B. Kellogg. “Note on the Barkhausen Effect under Mechanical Stress”. In: *Physical Review* 30.3 (Sept. 1927), pp. 354–356. DOI: 10.1103/PhysRev.30.354.

[Vel74] P. J. Vella et al. “Nonlinear surface-wave interactions: Parametric mixing and harmonic generation”. In: *Journal of Applied Physics* 45.5 (May 1974), pp. 1993–2006. DOI: 10.1063/1.1663536.

[Wag99] L Wagner. “Mechanical surface treatments on titanium, aluminum and magnesium alloys”. In: *Materials Science and Engineering: A* 263.2 (May 1999), pp. 210–216. DOI: 10.1016/S0921-5093(98)01168-X.

[Wan18] Zijun Wang et al. “Image processing based quantitative damage evaluation in composites with long pulse thermography”. In: *NDT & E International* 99 (Oct. 2018), pp. 93–104. DOI: 10.1016/j.ndteint.2018.07.004.

[Yin13] Aijun Yin et al. “Physical interpretation and separation of eddy current pulsed thermography”. In: *Journal of Applied Physics* 113.6 (Feb. 2013), p. 064101. DOI: 10.1063/1.4790866.

[Zab92] E. A. Zabolotskaya. “Nonlinear propagation of plane and circular Rayleigh waves in isotropic solids”. In: *The Journal of the Acoustical Society of America* 91.5 (May 1992), pp. 2569–2575. DOI: 10.1121/1.402993.

[Zar66] L.K. Zarembo and W.A. Krasilnikov. *Introduction to Nonlinear Acoustics*. Nauka, 1966.

[Zei82] Aharon Zeiger and Kenneth Jassby. “Measurement of acoustoelastic coefficients of Rayleigh waves in steel alloys”. In: *Journal of Nondestructive Evaluation* 3.2 (June 1982), pp. 115–124. DOI: 10.1007/bf00568968.

[Zha18] Zixin Zhao et al. “Robust 2D phase unwrapping algorithm based on the transport of intensity equation”. In: *Measurement Science and Technology* 30.1 (Nov. 2018), p. 015201. DOI: 10.1088/1361-6501/aaec5c.

[Zil01] Vladimir Zilberstein. “Applications Of Spatially Periodic Field Eddy Current Sensors For Surface Layer Characterization In Metallic Alloys”. In: *AIP Conference Proceedings*. AIP, 2001. DOI: 10.1063/1.1373863.

8 Appendix

8.1 Calculation of bulk waves acoustoelastic constants

Here the detailed procedure from [Hug53] is given. Introducing the general infinitesimal Cauchy strain tensor u_{rs} (Equation (2.2)), superimposed over a homogeneous triaxial finite strain with the coordinate axis as principal axes:

$$\begin{aligned} &x'_r = A_r x_r + u_r(\boldsymbol{x}), r = 1,2,3; \text{ where the de-dimensionalized } \tilde{u}_r = u_r/[L] \\ &\tilde{u}_r(\boldsymbol{x}) \ll A_r - 1. \end{aligned} \tag{8.1}$$

Lagrangian strain components are given by

$$\begin{aligned} &\eta_{rs} = \alpha_r \delta_{rs} + A_r A_s u_{rs}, \text{ where} \\ &\alpha_r = \frac{1}{2}(A_r^2 - 1), \end{aligned} \tag{8.2}$$

and δ_{rs} is a Kronecker function. The stresses are given by:

$$\begin{aligned} T_{rs} &= T^0_{rs} + C_{rstu}\partial u_t/\partial x_u, \text{ where} \\ T^0_{rs} &= [\lambda + (l - m - \lambda)\theta + (\lambda + m - \mu)\alpha_r]\theta\delta_{rs} + 2\mu(\alpha_r + 2\alpha_r^2)\delta_{rs} + m\sum_t \alpha_t^2\delta_{rs} + \frac{1}{2}n\delta^{rtu}_{stu}\alpha_t\alpha_u, \\ C_{rstu} &= [\lambda + 2(l - \lambda - m)\theta + 2(\lambda + m)(\alpha_r + \alpha_t) - 2\mu\alpha_r]\delta_{rs}\delta_{tu} + \\ &\quad [\mu + (\lambda + m - \mu)\theta + 2\mu(\alpha_r + \alpha_s + \alpha_u)][\delta_{rt}\delta_{su} + \delta_{ru}\delta_{st}] + \frac{1}{2}n(\delta^{rvu}_{svt} + \delta^{rvt}_{svu})\alpha_v, \\ \theta &= \alpha_1 + \alpha_2 + \alpha_3. \end{aligned} \tag{8.3}$$

Velocity V is given by solutions of

$$\det\left|C_{rstu}i_r i_u - V^2\delta_{st}\right| = 0. \tag{8.4}$$

and three corresponding solutions for the wave, propagating along the axis '1' :

$$\begin{aligned} \rho_0 V_1^2 &= \lambda + 2\mu + (2l + \lambda)\theta + (4m + 4\lambda + 10\mu)\alpha_1, \\ \rho_0 V_2^2 &= \mu + (\lambda + m)\theta + 4\mu\alpha_1 + 2\mu\alpha_2 - \frac{1}{2}n\alpha_3, \\ \rho_0 V_3^2 &= \mu + (\lambda + m)\theta + 4\mu\alpha_1 + 2\mu\alpha_3 - \frac{1}{2}n\alpha_2. \end{aligned} \tag{8.5}$$

8.2 Algebraic expressions for RW AEC calculation from the known SOEC, TOEC and velocities of bulk and Rayleigh waves

The coefficients in Equation (2.35) could be expressed explicitly in terms of SOEC (λ, μ), TOEC (l, m, n), and longitudinal, shear and Rayleigh wave velocities (V_L, V_T, V_R), correspondingly from the work [May95]:

$$h/h_0 = \frac{A\lambda + B\mu + Cl + Dm + En}{F\mu},$$
$$h_2/h_0 = \frac{G(\lambda + m + n) + H\mu}{l\mu}, \text{ where}$$

$$\begin{aligned}
A &= 28V_L^6V_R^4V_T^2 - 40V_L^6V_R^2V_T^4 + 16V_L^6V_T^6 - 28V_L^4V_R^6V_T^2 - 12V_L^4V_R^4V_T^4 + 80V_L^4V_R^2V_T^6 - 48V_L^4V_T^8 \\
&\quad + 56V_L^2V_R^6V_T^4 - 92V_L^2V_R^4V_T^6 + 8V_L^2V_R^2V_T^8 + 32V_L^2V_T^{10} - 20V_R^6V_T^6 + 60V_R^4V_T^8 - 40V_R^2V_T^{10}, \\
B &= -24V_L^8V_R^4 + 28V_L^8V_R^2V_T^2 - 8V_L^8V_T^4 + 24V_L^6V_R^6 + 80V_L^6V_R^4V_T^2 - 152V_L^6V_R^2V_T^4 + 64V_L^6V_T^6 \\
&\quad - 108V_L^4V_R^6V_T^2 + 20V_L^4V_R^4V_T^4 + 204V_L^4V_R^2V_T^6 - 136V_L^4V_T^8 + 140V_L^2V_R^6V_T^4 - 228V_L^2V_R^4V_T^6 + 16V_L^2V_R^2V_T^8 \\
&\quad + 80V_L^2V_T^{10} - 40V_R^6V_T^6 + 120V_R^4V_T^8 - 80V_R^2V_T^{10}, \\
C &= 8V_L^2V_R^6V_T^4 - 24V_L^2V_R^4V_T^6 + 16V_L^2V_R^2V_T^8 - 8V_R^6V_T^6 + 24V_R^4V_T^8 - 16V_R^2V_T^{10}, \\
D &= 28V_L^6V_R^4V_T^2 - 40V_L^6V_R^2V_T^4 + 16V_L^6V_T^6 - 28V_L^4V_R^6V_T^2 - 12V_L^4V_R^4V_T^4 + 80V_L^4V_R^2V_T^6 - 48V_L^4V_T^8 \\
&\quad + 52V_L^2V_R^6V_T^4 - 80V_L^2V_R^4V_T^6 + 32V_L^2V_T^{10} - 16V_R^6V_T^6 + 48V_R^4V_T^8 - 32V_R^2V_T^{10}, \\
E &= -3V_L^8V_R^4 + 2V_L^8V_R^2V_T^2 + 3V_L^6V_R^6 + V_L^6V_R^4V_T^2 - 2V_L^6V_R^2V_T^4 - 3V_L^4V_R^6V_T^2 + 2V_L^4V_R^4V_T^4, \\
F &= 24V_L^6V_R^4V_T^2 - 16V_L^6V_R^2V_T^4 - 16V_L^4V_R^6V_T^2 - 32V_L^4V_R^4V_T^4 + 32V_L^4V_R^2V_T^6 + 16V_L^2V_R^6V_T^4 + 8V_L^2V_R^4V_T^6 \\
&\quad - 16V_L^2V_R^2V_T^8, \\
G &= -16V_L^2V_R^4V_T^2 + 32V_L^2V_R^2V_T^4 - 16V_L^2V_T^6 + 8V_R^6V_T^2 - 24V_R^2V_T^6 + 16V_T^8, \\
H &= -12V_L^4V_R^4 - 4V_L^4V_R^2V_T^2 + 8V_L^4V_T^4 + 12V_L^2V_R^6 - 20V_L^2V_R^4V_T^2 + 72V_L^2V_R^2V_T^4 - 48V_L^2V_T^6 \\
&\quad + 4V_R^6V_T^2 - 52V_R^2V_T^6 + 40V_T^8, \\
I &= -12V_L^4V_R^4 + 8V_L^4V_R^2V_T^2 + 8V_L^2V_R^6 + 16V_L^2V_R^4V_T^2 - 16V_L^2V_R^2V_T^4 - 8V_R^6V_T^2 - 4V_R^4V_T^4 \\
&\quad + 8V_R^2V_T^6.
\end{aligned} \tag{8.6}$$

8.3 Parameters of Rayleigh wave dispersion inversion

Functions F_i have the following general form [Dit97]:

$$\begin{gathered}
F_i(X_3, \omega) = \omega^2\{f_{i1}e^{2\omega\kappa_s X_3} + f_{i2}e^{2\omega\kappa_l X_3} + f_{i3}e^{\omega(\kappa_l+\kappa_s)X_3}\}, \text{ where} \\
\kappa_s = \sqrt{\frac{1}{V_0^2} - \frac{1}{V_S^2}}; \kappa_l = \sqrt{\frac{1}{V_0^2} - \frac{1}{V_L^2}}; K_2 = \frac{2\kappa_l\kappa_s}{1/V_0^2 + \kappa_s^2}; K_4 = \frac{2}{1 + V_0^2\kappa_s^2}; \\
f_{11} = f_{21} = -0.5f_{31} = 0.5f_{51} = (\kappa_s/V_0)^2;\ f_{41} = 1/V_0^4 + \kappa_s^4; \\
f_{12} = (\kappa_l K_2/V_0)^2;\ f_{13} = -2\kappa_s\kappa_l K_2/V_0^2;\ f_{22} = K_4^2 f_{21};\ f_{23} = -2K_4 f_{21}; \\
f_{32} = \kappa_l K_2 K_4 f_{31}/\kappa_s;\ f_{33} = -[K_4 + \kappa_l K_2/\kappa_w]f_{31};\ f_{42} = K_2^2/V_0^4 + (\kappa_s\kappa_l K_4)^2; \\
f_{43} = -2[K_2/V_0^4 + \kappa_s^3 k_l K_4];\ f_{52} = \kappa_1 K_2 K_4 f_{51}/\kappa_s;\ f_{53} = -[\kappa_l K_4/\kappa_s + K_2]f_{51}
\end{gathered} \tag{8.7}$$

$$
\begin{aligned}
\alpha_1^{||} &= \frac{1}{3\lambda+2\mu}\left(\lambda+2l-\frac{\lambda(2\lambda+6\mu+4m)}{2\mu}\right),\\
\alpha_2^{||} &= \frac{1}{3\lambda+2\mu}\left(\lambda+2l+\frac{(\lambda+\mu)(2\lambda+6\mu+4m)}{\mu}\right),\\
\alpha_3^{||} &= \frac{1}{3\lambda+2\mu}\left(\lambda+2l+\frac{\lambda(\lambda+2m-n)}{2\mu}\right),\\
\alpha_4^{||} &= \frac{1}{3\lambda+2\mu}\left(3\lambda+2\mu+m-\frac{\lambda(2\mu-n/2)}{2\mu}\right),\\
\alpha_5^{||} &= \frac{1}{3\lambda+2\mu}\left(\lambda+\mu+m-\frac{\lambda(\mu-n/2)}{2\mu}\right);\\
\alpha_1^{\perp} &= \alpha_2^{\perp} = \alpha_1^{||},\\
\alpha_3^{\perp} &= \frac{1}{3\lambda+2\mu}\left(\lambda+2l-\frac{(\lambda+\mu)(\lambda+2m-n)}{\mu}\right),\\
\alpha_4^{\perp} &= \alpha_5^{\perp} = \frac{1}{3\lambda+2\mu}\left(m-\lambda-\frac{(\lambda+\mu)n}{2\mu}\right)
\end{aligned}
\tag{8.8}
$$

8.4 Polarization restrictions for nonlinear bulk wave interactions

In work [Kor98] Korneev considered the interaction of bulk waves in a fixed volume, substituting the displacement field of two incident waves in form

$$u_0 = u_0^{(1)} + u_0^{(2)} = A_0\cos(\omega_1 t - k_1 r) + B_0\cos(\omega_2 t + k_2 r) \tag{8.9}$$

into Equation (2.30). Part of Equation (2.31), describing the interaction of elastic waves, can be written in form:

$$
\begin{aligned}
&p(r,t) = I^{+}\sin[(\omega_1+\omega_2)t-(k_1+k_2)r] + I^{-}\sin[(\omega_1-\omega_2)t-(k_1-k_2)r],\ \text{where}\\
&I^{\pm} = -\frac{1}{2}\Big\{(\mu+n/4)[(A_0B_0)(k_2k_2)k_1 \pm (A_0B_0)(k_1k_1)k_2 + (B_0k_1)(k_2k_2)A_0\\
&\quad\pm (A_0k_2)(k_1k_1)B_0 + 2(A_0k_2)(k_1k_2)B_0 \pm 2(B_0k_1)(k_1k_2)A_0]\\
&\quad+(\lambda+\mu+m-n/4)[(A_0B_0)(k_1k_2)k_2 \pm (A_0B_0)(k_1k_2)k_1 + (B_0k_2)(k_1k_2)A_0 \pm (A_0k_1)(k_1k_2)B_0]\\
&\quad+(m-n/4)[(A_0k_2)(B_0k_2)k_1 \pm (A_0k_1)(B_0k_1)k_2 + (A_0k_2)(B_0k_1)k_2 \pm (A_0k_2)(B_0k_1)k_1]\\
&\quad+(2l-m+n/2)[(A_0k_1)(B_0k_2)k_2 \pm (A_0k_1)(B_0k_2)k_1]\\
&\quad+(\lambda+m-n/4)[(A_0k_1)(k_2k_2)B_0 \pm (B_0k_2)(k_1k_1)A_0]\Big\}
\end{aligned}
\tag{8.10}
$$

Here the expressions (x,y) denote scalar products. If resonant conditions (2.41) are fulfilled, the solution for the scattered second wave in the far-field could be evaluated with the

First wave	Scattering sign	Second wave		Scattered wave
P	±	P	→	P
P	-	P	→	SV
P	±	SV	→	P
P	-	SV	→	SV
SV	+	SV	→	P
SH	+	SH	→	P
P	-	SH	→	SH

Table 8.1: Allowed cases of bulk wave interaction [Kor98].

following integral:

$$\begin{aligned} \boldsymbol{u}_l(\boldsymbol{r},t) = &\frac{(\boldsymbol{I}^+\hat{\boldsymbol{r}})\hat{\boldsymbol{r}}}{4\pi V_P^2\rho r}\int_V \sin\left[\left(\frac{\omega_1+\omega_2}{V_P}\hat{\boldsymbol{r}}-\boldsymbol{k}_1-\boldsymbol{k}_2\right)\cdot\boldsymbol{r}'-(\omega_1+\omega_2)\left(\frac{r}{V_P}-t\right)\right]dV+\\ &\frac{(\boldsymbol{I}^-\hat{\boldsymbol{r}})\hat{\boldsymbol{r}}}{4\pi V_P^2\rho r}\int_V \sin\left[\left(\frac{\omega_1-\omega_2}{V_P}\hat{\boldsymbol{r}}-\boldsymbol{k}_1+\boldsymbol{k}_2\right)\cdot\boldsymbol{r}'-(\omega_1-\omega_2)\left(\frac{r}{V_P}-t\right)\right]dV+\\ &\frac{\boldsymbol{I}^+-(\boldsymbol{I}^+\hat{\boldsymbol{r}})\hat{\boldsymbol{r}}}{4\pi V_S^2\rho r}\int_V \sin\left[\left(\frac{\omega_1+\omega_2}{V_S}\hat{\boldsymbol{r}}-\boldsymbol{k}_1-\boldsymbol{k}_2\right)\cdot\boldsymbol{r}'-(\omega_1+\omega_2)\left(\frac{r}{V_S}-t\right)\right]dV+\\ &\frac{\boldsymbol{I}^--(\boldsymbol{I}^-\hat{\boldsymbol{r}})\hat{\boldsymbol{r}}}{4\pi V_S^2\rho r}\int_V \sin\left[\left(\frac{\omega_1-\omega_2}{V_S}\hat{\boldsymbol{r}}-\boldsymbol{k}_1+\boldsymbol{k}_2\right)\cdot\boldsymbol{r}'-(\omega_1-\omega_2)\left(\frac{r}{V_S}-t\right)\right]dV, \end{aligned} \tag{8.11}$$

where $\boldsymbol{r} = r\hat{\boldsymbol{r}}$, $|\hat{\boldsymbol{r}}| = 1$ is the radius-vector from the center point of interaction region to observation point; and $\boldsymbol{r}'$ is the radius-vector inside the integration (interaction) volume V. From (8.11) follow, that the amplitudes of the scattered waves are proportional to their projections in the direction, defined by polarization of the wave (parallel to $\hat{\boldsymbol{r}}$ for P-waves and perpendicular for S-waves).

This fact imposes an additional *polarization restriction*: scattering amplitude could be zero, even if conditions (2.41) are satisfied. Allowed interactions for bulk waves, according to Korneev, are shown at Table (8.1).

8.5 Ordinary least squares fit

OLS is an optimal solution for the classical linear optimization problem [Gol91]: find the unknown coefficient(s) β for the best linear approximation having the series of observations of independent variable(s) x, dependent variable y in presence of unknown random noise ε:

$$y_i = \beta x_i + \varepsilon_i, i = 1, ..., n. \tag{8.12}$$

According to the Gauss-Markov theorem, the following solution has the lowest sampling variance (or the smallest error) in class of linear unbiased estimators for one- and multidimensional regression problems:

$$\beta_{OLS} = (X^T X)^{-1} X^T Y, \tag{8.13}$$

where T stands for transpose.

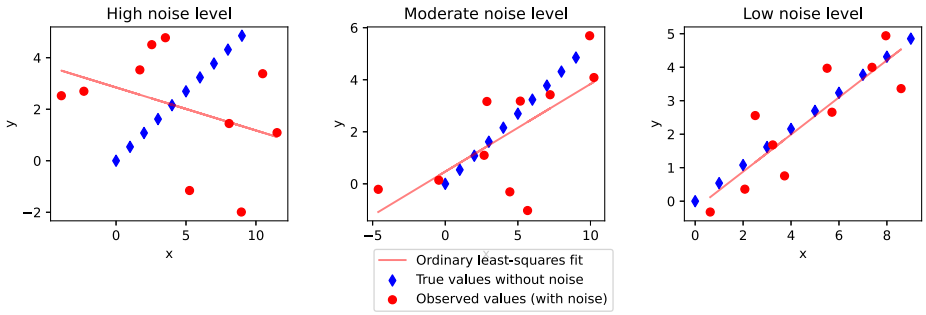


Figure 8.1: Ordinary least squares fit.

Examples of OLS fit for generic data are given in Figure 8.1.

8.6 Supplementary graphics of perturbation model simulation results

Solution of Equation (2.42) is presented in the Figure 8.2.

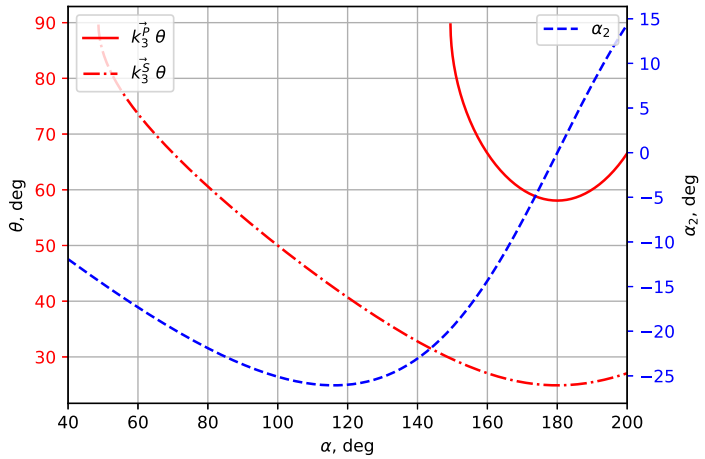


Figure 8.2: Dependence of angle θ on the angle between sources α for the scattered P-wave (solid line) and S-wave (dash-dotted line). Angle definitions are given in Figure 2.5.

Detailed results of efficiency calculations with perturbation model for nearly grazing incident angle are given here. This material presents detailed results of the calculations described in Section 2.7. Angles α and α_2 are shown at horizontal axes, while the vertical axis indicates the scattering efficiency. Color bars refer to the frequency ratio of the two input waves. Six wave-scattering modes are presented. As discussed above, any fixed couple of parameters from the list (f_1/f_2, α, α_2, θ) determines the others and the relative interaction efficiency. A numerical comparison is given in Table 4.3.

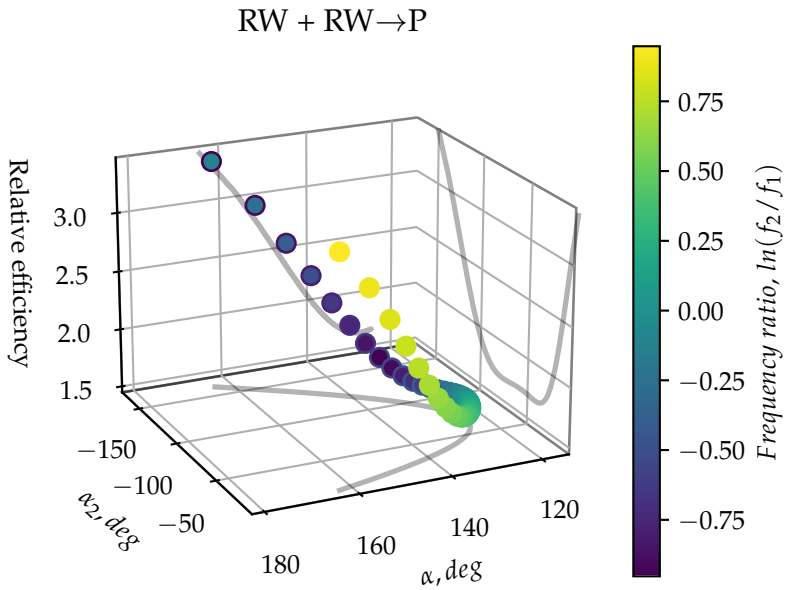


Figure 8.3: RW+RW→ P, efficiency of the pressure wave generation by two Rayleigh waves, propagating at angles α_1 and α_2, with a frequency ratio f_2/f_1

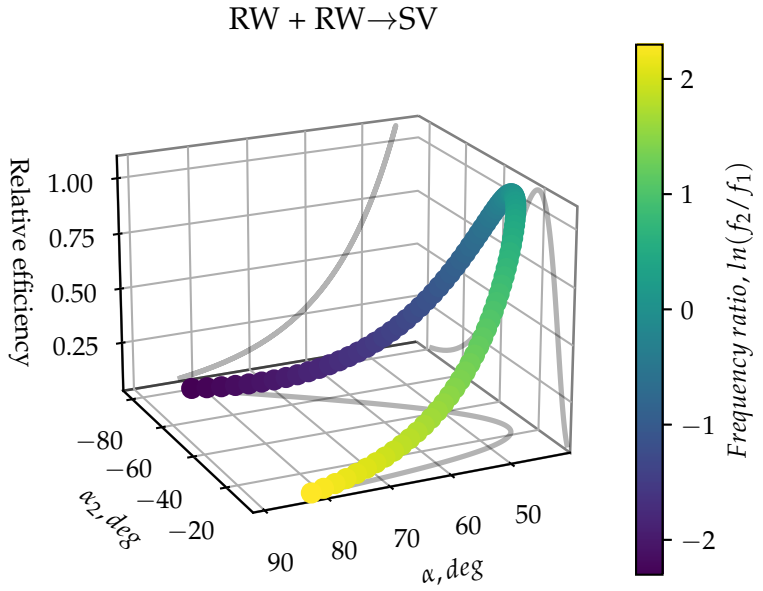


Figure 8.4: RW+RW→ SV, efficiency of the shear wave generation by two Rayleigh waves, propagating at angles α_1 and α_2, with a frequency ratio f_2/f_1

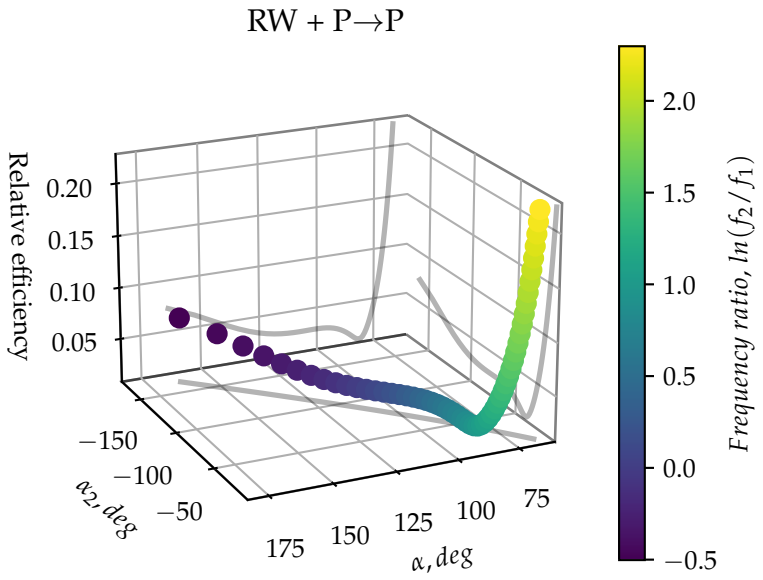


Figure 8.5: RW+P→ P, efficiency of the pressure wave generation by Rayleigh wave and pressure wave, propagating at angles α_1 and α_2, with a frequency ratio f_2/f_1

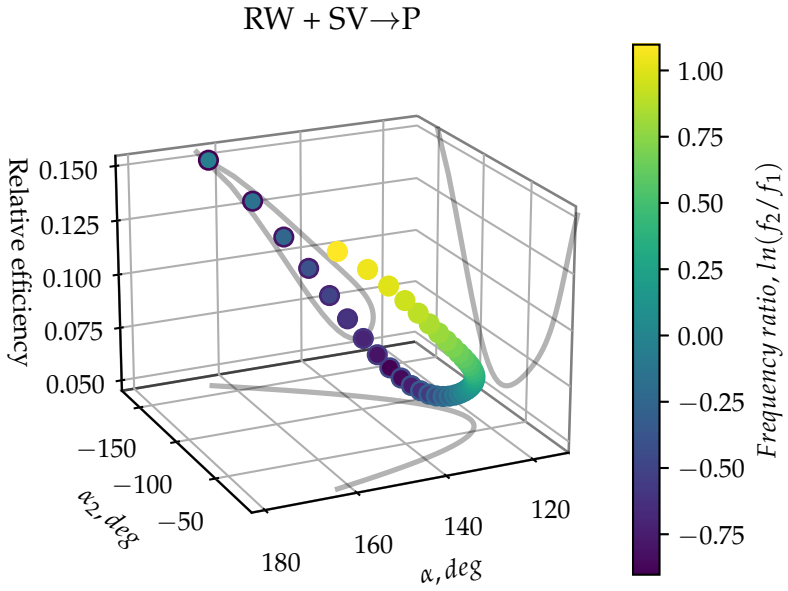


Figure 8.6: RW+SV→ P, efficiency of the pressure wave generation by Rayleigh wave and shear wave, propagating at angles α_1 and α_2, with a frequency ratio f_2/f_1

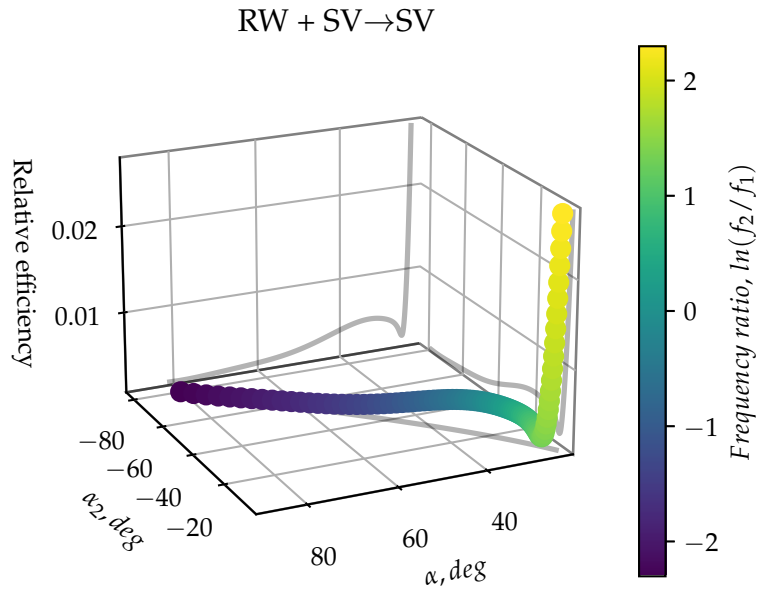


Figure 8.7: RW+SV→ SV, efficiency of the shear wave generation by Rayleigh wave and shear wave, propagating at angles α_1 and α_2, with a frequency ratio f_2/f_1

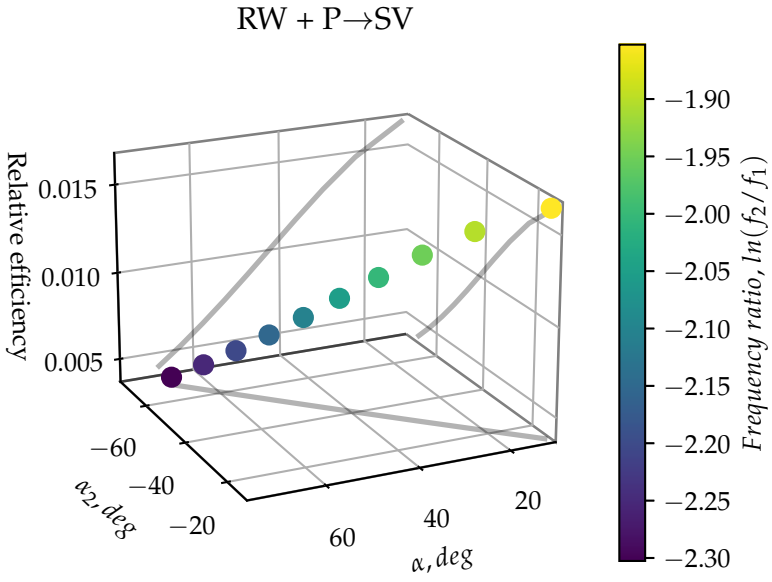


Figure 8.8: RW+P→ SV, efficiency of the shear wave generation by Rayleigh wave and pressure wave, propagating at angles α_1 and α_2, with a frequency ratio f_2/f_1

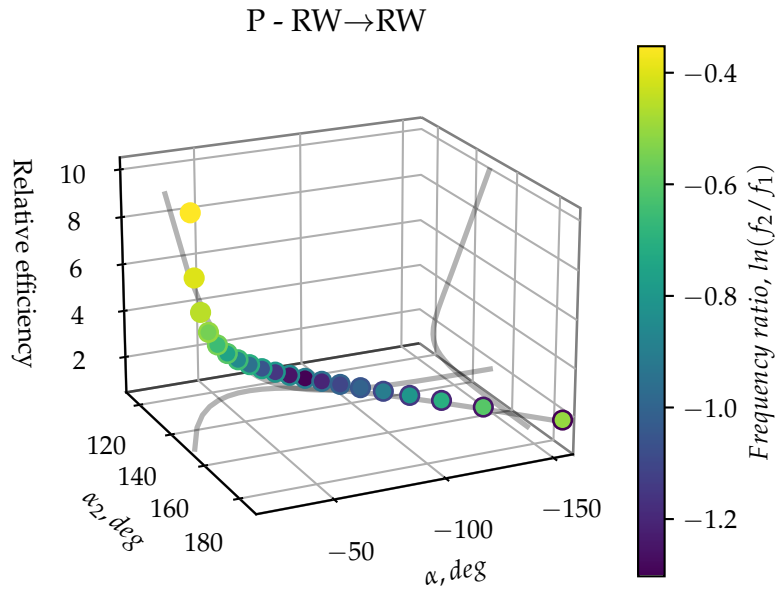


Figure 8.9: P-RW→ RW, efficiency of the Rayleigh wave generation by pressure wave and Rayleigh wave, propagating at angles α_1 and α_2, with a frequency ratio f_2/f_1

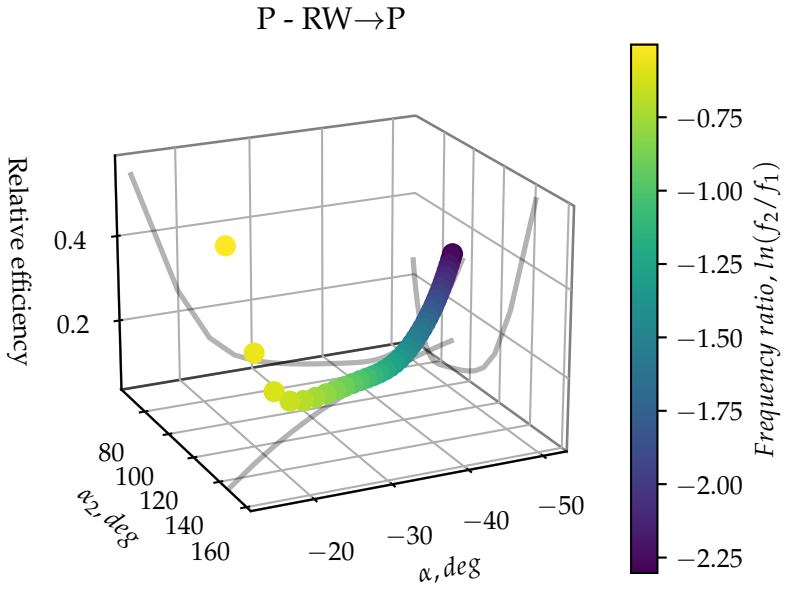


Figure 8.10: P-RW→ P, efficiency of the pressure wave generation by pressure wave and Rayleigh wave, propagating at angles α_1 and α_2, with a frequency ratio f_2/f_1

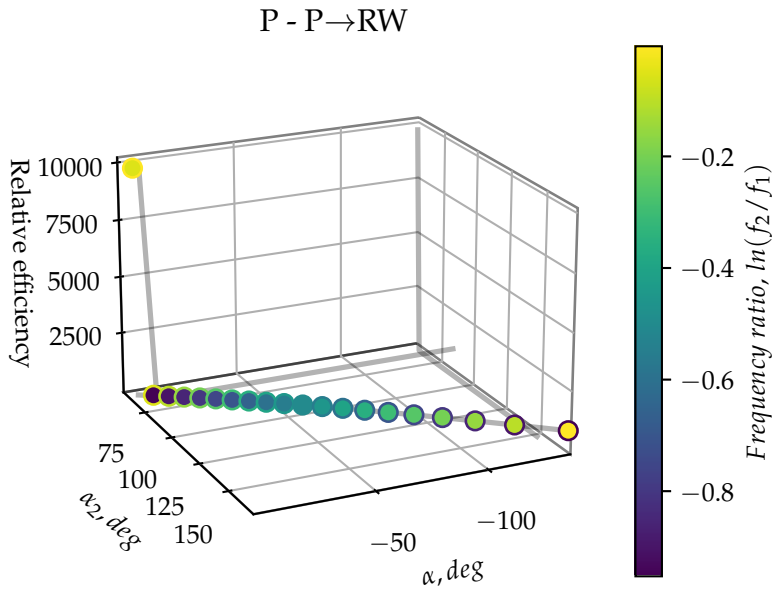


Figure 8.11: P-P→ RW, efficiency of the Rayleigh wave generation by two pressure waves, propagating at angles α_1 and α_2, with a frequency ratio f_2/f_1

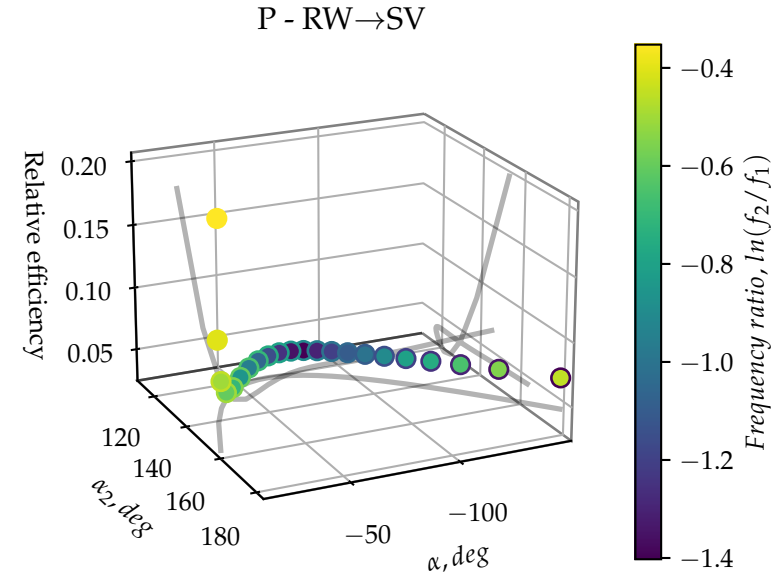


Figure 8.12: P-RW→ SV, efficiency of the shear wave generation by pressure wave and Rayleigh wave, propagating at angles α_1 and α_2, with a frequency ratio f_2/f_1

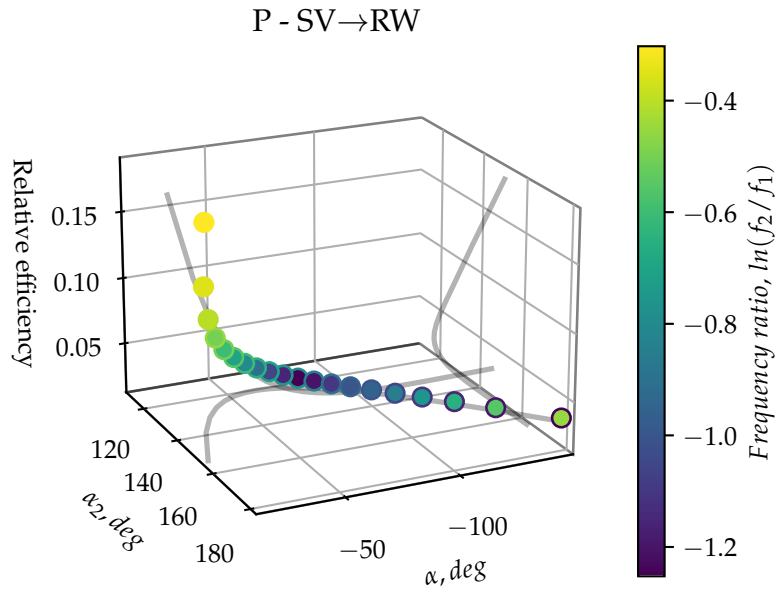


Figure 8.13: P-SV→ RW, efficiency of the Rayleigh wave generation by pressure wave and shear wave, propagating at angles α_1 and α_2, with a frequency ratio f_2/f_1

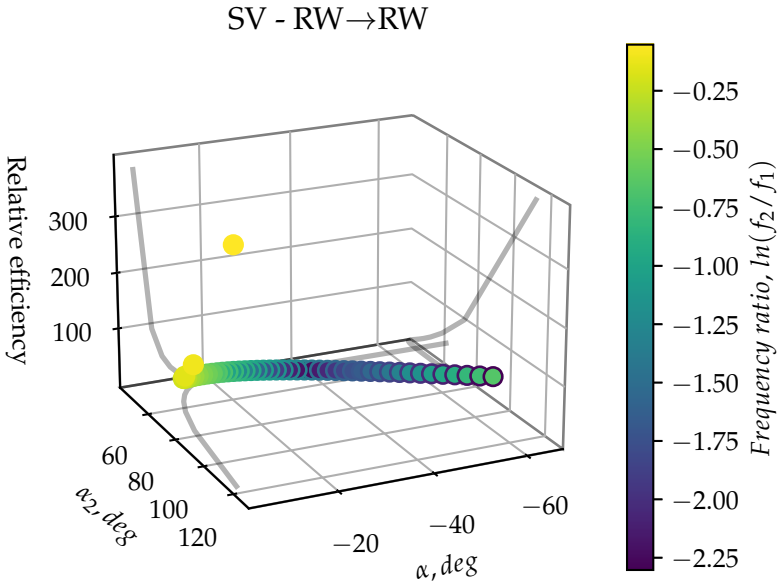


Figure 8.14: SV-RW→ RW, efficiency of the Rayleigh wave generation by shear wave and Rayleigh wave, propagating at angles α_1 and α_2, with a frequency ratio f_2/f_1

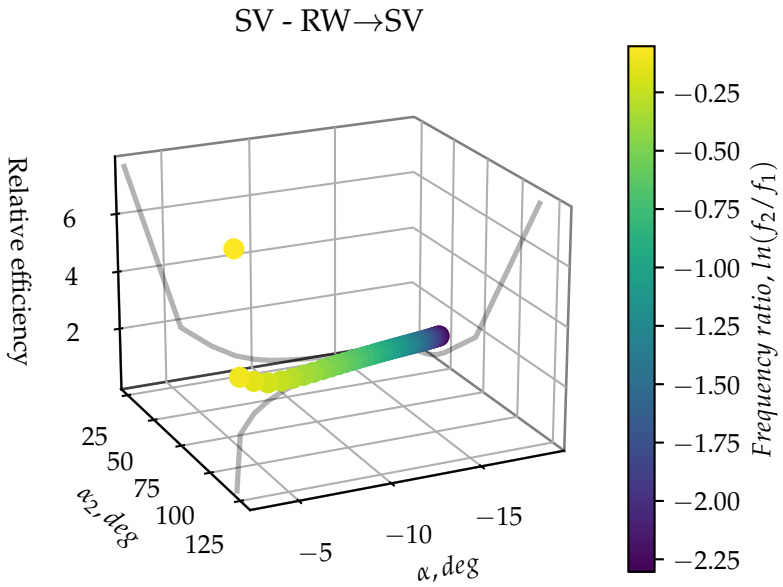


Figure 8.15: SV-RW→ SV, efficiency of the shear wave generation by shear wave and Rayleigh wave, propagating at angles α_1 and α_2, with a frequency ratio f_2/f_1

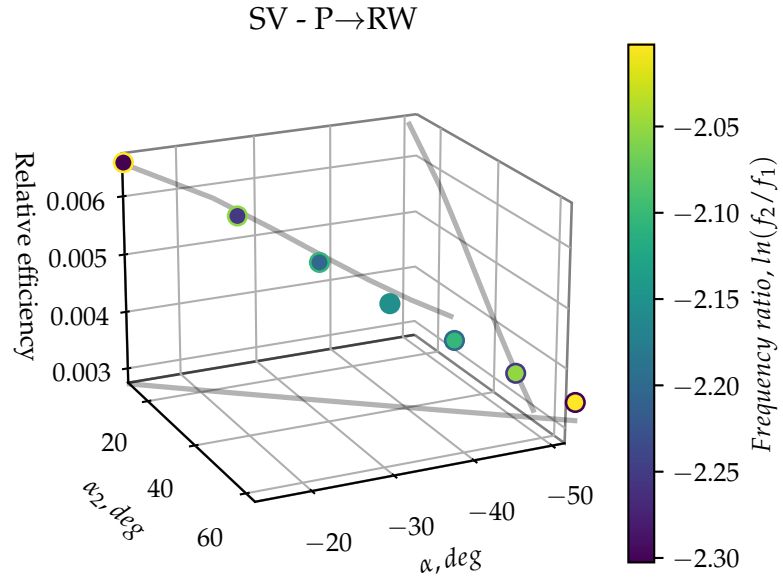


Figure 8.16: SV-P→ RW, efficiency of the Rayleigh wave generation by shear wave and pressure wave, propagating at angles α_1 and α_2, with a frequency ratio f_2/f_1

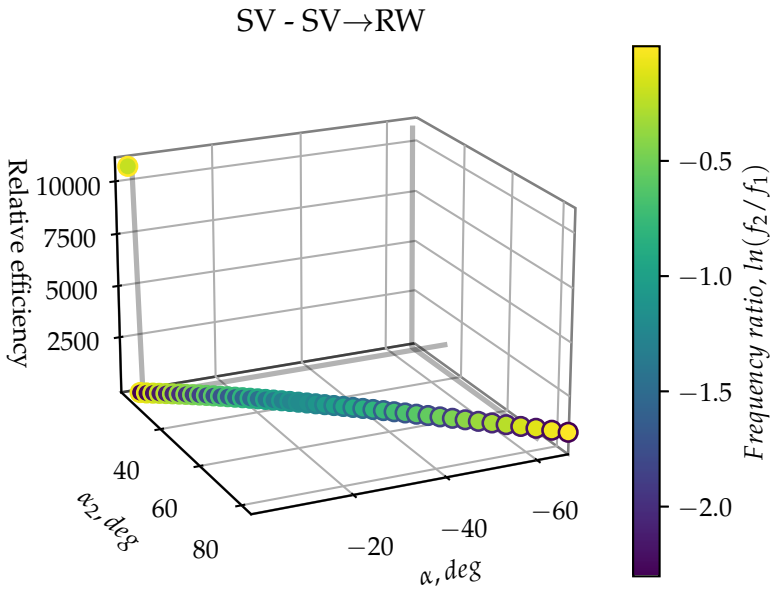


Figure 8.17: SV-SV→ RW, efficiency of the Rayleigh wave generation by two shear waves, propagating at angles α_1 and α_2, with a frequency ratio f_2/f_1

List of publications

Reviewed journal papers:

- Sergey Gartsev, Bernd Köhler. *Direct measurements of Rayleigh wave acoustoelastic constants for shot-peened superalloys* (NDT & E International, Volume 113, July 2020)
- Sergey Gartsev, Peng Zuo, Marek Rjelka, Andreas Mayer, Bernd Köhler. *Nonlinear interaction of Rayleigh waves in isotropic materials: numerical and experimental investigation* (Ultrasonics, Volume 122, May 2022)

Conference papers (presenting author):

- *Nonlinear elastic behavior of aero-engine materials for microstructure and stress state characterization*, 12th ECNDT (2018, Göteborg)
- *Determination of the nonlinear elastic constants in a surface treated layer for aero-engine disk residual stress measurement*, NDT in Aerospace, (2018, Dresden)
- *Possible Application Of Rayleigh Wave Scattering For The Surface-Treated Structural Elements Characterization*, 9th EASN (2019, Athens)
- *On use of directly measured RW AECs for the residual stress evaluation*, NDT in Aerospace, (2020, virtual)
- *Application of Multidimensional FFT for the Extraction of Wave Vectors and Computer-Aided Visualization of LDV Measurements*, IEEE IUS (2021, virtual)

Acknowledgements



Светлой памяти моего отца,
Николая Александровича Гарцева,
и моего учителя,
Петра Георгиевича Карклэ

First I want to thank my mom for her endless patience and everyday wisdom.

Secondly, I would like to send my regards to the science town of Zhukovskiy, school number 10, the faculty of DAFE MIPT and my former colleagues from TsAGI for their trust, expertise, openness, high standards of conduct and enthusiasm. You ignited my curiosity once and I still can't stop. Particular respect to the DAFE MIPT football team aka "football elite".

Thirdly, salute to all the organizers and participants of the NDTonAIR project - Stefano, Marco, Christ, Gui, Bernd, Silvio, Sevilia, Tommaso, Bengisu, Hamed, Yongtak, Quiji and all the others for the excellent organization and friendly atmosphere.

Without the professionalism and support of Fraunhofer IKTS team - Bernd, Henning, Marek, Martin, Zsolt, Matthias, Frank, Susanne, Christoph and Gosia - this work would certainly not been possible.

The kindness, patience, endurance and politeness of Prof. Mayer, who stoically withstood all my pathetic attempts to touch the world of theoretical physics, deserves a special tribute. Andreas, thank you once again.

Especial thanks to Peng, whose precious free time I have stolen for the opportunity to compare my results with the high-fidelity FEM.

Last but not least, I want to thank the people who were there for me and gave me reasons to smile even on the cloudiest of days: Simon, Jendrik, Wieland, Emre, Ignacio, Chiara, Adenisa, Nikolai, Nail, Sanya, Ivan, Sergei, Anya, Misha, Yulia, Sasha, Ruslan, Roma, Kirill and #carvingebat'team. Special thanks for not throwing heavy objects after my degraded jokes.

no to war

This work focuses on the evaluation of the acoustoelastic constants (AEC) using Rayleigh waves (RW). These constants represent the state of the microstructure of the material on macroscopic level and are therefore very sensitive to changes in microstructure. They are used as input parameters to determine the residual stress level with acoustoelastic measurements.

The comparison of different measurement strategies and the investigation of the possibility to create an in-situ method to measure the AEC near the surface using the nonlinear interaction of two Rayleigh waves are the main contributions of this work. Nonlinear interactions between elastic waves are considered as a prospective mean for in-situ determination of local near-surface nonlinear elastic parameters. The permissible interactions between bulk and surface waves were investigated using an analytical model and then compared with experimental results and available FEM simulations.

ISBN 978-3-8396-1881-3

Fraunhofer VERLAG